SIMULATION TOOLS FOR OPTICAL RESIST MODELS STORM

by

Ebo Harry Croffie

Memorandum No. UCB/ERL M01/29

9 August 2001

SIMULATION TOOLS FOR OPTICAL RESIST MODELS STORM

by

Ebo Harry Croffie

Abstract

Simulation Tools for Optical Resist Models (STORM)

by

Ebo Harry Croffie

Doctor of Philosophy in Applied Science and Technology

University of California at Berkeley

Professor Andrew R. Neureuther, Chair

STORM is a collection of software tools that provide a general numerical frame-work for tackling nonlinear model-equations encountered in photoresist process modeling. Post exposure bake models based on a moving-boundary acid transport concept that incorporates transient free-volume generation and densification are used as test vehicles for the simulation tools. The numerical tools are also used to demonstrate a moving-boundary silylation simulator which includes polymer relaxation, reaction-dependent silylating agent diffusivity, and stress-dependent retardation of the reaction rate.

Three key elements of the numerical algorithms include: (1) A second order implicit time discretization algorithm with variable timestep control for stability and accuracy requirements. This algorithm known as BDF2 is well suited for highly nonlinear partial differential equations; (2) An improved space discretization finite element algorithm which uses method of partial variable substitution to reduce the number of system

1

variables; (3) Miller's Krylov Subspace Iteration Convergence Accelerator which is used to speed up convergence of the Newton iterations. The Krylov accelerator achieves simulation runs of less that 5 minutes using realistic resist parameters. The same simulation can take more than a day when the Krylov accelerator is not used.

A novel free-volume PEB model is presented. The development of this model was driven by challenge to explain new experimental data from collaborators at the University of Texas at Austin. The model is able to link the relief image formation to the mechanical and chemical properties of the resist polymer and is capable of simulating the resist shrinkage upon baking.

The two dimensional silylation simulator is the first of its kind to include stress effects. Silylation simulation results illustrate the interplay of the various physical parameters in determining final silylation depth and sidewall angle as a function of exposure and silylation conditions and the film's material properties.

Principal examples in 193nm resist modeling and characterization and especially the ability to study influence of chemical structure and properties of photoacid generators on lithographic performance of 193nm resist is presented. The simulator is used to quantify acid generation efficiency, reaction efficiency and diffusion properties of the PAGs, and their effects on resist performance.

Dedication to the angels in my life...

*...To the loving memory of my mother, **Agnes Ama Adu-Gyamfi**. Your sons could not have pulled through without your protection. May we continue to flourish in your perfect peace...*

*...To the loving memory of my grandmother, **Stella Nyann**. The architect of my life. The life you believed worth building is empty without you. Your hard work and sacrifices were not in vain. Rest now...*

*...To my wife, **Abigail Adwoa Asantewaa Croffie**. A Love Supreme. Odo bi ye wu...*

Acknowledgments

I would like to thank my advisor, Professor Andrew R. Neureuther for his guidance and support. I have greatly benefited from his wisdom. His natural ability to motivate students and his fairness in dealing with students are quiet extraordinary. I would also like to thank Professor William Oldham for serving on my qualification examination and dissertation review committee. My thanks also goes to Professor Sanjay Govindjee for helping me to tie the loose ends on finite element algorithm implementation, as well as for fruitful discussions on advanced numerical methods for stiff equations. I would also like to thank him for serving on my qualification examination committee and dissertation review committee. Thanks to Professor Kieth Miller for helping me with the BDF2 and Krylov subspace numerical algorithms implementation and for serving on my qualification examination committee. My thanks also go to Professor Grant Willson at the University of Texas, Austin for his many help on resist chemistry.

I would also like to thank my colleagues and friends, Mr. Shafiul Litu, Mr. Ibna Faruque, Mr. Lei Yuan, Mr. Mosong Cheng, Mr. Yashesh Shroff, Mr. Kostas Adam, Dr. Tom Pistor, Dr. Marco Zuniga, Dr. Fang Piao, Dr. Zulu Xaba, Professor Luke Lee and Professor Elinor Velasquez for their friendship and support.

Thanks to my family members in the U.S., Ghana and Europe for all their love, encouragements and support. A special thanks to the Reed family in California for their love and care.

Hi Mom...

1 Introduction

Optical lithography has been a key enabling technology for the miniaturization of semiconductor devices. This has been made possible by the use of shorter wavelengths of light to pattern submicron features. At each move towards a shorter wavelength, new resist materials are developed. Furthermore, there is a renewed interest in surface imaged resist processes such as top surface imaging (TSI) and bilayer resists (BLR), since these offer viable extensions of optical lithography tools for future generations of integrated circuits (ICs).

During the optical lithography step in IC manufacturing, a mask pattern comprised of dark and clear areas is transferred to the photoresist on the wafer surface through the use of imaging optics. Resist chemistry as well as underlying film types will affect the final resist profile on the wafer. Because of the complexities associated with such a system, modeling has been used extensively to investigate the effects of different operating parameters.

Modeling and simulation is also useful for understanding factors responsible for various issues associated with the implementation of advanced lithography processes and emerging technologies. Semiconductor process simulators including COMPOSITE[1],

SAMPLE[2], DEPICT[3], PROLITH[4], SOLID[5] and SUPREM[6] have become important tools in process development and optimization. Given the reduction in cost of computation and increase in cost of experimentation trend, process simulators will continue to provide a cost effective means of understanding physical aspects of processing steps to allow for process optimization.

Accurate and scalable physical models and efficient numerical algorithms are essential in developing simulators for these advanced resist processes. Scalable models are models which provide accurate prediction of processes occurring in physical dimensions (size and shape) different from those used to characterize the models[7]. Developing a scalable model begins with experimental investigations of the physical mechanisms and important variables in the process to establish a basic model. The model verification step requires systematic experimental data that can be readily quantified. Thus, careful parametric studies must then be carried out to provide quantitative parameters for the range of operating conditions of interest.

The most difficult aspect of modeling advanced resist processes such as chemically amplified resists (CARs) post exposure bake (PEB) and TSI resist silylation is emulating the reaction state dependent transport. The difficulty arises primarily out of the nonlinearity associated with the behavior of diffusion species with reacted material state. Exponential diffusion models emulate the state dependent diffusion and offer more accurate predictions of PEB effects in CARs and profile shapes in silylated resist. These model-equations result in a system of nonlinear partial differential equations (PDEs) describing the time rate of change of reacting and diffusion species. Verifying such models is often

2

difficult, as analytical solutions to many of them are generally not available. Numerical simulations are often needed to solve the model-equations so that the models can be tested against experimental observations. Unfortunately, the nonlinear PDEs degrade the performance of numerical methods when no acceleration schemes are employed. The long simulation times required to solve these equations using conventional methods makes the process simulator unattractive. A rigorous and flexible numerical framework for simulating complex resist model-equations is needed for reliable prediction of resist profiles. This work presents simulation tools that provides such a framework. The program is called STORM, which stands for Simulation Tools for Optical Resist Models.

Several numerical tools have been included in STORM to provide a general numerical framework for tackling complex model-equations encountered in optical lithography process modeling. STORM utilizes the finite element method to emulate the polymer deformation. It employs efficient numerical algorithms based on the second order backward difference formula (BDF2) and Krylov subspace Newton convergence acceleration methods to facilitate rapid simulation of nonlinear diffusion model-equations. A greater than order of magnitude decrease in simulation time is achieved with the Krylov subspace accelerator. Monte Carlo methods for simulating oxygen reactive ion etching for surface imaged resist processes are also employed in STORM.

Post exposure bake (silylation) involves changing topographies due to polymer shrinkage (swelling). It also exhibits moving interfaces due to reaction state dependent transport. The most difficult aspect of modeling CARs and top surface imaging resist silylation is emulating the reaction-state dependent transport. The difficulty arises primarily

out of the nonlinearity associated with the behavior of diffusion with reacted material state. Exponential diffusion models emulates the state-dependent diffusion and offer more accurate predictions of PEB effects in CARs and profile shapes in silylated resist. These model-equations result in a system of nonlinear partial differential equations (PDEs).

The resulting nonlinear PDEs degrade the performance of classical numerical methods such as the finite difference method. The need for rigorous numerical techniques to facilitate rapid simulation of the more accurate nonlinear diffusion model-equations has been the motivation for this work.

The thesis starts with a motivation for the work leading to this dissertation followed by post exposure bake models and their simplifications. It then presents a description of TSI modeling and numerical algorithms and ends with applications of the modeling methodology to 193nm chemically amplified resist materials.

This dissertation is a result of several collaboration works. The initial project leading to the work in this dissertation was the development of a silylation simulator (co-developed with Marco Zuniga) based on moving boundary concepts. This made possible the study of effects of stress on reaction and diffusion mechanisms to understand lithography issues such as process trends on feature types and sizes. The advent of transparent materials at 193nm lithography directed this dissertation work to accommodate development of efficient mechanistic based chemically amplified resist simulators to address 193nm resist issues such as acid diffusion and line-end shortening.

Collaboration work with Lei Yuan on algorithm improvements of the finite element method (FEM) implementation and Mosong Cheng on optimization algorithms for simu-

4

lator calibrations has greatly improved the efficiency of STORM. Lei Yuan worked on the concept, coding and testing of the improved FEM algorithm. Mosong Cheng also provided simulation results of his modified finite difference method (FDM) for comparison with STORM simulation. The concept, coding and testing of the FDM are all to his credit.

A collaborative work between University of California at Berkeley TCAD Group and University of Texas at Austin Resist Synthesis Group on modeling chemically amplified resist led to the development of the free volume enhanced acid transport PEB model.

193nm resist material modeling work was done in collaboration with Frank Houlihan, Om Nalamasu, Pat Watson and Ray Cirelli of Bell Laboratories, and Allen Gabor and Ognian Dimov of Arch Chemicals.

A general overview of advanced resist processes in optical lithography, followed by the evolution of CAR models is presented in Chapter 2. This chapter also presents free volume enhanced acid transport models and describes approximate analytical models for rapid evaluation of PEB effects in CARs. Chapter 3 presents a general purpose polymer silylation model and the O_2 RIE dry development model for TSI process simulation. The numerical discretization algorithms implemented in STORM are described in Chapter 4, along with numerical example of the PEB model discretization, algorithm performance and simulation results. Chapter 5 presents experimental methodology for extracting data that can be readily quantified for simulator calibrations and show application results to 193nm chemically amplified resists, with emphasis on photoacid generator performance modeling to aid in resist material developments. Results on line end shortening and process

windows evaluations will also be discussed before concluding this dissertation in

Chapter 6.

2 Evolution of Chemically Amplified Resist Models

2.1. Introduction

In this chapter, the works of many authors on chemically amplified resist modeling are described. The chapter starts with an overview of the chemically amplified resist imaging process. It then gives a historical account of the modeling work and concludes with a unified model based on free volume enhanced acid transport concept. It demonstrates that many models can be deduced from this general model under simplifying assumptions.

2.2. Resist imaging overview

During the optical lithography process in integrated circuit fabrication, a device structure is patterned by imaging a mask onto a radiation sensitive material (photoresist) overcoating different thin film materials on the wafer. These photoresist films capture the pattern delineated through initial exposure to radiation and allow subsequent pattern transfer to the underlying layers[9]. The radiation source, imaging optics, mask type, and resist performance determine the minimum feature size that can be reproduced by the lithography process. Higher resolution in the exposure tool has been achieved by decreasing the exposure wavelength into the deep-ultraviolet (DUV) region (248nm and 193nm)[8]. To achieve high sensitivity and throughput, the resist systems best suited for DUV lithography are the chemically amplified resists (CARs). This class of resists enhances the dose

response of an exposed resist by undergoing chemical changes that alter the dissolution properties of the resist upon post exposure bake (PEB) process.

Positive tone CARs are composed of three essential components: a base resin, a dissolution inhibitor and a photoacid generator (PAG). Exposing the resist to DUV light generates acid from the PAG. During a subsequent post exposure bake (PEB), the photogenerated acid catalyzes a thermally induced reaction that cleaves the dissolution inhibitor groups (protecting groups), rendering the reacted (deprotected) region soluble in aqueous developer. Meanwhile, the acid diffuses from a high dose region to a low dose region washing out standing waves and causing the reacted region to be larger than the initially exposed region. In addition, most CARs exhibit volume shrinkage after the PEB step due to desorption of volatile group by-products that are created during the bake[12]. The resist pattern after development serves as a mask through which series of etching, doping and deposition steps result in the desired device functions[10][9]. Figure 2-1 shows the DUV lithography process for positive photoresist. In this figure, the effect of the polymer volume shrinkage is illustrated.
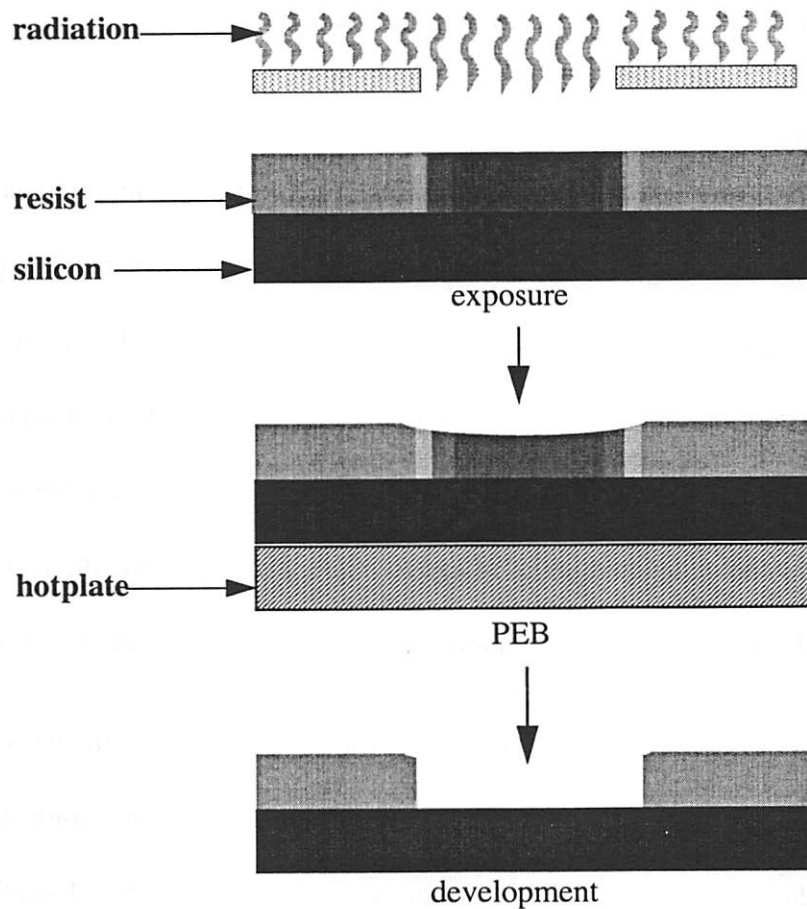
Figure 2-1. Positive tone chemically amplified resist process.

The CAR process described above can be divided into three subprocesses, namely, the exposure, the latent image formation during PEB, and the relief image formation process during wet development. Significant contributions have been made to the studying of the different subprocesses to aid in modeling and understanding the process. Formulating the appropriate model-equations to describe the process and developing the right simulation tools is just as important as the ability to perform experiments to quantify and calibrate

the model-equations for a given resist system. The remainder of this chapter presents an evolution of models and model quantification methodology.

2.3. Exposure Model

Dill and co-workers published their pioneering work in lithography simulation in a series of ground breaking papers[13][14][15]. Their approach in modeling lithography consists of two main components: simulation of the exposure tool and simulation of the resist. In order to simulate the exposure tool, the aerial image distribution obtained from the imaging optics is calculated. Following the calculation of the exposure tool, resist simulation converts the calculated aerial image to a latent image inside the resist. Post exposure bake (PEB) and dissolution simulation converts the latent image to a relief image.

Dill *et al.* proposed an exposure model for diazo-type resist in terms of the illumination intensity and photoactive compound (PAC) concentration within the resist. The model gives the intensity of the PAC concentration M as a function of depth in the resist film. The absorption coefficient is described as

Equation 2-1. $$\alpha = AM(z, t) + B$$

where M is the normalized local concentration of PAC. The destruction of the photoactive compound is described by

Equation 2-2. $$\frac{\partial}{\partial t}M(z, t) = -I(z, t)CM(z, t)$$

where I is the illumination intensity described by

Equation 2-3. $$\frac{\partial}{\partial z}I(z, t) = -\alpha I(z, t)$$

The *A, B, C* parameters are resist dependent and are known as the Dill parameters. *C* is the reaction rate constant for PAC conversion.

The exposure of standard positive tone resists has typically been quantified by monitoring the resist transmission as a function of exposure dose and then fitting Dill's *ABC* parameters to the results. Traditionally, the Dill model is adapted to the acid generation reaction for CARs by defining *M* as the normalized photoacid generator (PAG) concentration and 1-*M* as the normalized acid concentration. In this case, *C* is assumed to be the acid generation rate (photolysis rate) constant. Unfortunately, absorbance changes in CARs during exposure have been found to have little correlation to the amount of photoacid generated[47], making the Dill C parameter irrelevant to acid generation. Thus, other means of quantifying acid generation upon exposure have been developed.

Several successful methods for the direct measurement of the photogenerated acid have been published. Thackeray *et al.*[17], Cameron *et al.*[18], Eckert *et al.*[19], Okoroanyanwu *et al.*[20] and Pohlers *et al.*[21] have all proposed techniques for quantifying the photogenerated acid using absorbing or fluorescent dyes as indicators. Szmanda *et al.* proposed a method similar to the "standard addition" method. In this method, base quencher of varying amounts are added to the resist and the dose-to-clear (E_0) is measured to monitor the acid concentration[16]. Byers and co-workers have also successfully used FTIR spectroscopy to quantify the amount of acid generated during exposure[22]. The above techniques for determining acid concentration have helped in successfully modeling and quantifying the exposure of CARs.

11

2.4. Modeling the Post Exposure Bake

CARs make use of an acid catalyzed reaction during the post exposure bake (PEB) to achieve lithographically acceptable sensitivities[8]. Results of several reaction kinetics studies have been published to support the PEB modeling of CARs. Some of the early investigations on the reaction kinetics were performed by Willson[23], Fedynyshyn[24] and Reichmanis[25]. Seligson *et al.* demonstrated that a reciprocity existed between the exposure dose, the bake temperature, and the bake time and expressed this reciprocity mathematically as an "effective dose" [26]. Fukuda *et al.* described models based on contributions from photon and thermal energy[27]. Both Trefonas and Szmanda have developed models based on percolation theory, which relates dissolution behavior to threshold levels of extent of reaction[28][29].

Cerrina[28], Watanabe[29] and Ferguson[30] proposed models based on reaction rate kinetics which lead to coupled differential equations. Ferguson proposed a mechanistic reaction model to account for the extent of reaction from data obtained from Fourier transform infrared (FTIR) spectroscopy measurements[31]. Although many reactions can take place during the PEB, a simplified kinetic model for the rate limiting step results in a differential equation of the following form[24]:

Equation 2-4.
$$\frac{\partial A}{\partial t} = k_r(1-A)H^m$$

where A is the normalized reacted (activated) sites concentration, H is the acid concentration, k_r is the reaction rate constant and m is the reaction order.

Several studies of various CAR systems have shown that even under large area exposure conditions on anti reflective coatings where one would expect negligible changes

in the acid concentration during PEB, significant changes still occur[32][33]. The local

concentration of acid can change due to volatilization and loss mechanisms during PEB.

Thus, modeling of the time evolution of the acid has to take into account a quenching effect

of the reaction which is observed experimentally. Such a model can be expressed as fol-

lows[8]:

Equation 2-5.
$$\frac{\partial H}{\partial t} = -k_l H$$

where k_l is the acid loss rate coefficient.

In addition to reaction kinetics and acid loss mechanisms, acid diffusion effects also

play an important role in determining the final resist image. Thus, the effects of acid diffu-

sion on the time evolution of the acid concentration and the appropriate boundary condi-

tions that account for acid outdiffusion on the surface has to be included to provide a

complete set of model-equations to describe the PEB process. Mechanistic based diffusion

models explicitly include a description of the acid flux during the PEB as shown in the fol-

lowing expression[8]:

Equation 2-6.
$$\frac{\partial H}{\partial t} = \nabla(D(PEB)\nabla H)$$

where $D(PEB)$ is a general expression for the acid diffusivity as a function of the state and

processing conditions[34][35][36]. For positive CARs, it has been postulated that the

diffusivity of the photoacid generator changes as a function of the extent of polymer

deprotection[34][38]. Hinsberg *et al.* suggested that diffusivity increases exponentially

with reacted material[37]. Several equations have been proposed to provide a set of

complete model equations for the PEB process. Zuniga *et al.* proposed the following model[8]:

$$\frac{\partial A}{\partial t} = k_r(1-A)H^m$$

$$\frac{\partial H}{\partial t} = \nabla(D\nabla H) - k_l H$$

$$D = D_0 \exp(\omega A)$$

$$D_0 = A_r \exp\left(-\frac{E_a}{RT}\right)$$

Equation 2-7.

where D_o is the diffusivity constant, A_r is the Arrhenius coefficient, E_a is the activation energy and ω is a fitting parameter. D is a non-Fickean diffusivity and is assumed to be an exponential function of the activated sites concentration, A.

Mack employs variations of this PEB model in developing a PEB process simulator PROLITH[4]. The equations used in PROLITH are as follows:

$$\frac{\partial A}{\partial t} = k_r(1-A)H^m$$

$$\frac{\partial H}{\partial t} = \nabla(D\nabla H) - k_l H$$

$$D = D_0 + A(D_f - D_0)$$

$$D = D_0 \exp\left(\frac{\alpha A}{1+\beta A}\right)$$

$$D = D_0 = A_r \exp\left(-\frac{E_a}{RT}\right)$$

Equation 2-8.

14

Here, the user has a choice among algebraic, exponential and Fickean diffusion expressions.

Petersen et al. proposed the following model for the PEB process[39]

$$\frac{\partial M}{\partial t} = -\frac{\sigma D k_r}{\sigma D + k_r} HM$$

$$\frac{\partial H}{\partial t} = -k_l QH + D\nabla\nabla H$$

$$D = RTA\exp\left(\frac{-B_d}{V_g + \alpha(T - T_g)}\right)$$

$$k_r = A_r\exp\left(-\frac{E_r}{RT}\right)$$

Equation 2-9. $\quad k_l = A_l\exp\left(-\frac{E_l}{RT}\right)$

where diffusion is assumed to be Fickean but changes with the glass transition temperature. M is the reactive site concentration and Q is the quencher concentration.

A fundamental difficulty in quantifying the changes in the acid concentration during PEB is that the motion of the acid cannot be measured directly and must be inferred from either CD measurements of specialized exposure experiments or bulk measurements of the resist chemical and/or electrical properties[32]. Numerous studies have character-ized CD behavior as a function of PEB conditions. A series of publications by Shlegel showed that the diffusion coefficient for various acids ranged from 10^{-4} to 10^{-7} $\mu m^2/s$

depending on the PEB temperature and specified acid structure[40][41]. Typical diffusion

values for positive tone resist have been reported by Fedynyshyn to be $\sim 10^{-3} \, \mu m^2 / s$ [36].

There is a considerable body of literature regarding modeling of diffusion in polymeric materials. Much of this work incorporates free volume ideas into the description of diffusion[43][45]. A collaborative work between University of California at Berkeley TCAD Group and University of Texas at Austin Resist Synthesis Group on modeling chemically amplified resist led to the development of continuum-based models[91] and molecular level models[48] that incorporates free volume concepts.

2.5. Free volume enhanced PEB model

2.5.1. Introduction

Most of the models presented in Section 2.4 differ only in the type of diffusion used to describe the acid transport mechanism. The transport has been described by simple Fickean to algebraic and exponential concentration dependent diffusion models. Zuniga documented CD dependence on PEB conditions and found that for most chemically amplified resists, Fickean model does not adequately describe effects of PEB on linewidth[8]. He found that experimental data on PEB effects on linewidth were best fitted by case II type diffusion models whereby it is assumed that the diffusivity of the acid is an exponential function of the deprotection product. Unfortunately, the product of the deprotection of t-BOC and APEX (typical protecting groups in CAR) is polyhydroxysterene (PHOST) and recent experiments documented negligible acid diffusivity in PHOST[44]. They report diffusion coefficients $D \leq 10^{-8} \dfrac{\mu m^2}{s}$. Yet, line width growth with PEB time is well docu-

mented[8]. This leads to the conclusion that there must be some unique characteristic of the zone in which the reaction takes place. The experiments leading to this concept is further elaborated by Postnikov *et al.*[44].

The models described so far take the phenomenological modeling approach where equations are established to reproduce experimental phenomena. Another approach is to make assumptions about fundamental mechanisms governing the process and derive the necessary chemical and differential equations. This thesis proposes a generalized model for latent image formation in chemically amplified resists. The model is based on a moving boundary acid transport concept that incorporates transient free volume generation and densification. It is based on experimental observation of negligible acid diffusion in polyhydroxysterene below T_g. The model offers insight into the PEB reaction mechanism that governs the relief image formation in chemically amplified resists. During post exposure bake, there is a thermally induced deprotection catalyzed by the photo-generated acid that produces volatile by-products thereby generating free volume in the resist polymer. The free volume enhances local diffusivity of the acid. The rapid loss of the volatile products is followed by relaxation of the polymer matrix which eliminates the transient free volume and densifies the polymer. The densified polymer inhibits the diffusion of any acid trapped in the deprotected sites. Cases are presented where the model reduces to Fickean and case II type reaction driven diffusion models under some simplifying assumptions. The model was implemented in STORM (Simulation Tools for Optical Resist Models) to simulate 1D and 2D profiles. The results imply that the relief image formation depends strongly on both the mechanical the chemical properties of the resist. This model provides new directions for resist process optimization.

2.5.2. Model Description

CAR systems are characterized by a trade-off between process latitude and exposure sensitivity. Sensitivity increases by increased post exposure bake (PEB) temperature but unfortunately, the sensitivity increase is accompanied by loss of exposure latitude. This degradation in process latitude with increasing temperature is attributed to the enhancement of acid diffusion at higher temperatures. The impact of diffusion (blur) on smaller feature sizes has led to intensive investigations of the PEB reaction/diffusion process in attempt to gain better understanding of the physical parameters affecting relief image formation.

The proposed model is based on the following assumptions. During PEB, the photogenerated acid (H) catalyzes a thermally induced reaction that removes the protecting groups (P) and creates deprotected sites (A). Volatile by-products (V) are created during this reaction. The volatile fragments have appreciable mobility in polymer. Thus, they desorp fairly rapidly from the resist material, generating a transient free volume (F) in the reaction zone[43]. PEB temperatures are below the glass transition temperature (T_g) of the resist, the resist is considered to behave as a glassy polymer. Glassy polymers do not respond immediately to change in their equilibrium state[12]. Thus, densification and elimination of free volume after the volatile group desorption is not instantaneous. The rate of densification will be characterized by a relaxation rate constant (k_x) which is assumed to be inversely proportional to the polymer relaxation time. If this relaxation time is large compared to the characteristic diffusion time, then significant diffusion of the acid can occur before the polymer densification suppresses the diffusion and prevents the acid in the densified region from taking further part in the diffusion process. Thus, while

the acid concentration remains essentially constant during PEB, only a limited number of acid molecules, those at the deprotected/protected interface, can freely diffuse. This is because after the densification of the initially exposed region of the resist, acid molecules in this region are immobilized. The free volume needed to facilitate acid transport is generated only at the deprotected/protected reaction zone.
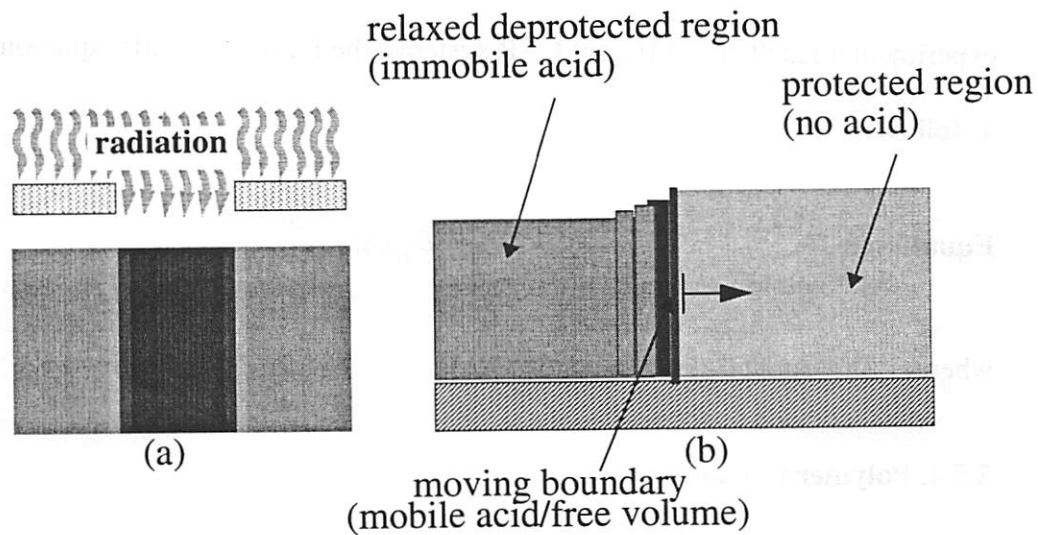
Figure 2-2. Free volume acid transport concept.

a) initial acid concentration gradient. (b) physical mechanisms governing acid transport.

Figure 2-2b illustrates this process. It is assumed that a sharp boundary surface moves through the resist polymer. This boundary separates a densified region in which all acid molecules are immobile from one in which the acid concentration is zero.

2.5.3. Diffusivity model

The influence of free volume on the diffusion properties of glassy polymers is described in[43]. As explained above, the rapid desorption of the volatile by-products during reaction creates free volume in the reaction zone. Though the local relaxation rate

of the reacted sites will be much faster than a truly glassy material, it is assumed that the local reduction in T_g enhances the mobility of the acid molecules, allowing them to use the free volume as 'stepping stones' to traverse the deprotected/protected boundary. This suggests a dependence of the diffusivity on the free volume concentration. A diffusion model that can be predicted theoretically using T_g and free volume arguments is the Fujitu-Doolittle equation[46]. To present a general diffusion model that is consistent with experimental results for different CAR systems, the Fujitu-Doolittle equation is adapted as follows:

Equation 2-10.
$$D = D_o \exp\left(\frac{\omega F}{1 + \upsilon F}\right)$$

where D_o, ω and υ are constants.

2.5.4. Polymer relaxation

PEB model described above consists of two complex moving boundary problems; one in which the deprotected zone (deprotected/protected interface) advances inside the resist material and another in which deprotected regions continuously shrink. (i.e., no conservation of volume). The characteristic time needed for the polymer matrix to reorganize itself to eliminate the free volume is related to the polymer relaxation rate constant (k_x). It is assumed the volume shrinkage rate at the deprotected/protected interface to be proportional to the free volume concentration, given by

Equation 2-11.
$$\frac{\partial}{\partial t} Vol = -\beta k_x F$$

20

where *Vol* is the volume at the moving zone and β is a parameter proportional to the size of the volatile group molecules desorbing from the resist. The induced forces and possible stress and strain fields at the reaction front due to local polymer densification must be related to the mechanical properties of the resist polymer to emulate the global polymer deformation. The following linear momentum balance equation is used to model the polymer deformation[49].

Equation 2-12.
$$\int_w \delta\dot{\varepsilon} \cdot \sigma = \int_\Gamma \delta(v) \cdot f + \int_w \delta(v) \cdot b$$

$\dot{\varepsilon}$ is the strain rate, σ is the stress, v is the velocity, Γ is the boundary, f is the boundary force and b is the body force.

2.5.5. Differential Equations

The physical models explained above translate to the following chemical equations:

$$P + H \xrightarrow{k_r} V + A$$

$$V \xrightarrow{k_{des}} F$$

Equation 2-13.
$$F \xrightarrow{k_x} (zero)$$
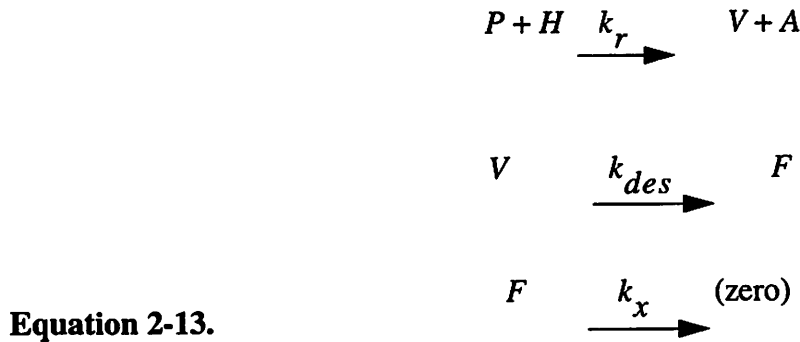
The following set of coupled nonlinear partial differential equations describes the proposed PEB model:

$$\frac{\partial P}{\partial t} = -k_r PH$$

$$\frac{\partial V}{\partial t} = k_r PH - k_{des} V$$

$$\frac{\partial F}{\partial t} = k_{des} V - k_x F$$

$$\frac{\partial H}{\partial t} = \nabla(D\nabla H)$$

$$\frac{\partial A}{\partial t} = k_r PH$$

$$k_r = k_0(1 - exp(-\alpha H))$$

$$D = D_0 exp\left(\frac{\omega F}{1 + \upsilon F}\right)$$

$$\frac{\partial}{\partial t} Vol = -\beta k_x F$$

Equation 2-14.
$$\int_w \delta\left(\frac{\partial}{\partial t}\dot{\varepsilon}\right) \cdot \sigma = \int_\Gamma \delta(v) \cdot f + \int_w \delta(v) \cdot b$$

2.5.6. Boundary Conditions

The air-polymer interface can be described by assuming that the flux of the acid groups is driven by the acid concentration, free volume concentration and base contaminants near the air-polymer interface. It is modeled as

Equation 2-15.
$$-D\left(\frac{\partial H}{\partial n}\right)_{\text{int air-polymer}} = -k_1 HF - k_2 H$$

where k_1 and k_2 are parameters for acid loss due to desorption and base contamination respectively. Assuming impermeable boundary conditions at the substrate polymer interface, one gets

$$-D\left(\frac{\partial H}{\partial n}\right)_{\text{int surface-polymer}} = 0$$

$$-D\left(\frac{\partial V}{\partial n}\right)_{\text{int surface-polymer}} = 0$$

Equation 2-16.

2.5.7. 1D simulation results

Figure 2-3 gives the profiles of acid groups, protected groups, volatile groups, free volume content, and deprotected sites versus the distance into the initially protected t-BOC for the following conditions: $D_f = 1\times10^{-4}\frac{\mu m^2}{s}$, $D_v = 1\times10^{-2}\frac{\mu m^2}{s}$, $k_o = 2.0\frac{\mu m^3}{s}$,

$k_{des} = 10.0\frac{1}{s}$, $k_x = 2\frac{1}{s}$, $\alpha = 10.0$, $\omega = 5.0$, and $v = 1.0$. The PEB time is 60s and the simulation performance is under 30 seconds for this 1-D case on a 600MHz machine. The time arrows in these figures illustrate the time evolution of the species. The acid concentration profile shows acid diffusion only at the front where free volume content is being

23
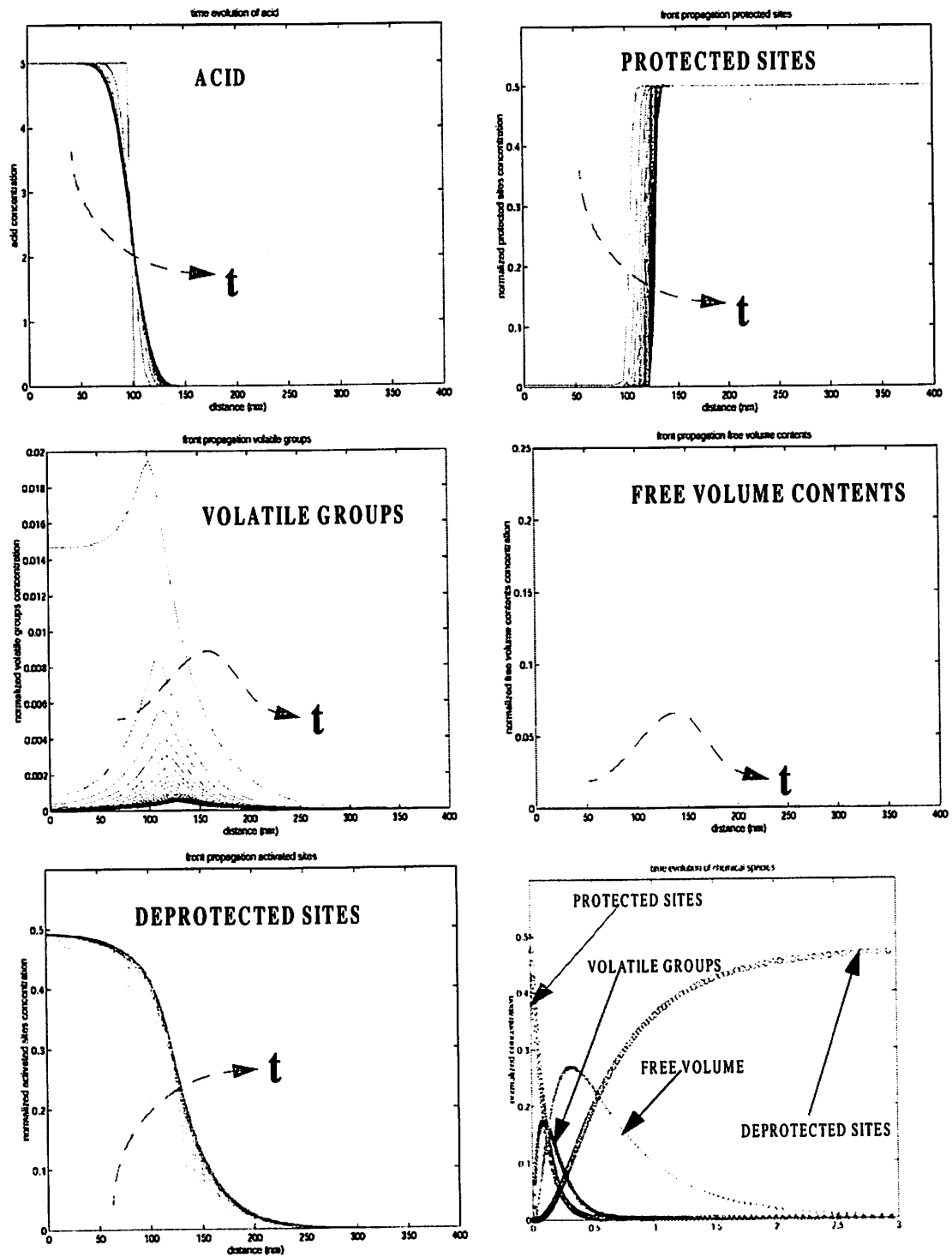
Figure 2-3. Front propagation of species

Front propagation of species. (a) Acid sites concentration. (b) Protected sites concentration. (c) Volatile group concentration. (d) Free volume concentration. (e) Deprotected sites concentration. (f) Time evolution of species at a fixed node

24

generated. The acid behind the front is immobile and maintains the initial profile for all times. The protected groups concentration profiles and the deprotected sites concentration exhibit a very sharp moving boundary between deprotected and protected regions. The volatile groups and the free volume content exhibits traveling waves of changing profiles that rise and decay with time. The time evolution of the species at a fixed site (Figure 2-3f) illustrates this phenomena.

The underlying physical mechanisms of the above model provide rigorous foundation for first principle based simulations. Understanding the physical mechanisms was a result of a collaborative work between University of California at Berkeley TCAD Group and University of Texas at Austin Resist Synthesis Group on modeling chemically amplified resist. This work led to the development of continuum-based models[91] and molecular level models[48] that incorporates free volume concepts. For the continuum simulation approach of interest in this thesis, where the speed of the simulator as well as the ease of quantifying model parameters is of great concern, the above model, though rigorous, has far too many parameters to make calibration practical. Furthermore, experimental techniques for extracting some of the parameters such as free volume coefficients are not available. Even if these techniques were readily available, the number of wafers that must be used to extract the model parameters independently makes the model prohibitively expensive for practical use. The remaining sections of this chapter makes basic assumptions to reduce that number of parameters. Analytical expressions will also be derived.

2.6. Simplified PEB Models

The proposed models attempt to capture the physical mechanisms of the PEB process at the expense of higher complexity in the model. The number of parameters needed to apply the above model to existing resist systems is too large, making design of experiments (DOE) for parameter extraction prohibitively expensive. Basic assumptions have to be made to simplify the model to make it practical.

2.6.1. Moving Boundary Transport (MBT) Model

The following assumptions are made in order to simplify the model:

1. Desorption rate (k_{des}) of the volatile fragments is much faster than the relaxation

   rate (k_x) (i.e. instantaneous desorption of volatile groups)

2. The effects of acid loss to ambient on PEB are negligible

3. Base contamination in the ambient is negligible

Assumption (1) allows us to ignore the volatile group concentration and model the chemical reaction as:

$$P + H \xrightarrow{k_r} A + F$$

Equation 2-17. $$F \xrightarrow{k_x} (zero)$$

Since there is a direct conversion of protected groups (P) to deprotected groups (A), one can also ignore keeping track of the protected group concentration by representing it as ($1-A$), which is normalized protected group concentration. Assumptions (2) and (3)

26

allow the boundary condition parameters to be set to zero. These assumptions lead to the following simplified set of equations which will be referred to as the MBT (moving boundary transport) model in subsequent sections

$$\frac{\partial A}{\partial t} = k_r(1-A)H$$

$$\frac{\partial F}{\partial t} = k_r(1-A)H - k_x F$$

$$\frac{\partial H}{\partial t} = \nabla(D\nabla H)$$

$$\frac{\partial}{\partial t}Vol = -\beta k_x F$$

$$D = D_0 exp\left(\frac{\omega F}{1+F}\right)$$

$$\int_w \delta\dot{\varepsilon}\cdot\sigma = \int_\Gamma \delta(v)\cdot f + \int_w \delta(v)\cdot b$$

Equation 2-18.

2.6.2. Case II type diffusion models

It is interesting to note that the general MBT model reduces to the Case II model in [50] under some simplifying assumptions. If an assumption is made that the volatile group by-products have negligible effects on the PEB reaction/diffusion kinetics, a simpler set of equations can be derived. The only drawback of this assumption is that for long enough PEB times, the model will predict that the acid will diffuse through the entire resist and deprotect it. Since experimental data show that deprotection of unexposed regions of the resist saturates for long PEB times[51][52], some other acid loss assumption has to be

27

incorporated in the model to make it useful. Furthermore, a non-integer reaction order has to be introduced to better match experimental results. These assumptions produce the following set of chemical and differential equations used by Zuniga *et al.* [50] to describe the PEB process.

Equation 2-19.

$$P + H \xrightarrow{k_r} A$$

$$\frac{\partial A}{\partial t} = k_r (1 - A) H^m$$

$$\frac{\partial H}{\partial t} = \nabla (D \nabla H) - k_l H$$

$$D = D_0 exp(\omega A)$$
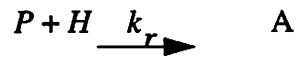
Equation 2-20.

Here m is the reaction order and k_l is the acid loss rate constant. In fact, if ω is chosen to be zero (D is constant), then the above model collapses to the Fickean diffusion model of PEB described in the literature[53]. Otherwise, D is chosen to be exponential function of the deprotected group concentration and the above model becomes the Case II type diffusion PEB model available in the literature[50].

Although this model was phenomenologically derived to match experimental results, whereby acid quenching had to be incorporated as well as a fitting parameter m, a similar but mechanistic based set of equations can be reached when one considers a class of DUV

resists where a base quencher is deliberately introduced to retard acid migration. For this class of resists, the chemical equations are:

$$P + H \xrightarrow{k_r} A$$

Equation 2-21.
$$H + B \xrightarrow{k_l} \text{(zero)}$$

resulting in the following set of equations.

$$\frac{\partial A}{\partial t} = k_r(1 - A)H$$

$$\frac{\partial H}{\partial t} = \nabla(D\nabla H) - k_l BH$$

$$\frac{\partial B}{\partial t} = -k_l BH$$

$$D = D_0 exp(\omega(1 - A))$$

Equation 2-22.

The difference between the two sets of equations is that the quencher concentration is explicitly expressed in Equation 2-22 and the fitting parameter is no longer needed.

The form of the diffusivity equation is of importance since it determines how well the models can predict experiments over a given range of process conditions. The forms introduced are

Equation 2-23.
$$D = D_0 exp\left(\frac{\omega F}{1 + \upsilon F}\right)$$

from Equation 2-14,

Equation 2-24.
$$D = D_0 exp(\omega A)$$

29

from Equation 2-20 and

Equation 2-25. $$D = D_0 exp(\omega(1-A))$$

from Equation 2-22. Equation 2-23 give the most accurate prediction over a wide range of process conditions since it is theoretically derived from free volume arguments. However, the transient free volume content during PEB is not easy to quantify from experiments and thus calibrating the ω and υ presents a big challenge. Furthermore, the additional parameter, υ, makes its use unattractive. A simple simulation comparisons to Equation 2-23 shows that Equation 2-25 agrees better with Equation 2-23 than Equation 2-24 for longer PEB times as shown in Figure 2-4. This is because Equation 2-25 emulates acid transport retardation due to polymer densification after deprotection as described in Section 2.5.2. Thus, Equation 2-22 provides better prediction of experimental data and is simple enough to make its use practical.

2.6.3. Analytical expressions for PEB

In this section an analytical expression of the model Equation 2-22 is derived. In the absence of diffusion, Equation 2-22 yields the following analytical solution for the
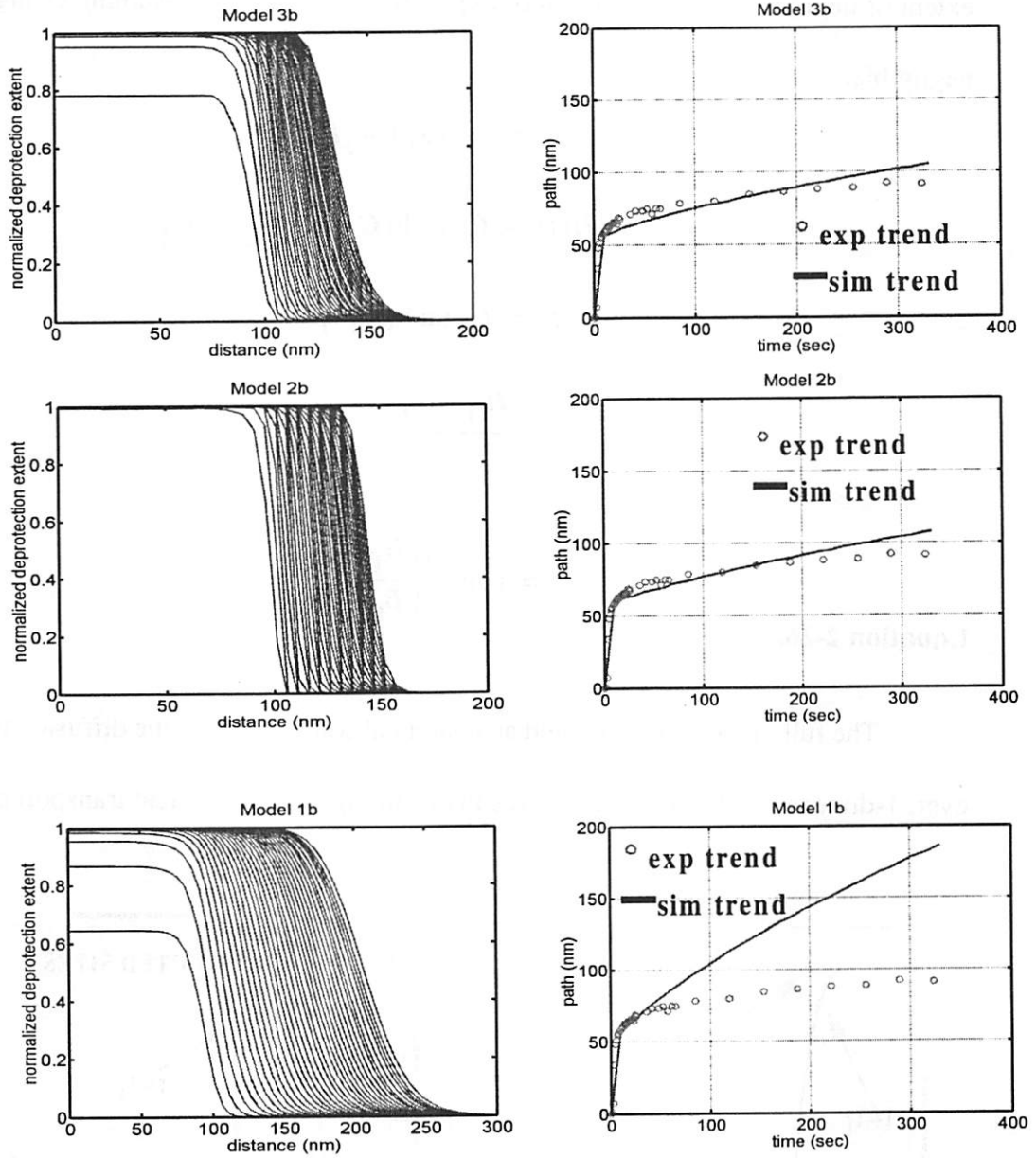
Figure 2-4. Diffusivity Model Profiles

(a) $D = D_o \exp\left(\dfrac{\omega A}{(1 - \eta A)}\right)$. (b) $D = D_o \exp(\omega(1 - A))$. (c) $\quad D = D_o \exp(\omega A)$

31

extent of deprotection as a function of exposure dose and time, assuming changes in H is

negligible.

$$A(t) = 1 - \exp(-k_r H t)$$

$$H(t) = C_1 \tanh(C_1 k_I t - C_2) + C_1$$

$$B(t) = C_1 \tanh(C_1 k_I t - C_2) - C_1$$

$$C_1 = \frac{H_0 - B_0}{2}$$

$$C_2 = \tanh^{-1}\left(\frac{H_0 + B_0}{B_0 - H_0}\right)$$

Equation 2-26.

The full model does not yield an analytical solution due to the diffusion term. However, 1-dimension (1-D) simulation results from Figure 2-3 and acid transport experimen-

(a)   (b)
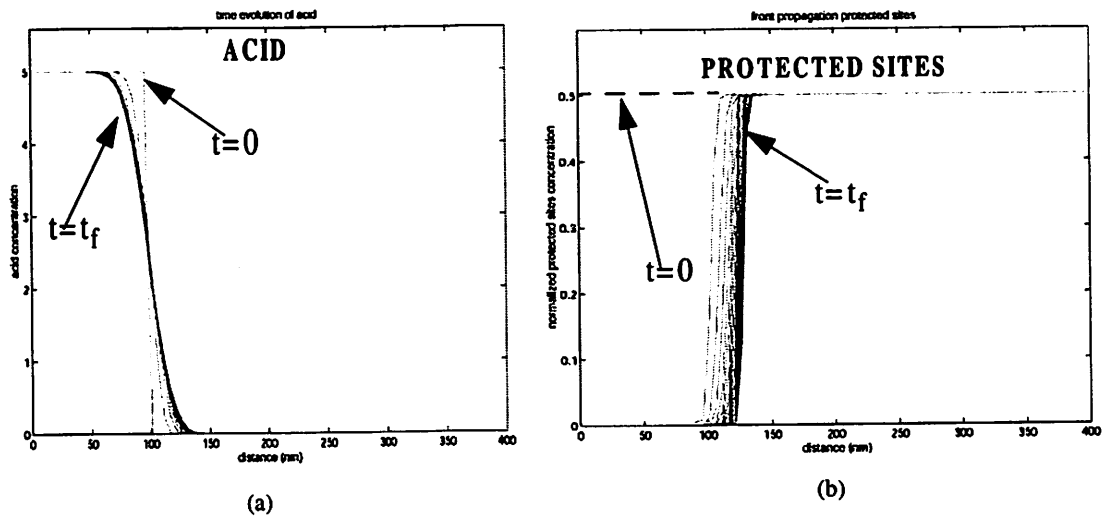
Figure 2-5. Assumption Illustration for Analytical Model Derivation

(a) Acid concentration profile evolution. tf is the bake time (b) Protected sites concentration profile evolution.

tal data suggests that the protected/deprotected interface exhibits a reaction front propagation phenomena (i.e. the deprotected/protected interface behaves like a travelling wave propagating in the direction of unexposed resist region)[54]. Thus, if one can cast the equations in the wave equation form, one can obtain analytical expression for the propagation speed as a function of the PEB parameters. To do this, let's rewrite the model equations in the following form to keep track of the protecting group concentration:

Equation 2-27.
$$\frac{\partial A}{\partial t} = k_r PH$$

Equation 2-28.
$$\frac{\partial H}{\partial t} = -k_l HB + \nabla(D\nabla H)$$

Equation 2-29.
$$\frac{\partial P}{\partial t} = -k_r PH$$

Equation 2-30.
$$D = D_0 \exp(\omega P)$$

The influence of the base quencher, B, is assumed negligible so that its time rate of change can be ignored in the above equations. These equations are solved using STORM's 1-D simulator. The acid and protected sites concentration profiles are shown in Figure 2-5. The sharp boundaries exhibited by these profiles justify the following assumptions. From Equation 2-27,

Equation 2-31.
$$\frac{\partial^2 A}{\partial t^2} = k_r H \frac{\partial P}{\partial t} + k_r \frac{\partial H}{\partial t} P$$

Substituting Equation 2-28 and Equation 2-29 gives

Equation 2-32.
$$\frac{\partial^2 A}{\partial t^2} = k_r P \left(H^2 k_r + \frac{\partial}{\partial x}\left(Do\exp(\omega P)\frac{\partial H}{\partial x}\right) - k_l HB \right)$$

Assuming the gradient term dominates at the interface and simplifying, gives

Equation 2-33. $$\frac{\partial^2 A}{\partial t^2} = k_r Do \exp(\omega P) P \left(\frac{\partial^2 H}{\partial x^2} - \omega \frac{\partial A}{\partial x} \frac{\partial H}{\partial x} \right)$$

At the interface, it is assumed (see Figure 2-5) that

Equation 2-34. $$-\frac{\partial P}{\partial x} \approx \frac{\partial H}{\partial x}$$

Assuming sharp interfaces can be approximated by exponential decay function, it can be shown that

Equation 2-35. $$\frac{\partial^2 A}{\partial x^2} \approx \left(\frac{\partial A}{\partial x} \right)^2$$

These assumptions give

Equation 2-36. $$\frac{\partial^2 A}{\partial t^2} = k_r Do (1-A)(1-\omega) \exp(\omega(1-A)) \frac{\partial^2 A}{\partial x^2}$$

which yields the following expression for the propagation speed.

Equation 2-37. $$\frac{dx}{dt} = \sqrt{k_r Do(1-A)(1-\omega)\exp(\omega(1-A))} \qquad (\omega < 1)$$

The analytical expressions provide the means of quickly evaluating the effects of PEB on LES and can be useful for optical proximity correction (OPC) applications. When Equation 2-26 and Equation 2-37 were evaluated in MATLAB to simulate PEB effects on LES, good predictions of the experimental data were achieved provided that optimal parameters of D_0 are used for each dose. A look-up table generated for D_0 using the non-

OPC LES data is presented in Table 1. The dependency of D_0 on exposure dose, D_e, was found to be

$$D_0(D_e) = 4.75 \times 10^{-6} D_e - 3.93 \times 10^{-6}$$

The result is plotted in Figure 2-6.
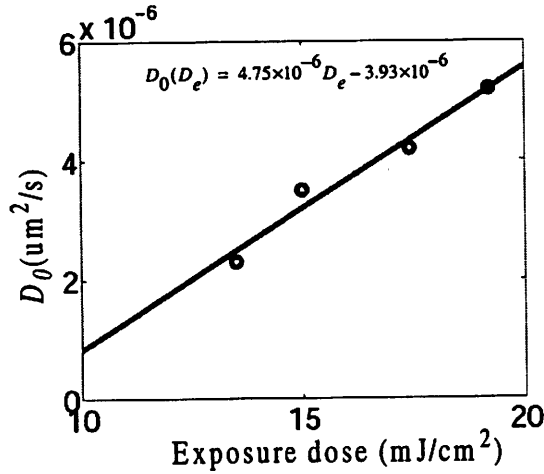
Figure 2-6. D_0 dependency on exposure dose for analytical PEB model applications.

This formula was used for D_0 in Equation 2-37 to simulate OPC features. The results will be discussed in Chapter 5, along with the limitations of the model.

TABLE 1. Look-up table for D_0 for analytical model evaluations

Dose(mJ/cm^2)	13.5	15.0	17.4	19.2
D_0 ($\mu m^2/s$)	2.3×10^{-6}	3.5×10^{-6}	4.2×10^{-6}	5.2×10^{-6}

2.7. Software and Applications

The transition in optical lithography from 248nm to 193nm wavelength renewed interest in top surface imaging lithography using silylation. During this transition, there was a strong interest in modeling support to aid in the development of TSI materials. Thus,

the initial project leading to the work in this dissertation was the development of a silylation simulator (co-developed with Marco Zuniga) based on moving boundary concepts. This made possible the study of effects of stress on reaction and diffusion mechanisms to understand lithography issues such as process trends on feature types and sizes. The advent of transparent materials at 193nm lithography directed this dissertation work to accommodate development of efficient mechanistic based chemically amplified resist simulators to address 193nm resist issues such as acid diffusion and line end shortening. The program is named STORM, for Simulation Tools for Optical Resist Models. Its goal is to develop software tools to provide quantitative support for deep submicron resist process modeling.

STORM version 1.0 was released in June 1998 through the Industrial Liason Program at the University of California at Berkeley. The principal components include SPLAT for exposure simulation, BAKE for post exposure bake simulation and SILY for silylation simulation. X-Window plotting programs such as CONTOUR is also included in the software release for visualization of simulation results. STORM version 2.0 was released in December 1999. The new release adds etch capabilities in O2ETCH to allow for oxygen reactive ion etching of top surface imaged resist, making TSI and bilayer resist process simulations possible.

The computer programs for O2ETCH, SILY and BAKE solve a set of chemical kinetics nonlinear partial differential equations using the finite element method for space discretization and a backward difference formula time advancement scheme for time discretization. In addition to the chemical kinetics equations, SILY also solves the virtual power equations to determine the mechanical stress fields and polymer deformation.

O2ETCH also utilizes Monte Carlo methods to simulate the ion bombardment during the etching process. The simulation domain is 2-dimensional and may be a cross section or a top view of a photoresist.

STORM is designed for use on engineering workstations running under the Unix operating systems. The plotting program requires the X window system. Memory requirements depends on the number of nodes approximating the simulation domain. Practical simulations require between 1 and 200 megabytes of physical memory. Run times depends on machine, problem size and simulation parameters. A typical BAKE simulation runs under 1 minute on 600MHz DEC Alpha, under 1 minute on 700MHz Pentium III PC running unix emulator CYGWIN, and under 4 minutes on a 200MHz Sun Ultra Sparc machine (676 finite element domain nodes).

STORM version 1.0 and version 2.0 were released without graphical user interface (GUI); the user must execute the programs by modifying the appropriate input parameter files. The included software tools may be run as separate stand alone programs. Communication between programs is primarily through files. This form of information transfer allows intermediate steps to be saved and retrieved for later use.

The STORM programs have been successfully ported onto Microsoft Windows platform using unix emulator CYGWIN and can now be accessed from the (Lithography Analysis through Virtual Access) LAVA website at http://cuervo.eecs.berkeley.edu.

3 Top Surface Imaging Modeling

3.1. Introduction

Lithographic processes combining silylation and dry development have yielded promising results which extend the limits of the lithographic tools[55]-[57]. Top surface imaging techniques achieve insensitivity to underlying topography and thereby increase focus and exposure latitude. Lateral encroachment into ideally isolated regions has stimulated many studies of processing approaches and conditions. However, a better understanding of the mechanisms which govern uptake of the silylating agent in the polymer matrix would help to simplify the choice of processing conditions and facilitate the design of an optimum resist.

Silylation is the process of incorporating silicon containing compound into a resist polymer. This is an important process in the top surface imaging (TSI) lithography process whereby upon exposure, the latent image is formed at the near top region of the resist. A silicon containing compound in the gas or liquid phase is diffused into the polymer and the silicon is selectively incorporated into the exposed region (negative tone) or unexposed region (positive tone) of the resist. The silicon containing region forms a SiO_2 barrier to protect the underlying resist from etching during a dry development step in an O_2 plasma.

Figure 3-1 illustrates positive tone and negative tone TSI processes. For the negative tone

EXPOSURE AND PEB

SILYLATION

DRY DEVELOPMENT

(a)   (b)
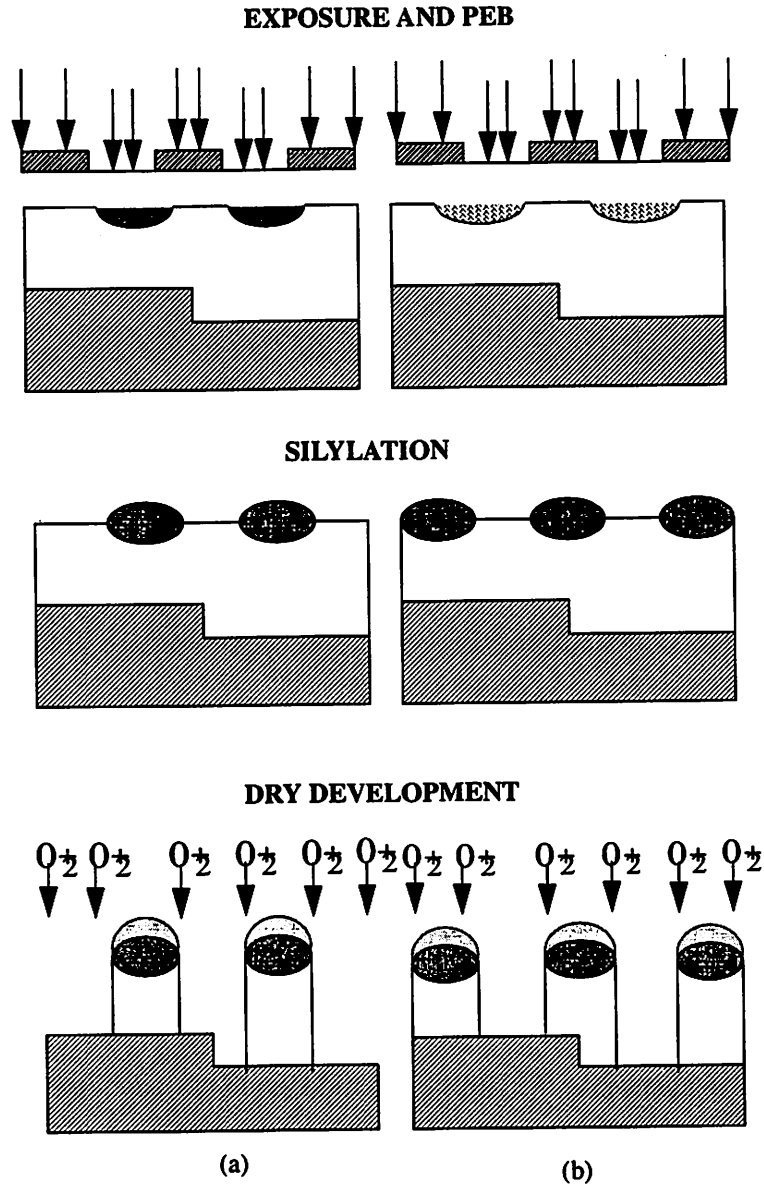
Figure 3-1. Top Surface Imaging

(a) Negative tone non-diffusion enhanced TSI scheme. (b) Positive tone diffusion enhanced TSI scheme.

process, the exposure and post exposure bake activates functional groups that are capable

of reacting with the silylating agent. During silylation, the silicon is selectively incorpo-

39

rated in the exposed region. Subsequent dry development process etches the unexposed region away, resulting in a negative tone process. For the positive tone TSI process (Figure 3-1b) the resist crosslinks upon exposure. During silylation, the crosslinked region inhibits the diffusion of the silylating agent, allowing selective incorporation of silicon in the unexposed region. During the dry development process, the non silylated region is etched away, resulting in a positive image.

Recent silylation modeling efforts have been empirical in nature. Weib *et al.* have proposed a reaction dominated propagation model which describes the evolution of the silylated area as a propagation of the layer boundary with a photoactive compound (PAC) dependent velocity[58]. Simakov *et al.*[59] model silylation uptake as reaction diffusion process, utilizing solutions to the diffusion equations assuming an infinite source of silicon at the surface to obtain expressions for silicon concentration versus time throughout the resist film. McDonaugh *et al.*[60] modeled the silylation step using linear interpolation of silylation rates as predicted by the DESIM model[61]. Reaction-diffusion models proposed by Jaghold *et al.*[62] and Pierrat[98] include gas phase incorporation and diffusion of the silylating agent into the film. Such models do not adequately explain the experimentally observed dependence of silylation depth and final resist profile as a function of feature size and feature type as observed by Hartney[64].

Like the PEB process described in Chapter 2, silylation is a moving boundary problem in which the larger molecule silylating agent continuously expands the resist polymer while a sharp silylated/unsilylated front propagates inside the resist[65]. A comprehensive model for a negative tone silylation process was first presented by Pierrat [66]. This model

40

takes into account the reaction of the silylating agent with the hydroxil groups of the polymer and the relaxation of the polymer after reaction. Zuniga *et al.* proposed a two dimensional extension of the model to take into account possible stress induced reaction retardation due to polymer swelling[67]. The underlying assumptions of these models are that the silylating agent (S) reacts with the hydroxil groups (H) to form unexpanded sites (U). The unexpanded sites then relax with some relaxation time constant, t_r, to form expanded sites (E). The chemical equations describing this process is as follows:

Equation 3-1.
$$S + H \xrightarrow{K_1} U$$
$$U \xrightarrow{t_r} E$$

The resulting set of differential equations are[34]:

Equation 3-2.
$$\frac{\partial S}{\partial t} = \nabla(D_0 \exp(\omega E)\nabla S)$$

Equation 3-3.
$$\frac{\partial H}{\partial t} = -K_1 SH$$

Equation 3-4.
$$\frac{\partial U}{\partial t} = K_1 SH - \frac{U}{t_r}$$

Equation 3-5.
$$\frac{\partial E}{\partial t} = \frac{U}{t_r}$$

Equation 3-6.
$$\frac{\partial A}{\partial t} = \frac{A_f - A_i}{E_{max}} \frac{U}{t_r}$$

Equation 3-7.
$$\int_w \delta(\dot{\varepsilon}) \cdot \underline{\sigma} = \int_\Gamma \delta(v) \cdot f + \int_w \delta(v) \cdot b$$

Equation 3-8.
$$k_r = A exp\left[-\frac{(Ea_1 - B\sigma)}{KT}\right]$$

where D_o is the silicon intrinsic diffusivity in the unsilylated film, K_I is the reaction rate, t_r is the polymer relaxation time, ω is the reaction-diffusion coupling coefficient, and B is the stress-reaction coupling coefficient. $\underline{\sigma}$ is the stress matrix and σ is a scalar measure of $\underline{\sigma}$. Resist swelling, as modeled by Equation 3-6, is supposed to give rise to stress and strain fields as a function of the local deformation, as calculated by Equation 3-7. As illustrated in Equation 3-8, such stress fields are supposed to lead to a local reduction in the reaction rate by linearly changing the activation energy of the process. The silylated/ unsilylated boundary propagation is modeled by the nonlinear diffusive transport as shown in Equation 3-2. This local enhancement with the diffusivity is a result of both the polymer expansion and the lowering of the glass transition temperature (Tg) at the reacted sites.

Based on this model, the role of physical mechanisms in profiles shapes of silylated resists were investigated in collaboration with Marco Zuniga. The effects of diffusion, reaction and stress parameters on the profiles shapes are summarized in the following section.

3.1.1. Silylation Mechanism Simulation Results

The profile of expanded sites in the resist can be calculated as a function of polymer characteristics, processing and imaging conditions. The initial condition for the bonding sites H at t=0 are provided by the change of state after exposure. It is assumed that H is proportional to the energy deposited in the resist and can be calculated with simulators such as TEMPEST[68]. The conditions simulated were NA = 0.5, λ = 248nm, sigma =0.5 and no defocus. The refractive index was chosen as to deposit the energy within 0.1μm of the

top surface of the film. Normalized values for bonding sites concentration, and hence sily-

lating agent, unexpanded site, and expanded site concentration were utilized in the simu-

lations.

Figure 3-2 illustrates the typical mesh deformation due to the volume mismatch
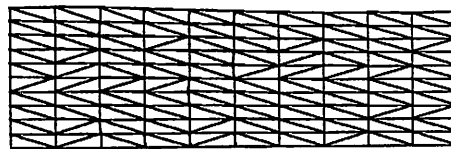
silylation time = 10s
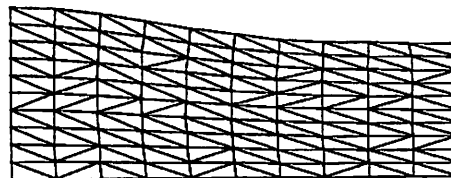
silylation time = 50s
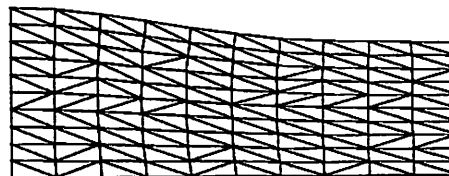
silylation time = 100s

Figure 3-2. Example mesh deformation for a 0.3μm feature

(top) 10 seconds, (middle) 50 seconds and (bottom) 100 seconds.

introduced by the silylating agent. The amount of deformation introduced does not ill-con-

dition the Jacobian transformation of the subparametric triangulation scheme, allowing the

initial discretization to be employed throughout the simulation. As previously mentioned, the deformation rate is proportional to the rate of change of expanded sites. Thus, the deformation as a function of time is proportional to the unexpanded site concentration, and eventually ceases as the reaction reaches completion. The deformation of the example depicted in Figure 3-2 stops after approximately 90s of silylation time.

Figure 3-3 depicts the results for coupling-free diffusion limited and reaction limited examples for a 0.3μm feature. In all subsequent simulations, the chamber pressure and silylating agent surface desorption values were set to achieve a maximum concentration of 0.5 at the surface of the film within 10 seconds in the absence of any reaction in the film. The expanded site concentration for the diffusion limited case in Figure 3-3a was obtained with the following parameters: D_o= 1e-5μm^2/s, K_1 = 5/s and t_{relax} = 1s. The bright areas of the aerial image lead to high concentrations of hydroxil groups, which in turn locally deplete the silylating agent concentration. Thus, the silylating agent is consumed faster in the middle of the feature, allowing diffusive transport to achieve higher concentration values in the darker regions of the film. This leads to the creation of a "W" expanded site profile within the film. The local species time evolution for the surface node with the highest hydroxil group concentration is depicted in Figure 2c. The relaxation profile is clearly depicted in the time evolution of unexpanded sites, which is controlled by the ratio of the reaction rate to the relaxation time.

The expanded site concentration for the reaction limited case depicted in Figure 3-3b was simulated with the following parameters: D_o= 1e-3μm^2/s, K_1 = 1e-2/s and t_{relax} = 1s. Both the high diffusivity and low reaction rate allow the silylating agent to rapidly pen-
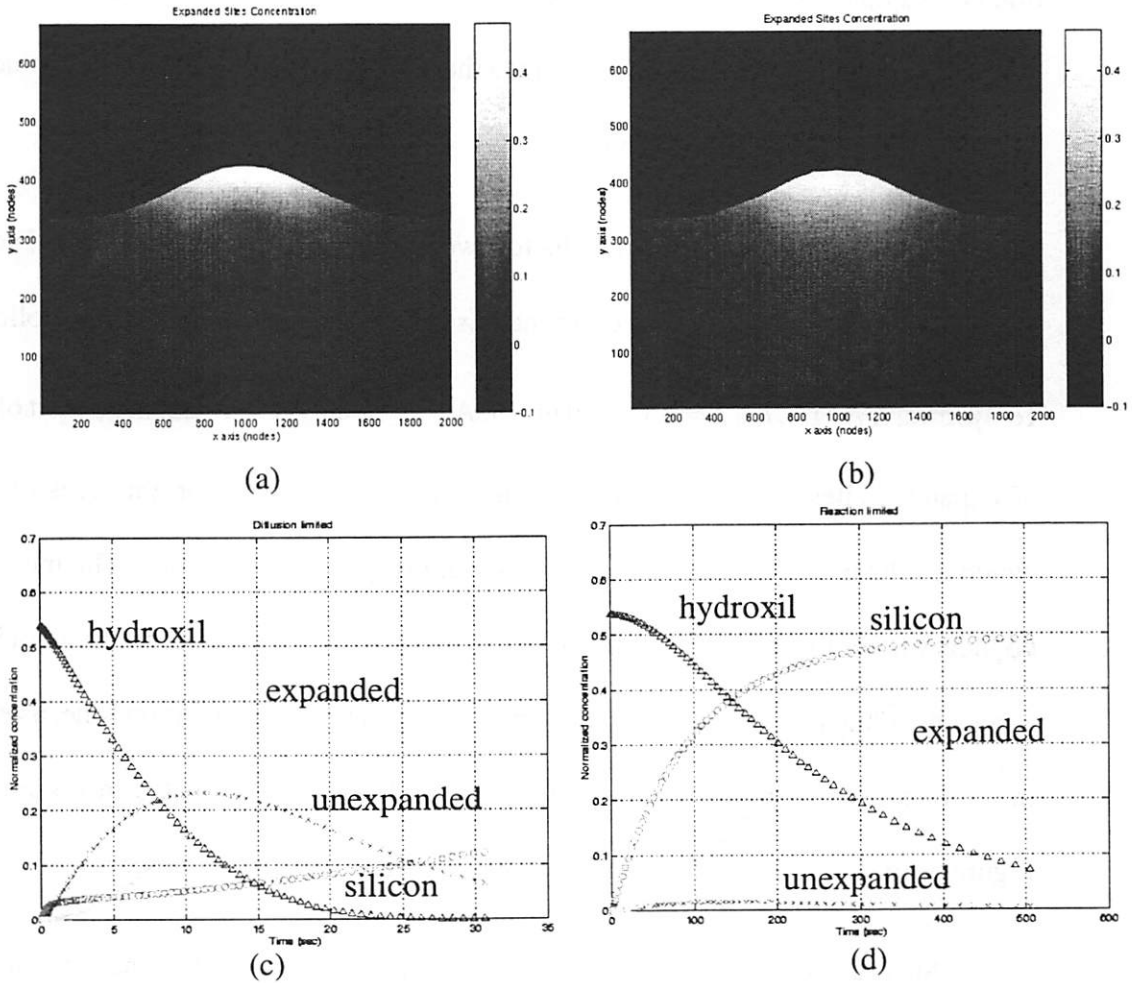
(a)

(b)

(c)

(d)

Species time evolution for node(0,0) for coupling-free diffusion limited silylation process.

Species time evolution for node(0,0) for coupling-free reaction limited silylation process.

Figure 3-3. Diffusion limited and reaction limited silylation

(a) Expanded Site concentration contours for 0.3μm feature for a coupling-free diffusion limited silylation process. Silylation time = 30s (b) Expanded Site concentration contours for 0.3μm feature for a coupling-free reaction limited silylation process. Silylation time = 500s

etrate the film beyond the optical exposure depth. In this case, the profile formation closely

follows the intensity contours of the initial aerial image. Thus, the characteristic "W" pro-

file obtained for the diffusion limited case is not present in the reaction limited example.

In addition, the time evolution for the unexpanded sites is very different from the diffusion limited example. Due to the lower ratio of reaction rate to relaxation time, the unexpanded sites concentration is five times lower since the reaction cannot replenish the values before they relax away into expanded sites.

Figure 3-4 illustrates the results for two nonlinear diffusion examples. The simulation parameters used to obtain the expanded site contours in Figure 3a as are follows: $D_o =$ 1e-4μm^2/s, $K_1 = 1$/s, $t_{relax} = 0.1$s, and $\omega = 5$. As previously discussed, the extent of reaction of expanded sites greatly increases the local diffusivity in the bright areas of the film, which results in a sharp boundary in the silylating agent concentration. The motion of this boundary is controlled by the intrinsic diffusivity and the local concentration gradient, creating a near linear dependence of silylating agent uptake with silylation time, as evidenced in the linear increase of expanded sites with silylation time depicted in Figure 3-4c and Figure 3-4d. Such behavior is characteristic of a case II diffusion process.

Such a nonlinearity eliminates the "W" profile observed in the diffusion limited example, since the rapid fluxes established in the bright areas of the film allow for local replenishment of the silylating agent consumed in the reaction. As expected, such behavior is more pronounced with increasing diffusion coupling values. Figure 3-4b depicts the expanded sites concentration for $D_o =$ 1e-4μm^2/s, $K_1 = 1$/s, $t_{relax} = 0.1$s, and $\omega = 20$. The increased coupling value gives rise to an even sharper silylating agent front, whose gradients is the highest in the bright areas of the film. The net effect is to increase the silylation depth as evidenced by the deeper contours of expanded sites in the bright areas of the image. Note that the nonlinearity is also evident in the time evolution of the species as
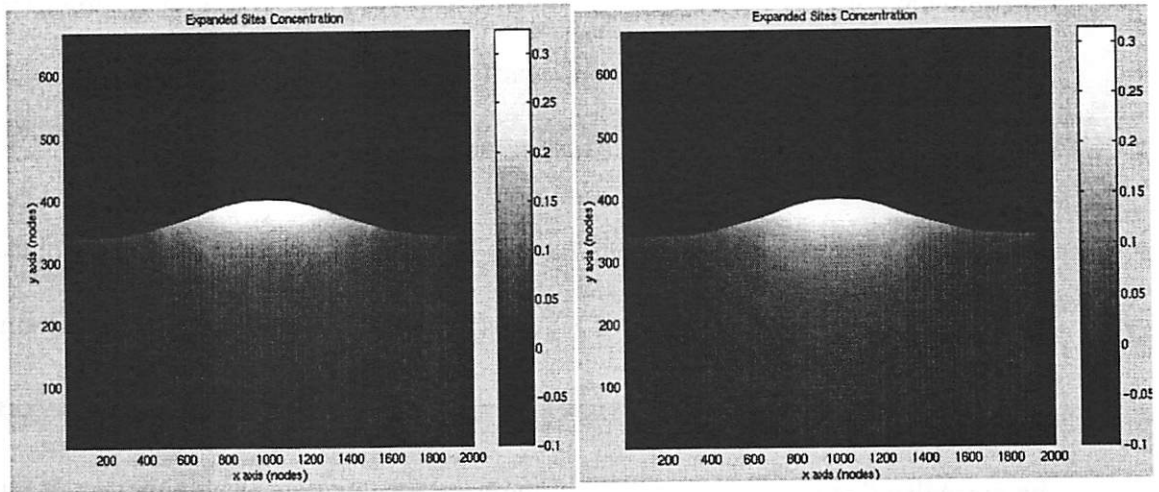
(a)

(b)
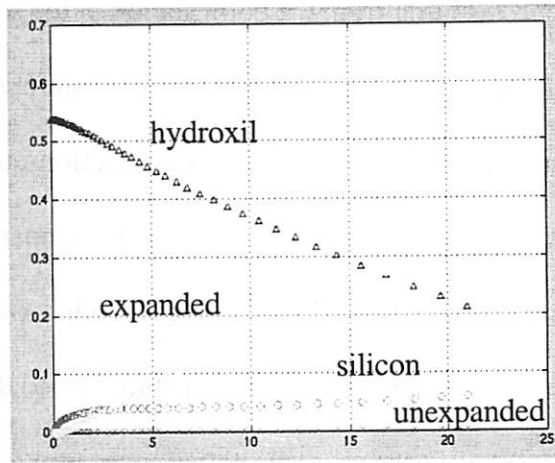
(c)
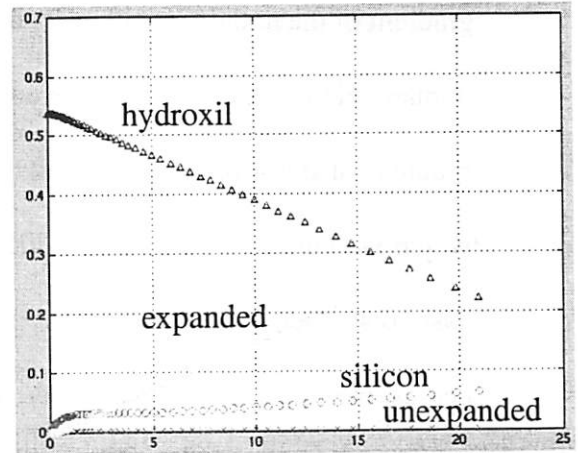
(d)

Species time evolution for node(0,0) for a non stress-coupling nonlinear diffusion silylation process. Silylation time = 25s, ω=5

Species time evolution for node(0,0) for a non stress-coupling nonlinear diffusion silylation process. Silylation time = 25s, ω=20

Figure 3-4. Diffusion limited and reaction limited silylation

(a) Expanded Site concentration contours for 0.3μm feature for a non stress-coupling non-linear diffusion silylation process. Silylation time = 25s, ω=5. (b) Expanded Site concentration contours for 0.3μm feature for or a non stress-coupling nonlinear diffusion silylation process. Silylation time = 25s, ω=20

depicted in Figure 3-4c and Figure 3-4d. Both Figures depict a near-linear decay in the local hydroxil group concentration, in sharp contrast with the exponential decays depicted in the coupling-free examples. Finally a lower relaxation value was utilized to more clearly

illustrate the effect of the diffusion nonlinearity. If the relaxation time is excessively long compared to the reaction rate, the nonlinearity has little effect as the profile formation will be initially by the initial Fickean diffusion mechanism.

Figure 3-5 depicts the results for two Fickean diffusion, stress-coupling examples. The expanded sites concentration of Figure 4a was obtained with the following simulation parameters: D_o= 1e-3μm^2/s, K_1 = 1/s, t_{relax} = 1s, ω = 0, and B = 1. As previously discussed, the normalized stress fields throughout the film are calculated as a function of the spatial gradient of the nodal velocity distribution resulting from the deformation of the simulation domain. Hence, the stress values are the highest in the periphery of the feature where the gradient of deformation is the highest. This results in a rapid local reaction quenching, which is manifest by the larger sidewall angle depicted in Figure 3-5 as compared to the cases discussed earlier. This phenomena is similar to bird's beak formation in LOCOS processes, in which the surface oxidation rate is exponentially quenched by the local stress in the field. This increase in the sidewall stress is further evidenced in Figure 3-5b, which was obtained with the following simulation parameters: D_o= 1e-4μm^2/s, K_1 = 1/s, t_{relax} = 1s, ω = 0, and B = 1. As evidenced in the local species time evolution (faster hydroxil group depletion and expanded site generation), the lower intrinsic diffusivity with the same reaction rate allows for a greater proportion of silylating agent to participate in the reaction before it is swept away through diffusive transport. This effective rise in the local reaction rate with decreasing diffusivity is due to the non-equilibrium condition simulated for the silylating agent uptake at the top surface of the film. As shown in Figure 3-5c and Figure 3-5d, the silylating agent concentration at the top surface is well below its equilibrium value

of 0.5, hence and increase in the diffusive flux locally depletes the silylating agent concentration.

This results in a greater unexpanded site concentration, greater local deformation, higher stress values, and hence an increased sidewall angle. On the other hand, the higher diffusivity depicted in Figure 3-5a penetrates the film more rapidly and allows for a more uniform reaction in the film, lower local stress fields, and hence, lessened reaction quenching. The maximum expanded site value achieved with the higher diffusion value is 0.23, compared to 0.41 for the latter example.

Figure 3-6 illustrates the expanded sites concentration obtained from two diffusion and stress coupled examples of the silylation model. The simulation depicted in Figure 3-6a was carried out with the following parameters: D_o= 5e-5μm^2/s, K_I = 0.5/s, t_{relax} = 1s, ω = 5, and B = 0.8.

As expected, the nonlinearity modeled both increase the sidewall angle and create a more uniform and abrupt boundary between silylated and unsilylated sites in the bright areas of the image. Moreover, although the reaction rate is half the value of the previous example, the concentration of expanded sites is higher in the bright regions of the image. The higher net reaction rate is due to the lower silylating agent diffusivity coupled with the diffusion nonlinearity, increasing the local concentration available for the silylation process. These effects are further illustrated in Figure 3-6b, which was simulated with the following parameters: D_o= 5e-5μm^2/s, K_I = 0.5s, t_{relax} = 1s, ω = 10, and B = 1.2. Both the higher stress and diffusion coupling coefficients quench the deformation process more rapidly. The net lower reaction rate due to locally higher diffusive distribution of the silylating

(a)

(b)

(c)

Species time evolution for node(0,0)
for a stress-coupling linear diffusion
silylation process.
Silylation time = 25s, D_0=1e-3μm^2/s
B=1

(d)

Species time evolution for node(0,0)
for a stress-coupling linear diffusion
silylation process.
Silylation time = 25s, D_0=1e-4μm^2/s
B=1
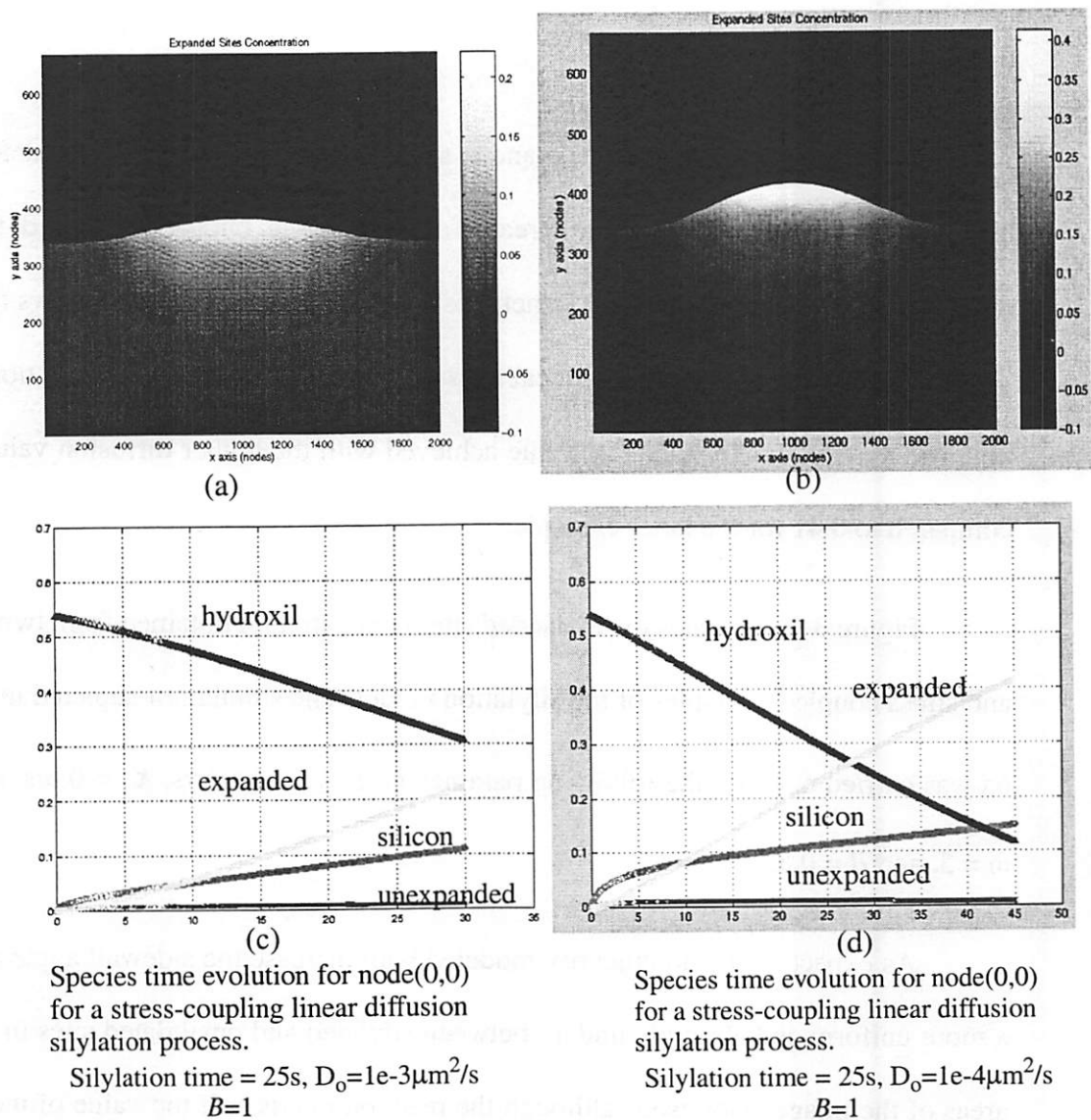
Figure 3-5. Stress coupling linear diffusion

(a) Expanded Site concentration contours for 0.3μm feature for a stress-coupling linear diffusion silylation process Silylation time = 25s, D_0=1e-3μm^2/s, B=1. (b) Expanded Site concentration contours for 0.3μm feature for a stress-coupling linear diffusion silylation process Silylation time = 25s, D_0=1e-4μm^2/s, B=1.

agent leads to less pronounced initial spatial gradient in the nodal velocity distribution. The

higher stress coupling value subsequently quenches the effective reaction rate, resulting in

less surface deformation.
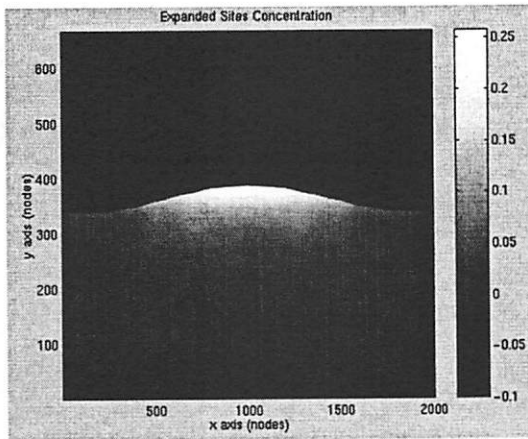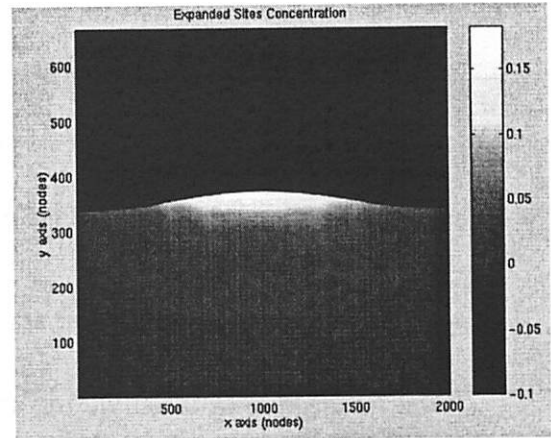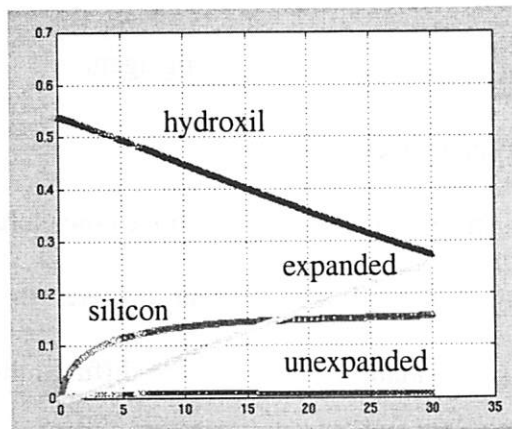
50

(a)

(b)

(c)

(d)

Species time evolution for node(0,0) for a stress-coupling linear diffusion silylation process.
Silylation time = 25s, $\omega=5, B=0.8$.
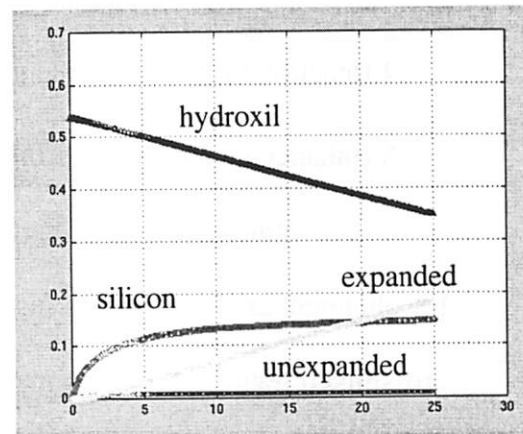
Species time evolution for node(0,0) for a stress-coupling linear diffusion silylation process.
Silylation time = 25s, $\omega=10, B=1.2$.

Figure 3-6. Stress Coupling linear diffusion

a) Expanded Site concentration contours for 0.3μm feature for a stress-coupling linear diffusion silylation process. Silylation time = 25s, $\omega=5, B=0.8$. (b) Expanded Site concentration contours for 0.3μm feature for a stress-coupling linear diffusion silylation process Silylation time = 25s, $\omega=10, B=1.2$.

3.2. General Model for Positive and Negative Tone Silylation

This section describes a general moving boundary model for positive and negative tone silylation process capable of simulating both diffusion enhanced and non-diffusion enhanced silylating schemes. This model takes into account the following:

1. Diffusion of the silylating agent in non-crosslinked region

2. Adsorption of the silylating agent at functional group sites

3. Polymer expansion during adsorption of silylating agent (polymer relaxation)

4. Reaction of the functional groups with the adsorbed silylating agent

5. Enhancement of local diffusivity at the reacted sites

An intuitive picture of the mechanisms that motivated the above considerations can be obtained as follows. During silylation, the silylating agent diffuses in the non-crosslinked region of the polymer (diffusion enhanced silylation) or diffuses through the entire polymer (non-diffusion enhanced silylation). Since the silylating agent molecules are larger than the functional group sites, the silylating agent must be adsorbed at the functional group sites before reaction can take place. This adsorption process can be visualized by assuming that the larger silylating agent molecule must penetrate into the smaller functional group sites in order to make itself available for reaction. As a first pass, the absorption process is modeled by the absorbing probability equation where it is assumed that the probability that a silylating agent will be adsorbed is proportional to the silylating agent flux. During the adsorption, the polymer is displaced by the larger silicon molecule, causing it to swell at the site. It is assumed that the polymer adsorption/swelling rate is proportional to the polymer relaxation time (t_r). After adsorption, the silylating agent reacts with

the functional groups to form the reacted sites. Since the silylated resist has lower glass transition temperature (T_g)[66], the diffusivity of the silylating agent at the reacted sites is much larger than that of the unsilylated sites. This mechanism creates a sharp moving boundary between silylated and unsilylated resist.

3.2.1. Adsorption rate model

From the above consideration, one can write the following model for the adsorption rate probability:

Equation 3-9.
$$k_{ads} = \left(1 - \exp\left(-\alpha\frac{S}{t_r}\right)\right)$$

In words, the probability that a silylating agent will be adsorbed at a functional group site is proportional to the silylating agent concentration and inversely proportional to the polymer relaxation time. The higher the silylating agent concentration or the lower the relaxation time, the higher the probability of an adsorption event. Thus, the reaction rate will be proportional to the silylating agent concentration, the functional group concentration and the probability that the silylating agent will be adsorbed at the functional group sites.

3.2.2. Diffusivity model

As explained above, the local diffusivity is enhanced at the reacted sites due to the lower T_g of the polymer at these sites[66]. Since there are several silylation processes [100][70][71], a general model should account for all these processes. The Fujita-Doolittle equation for diffusion is more appealing for reacted sites enhanced diffusion since it is theoretically derived from free volume and glass transition temperature arguments[46]. To

present a general diffusion model, the Fujita-Doolittle equation is adapted to take into account cross-linked regions that impede the diffusion of the silylating agent.

Equation 3-10. $$D = D_0 \exp\left(\frac{\omega R}{1 + \upsilon R} - \gamma C\right)$$

D_o is the intrinsic diffusivity of silylating agent in the resist polymer, R is the reacted sites concentration and C is the cross-linked sites concentration.

3.2.3. Polymer relaxation

As discussed above, the silylation process consists of two complex moving boundary problems; one in which the silylated/unsilylated boundary advances inside the resist material and another in which resist continuously swell during the process of silylating agent adsorption (i.e., no conservation of volume). It is assumed that the volume expansion rate is proportional to the change in the reacted sites concentration. This assumption yields:

Equation 3-11. $$\frac{\partial}{\partial t} Vol = \beta \frac{\partial R}{\partial t}$$

β is a parameter proportional to the size of the silylating agents molecules being adsorbed in the resist.

3.2.4. Silylation diffusion/reaction kinetics

The following chemical equations summarizes the reaction kinetics described above:

$$S + H \xrightarrow{k_{ads}} S\text{:}H$$

$$S\text{:}H \xrightarrow{k_r} R$$

Equation 3-12.

where S:H is an adsorbed site available for reaction.

3.2.5. Differential Equations

The following set of coupled nonlinear partial differential equations describe the proposed silylation model:

$$\frac{\partial S}{\partial t} = -k_{ads}k_r SH + \nabla(D\nabla S)$$

$$\frac{\partial H}{\partial t} = -k_{ads}k_r SH$$

$$\frac{\partial R}{\partial t} = k_{ads}k_r SH$$

$$\frac{\partial}{\partial t}Vol = \beta k_{ads}k_r SH$$

$$D = D_0 \exp\left(\frac{\omega R}{1+R} - \gamma C\right)$$

$$k_{ads} = \left(1 - \exp\left(-\alpha\frac{S}{t_r}\right)\right)$$

$$k_r = A\exp\left[-\frac{(Ea_1 - B\sigma)}{KT}\right]$$

Equation 3-13.

3.2.6. Boundary conditions

The gas-polymer interface can be described by assuming that the flux of the silylating agent is driven by the gas pressure in the reactor and by the concentration of the silylating agent in the polymer near the gas-polymer interface[67]. The model is as

Equation 3-14.
$$-D\left(\frac{\partial S}{\partial n}\right)_{\text{int air-polymer}} = k_1 P_a - k_2 S$$

55

Assuming impermeable boundary conditions at the substrate polymer interface gives

Equation 3-15. $$-D\left(\frac{\partial S}{\partial n}\right)_{\text{int substrate-polymer}} = 0$$

3.3. Modeling O_2 Reactive Ion Etching for Surface Imaged Resists

3.3.1. Introduction

Surface imaged resist processes require O_2 reactive ion etching (RIE) dry development step to transfer the resist image defined at the near top region to the rest of the resist. In the top surface imaging (TSI), the near top region of the resist to be etched contains silicon, which converts to silicon dioxide etch mask during the dry development step. The modeling of this O_2 RIE process is necessary for the simulation of surface imaged resist processes. The difference between etching surface imaged resist processes and conventional RIE processes is that the etch mask is not prescribed before the etching process. It must be created during the etching process proper. Thus, modeling of the O_2 RIE process necessitate the modeling of SiO_2 etch mask formation during the etching.

Figure 3-7 illustrates the dry etching process for surface imaged resists. The feed gas is assumed to be SO_2. The oxygen atoms react with the silicon to form a SiO_2 barrier. The presence of sulfur results in inhibition of reaction on the resist surface and protects the sidewalls. The resist surface is bombarded with energetic ions and surface that is not protected by barrier gets etched away. The incident energetic ions remove the sulfur, increasing the etch rate of bombarded surfaces.
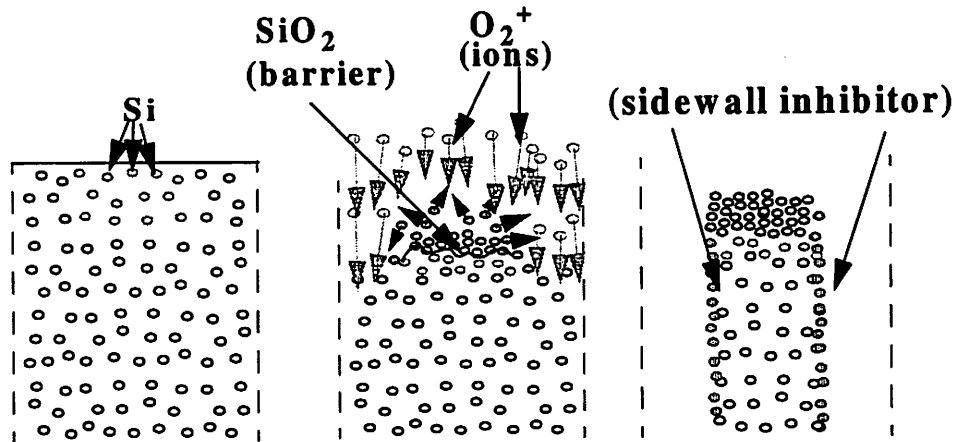
Figure 3-7. Schematic of dry etch process for surfaced imaged resist processes

A considerable number of plasma processing models and simulators have been developed[73][74][75][76][77][78][79]. The available simulation models attempt to capture the material removal by emulating the time evolution of the topography during the etching process. The most popular algorithm used for topographic profile simulation is the *string algorithm*, well known from the simulation program SAMPLE[2]. In this algorithm, the wafer surface is represented by a string of points connected by line segments (2D) or surface elements (3D). Depending on the implementation, the lines are moved according to the local etch rate[76].

A second algorithm for dry etch simulation is the *cell-removal method* proposed by Pelka[76]. In this approach, the complete volume of the material to be etched is described by dividing it into a matrix of little cells. These cells are removed according to the local etch conditions. Sethian proposed etching algorithm using Level Set Methods[80]. The

approaches described above simulate the time evolution of the topography in order to be able to visualize the final topography after etching.

An alternative approach used in STORM is to represent the simulation domain with a grid of nodes and elements using the finite element method. The material to be etched is given some initial concentration and the time evolution of the remaining material topography is predicted by the reaction/diffusion/ion-bombardment kinetics on a fixed grid. The etched profile can then be visualized with a plotter such as MATLAB, by plotting the concentration of the remaining material. By using interpolation schemes to refining the grid, the plotter displays a sharp contrast between etched and non-etched material and leads to a more realistic profile after simulation. In this way, visualization of the final profile is left as a task of a plotter and not the grid. Most importantly, line edge roughness as observed in etched profiles of surface imaged resists can be simulated more efficiently with this approach.

3.3.2. O_2 RIE plasma etching model for surfaced imaged resists

This section demonstrate the new approach by modeling the O_2 RIE dry development process of surface imaged resists, although the approach is applicable to all plasma etching processes. Consider the following mechanisms during the O_2 RIE dry development step:

1. Transport of oxygen (O) from the bulk plasma to resist (C) surface

2. Reaction of silicon (S) and O to form SiO_x etch barrier (B)

3. Adsorption of O by C surface to form $C{:}O$ adsorbed products

4. Reaction and thermal desorption of $C{:}O$ to form volatile products (P)

5. Ion enhanced desorption of $C{:}O$ products

6. Physical sputtering of S

7. Physical sputtering of B

8. Enhancement of local diffusivity of oxygen at etched sites

The following describes the above mechanism. During the dry development step, O atoms (activated neutrals) diffuse to the resist surface to react with the carbon (C) and silicon (S) while energetic ions (I) bombard the exposed surface. The reaction of the O with S result in a SiO_x etch barrier (B). The adsorption of O by C surface and subsequent reaction results in isotropic etching (ashing) of the resist. The ion enhances the etching rate at the surface by increasing the desorption rate of the etched products. The rate-limiting step is assumed to be desorption of CO gas[81]. Energetic ions can also sputter the silicon before it forms a barrier or can sputter the barrier. The absence of resist material after etching means the fresh O atoms can be quickly transported to the new exposed surface. This is considered as an enhancement of the local diffusivity at the etched sites.

The chemistry and physics of a plasma process is very complex, making the evaluation of all possible surface processes computationally expensive. Additional chemistry and physics can be incorporated into the above etch model, including the consideration of SO_2 feed gas (instead of O_2 feed gas) to allow for sidewall passivation by the sulfur products, physical sputtering of carbon, formation and desorption of CO_2 as an etch product, etc. These processes can be added to the above model with ease but at the cost of increased computation resources and time.

3.3.3. Monte-Carlo method for Ion bombardment

It is assumed that the energy and angle of incident of the ions arriving at the resist surface have a normal distribution about some mean value with standard deviation σ. For the energy, the mean is chosen to be proportional to the substrate bias. The mean incidence angle is chosen to be zero (normal to the surface) with $\sigma \approx 2°$ [76]. In order to distinguish different angles of incidence and different energies, Monte-Carlo methods are used. A random number generator determines the energy and angle of a incident ion. The effects of the ion on etching are then incorporated into the calculation of the state of the resist surface.

3.3.4. Dry development diffusion/reaction kinetics

The following chemical equations summarizes the reaction kinetics described above:

$$O + S \xrightarrow{k_{ox}} B$$

$$O + C \xrightarrow{k_{ads}} O{:}C \xrightarrow{k_{th}} P$$

$$I + O{:}C \xrightarrow{Y_{CO}k_{ion}} P$$

$$I + S \xrightarrow{Y_S k_{ion}}$$
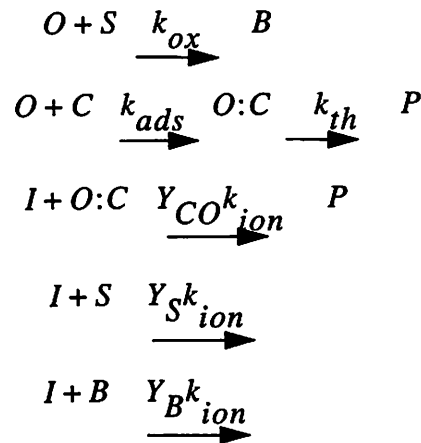
Equation 3-16.
$$I + B \xrightarrow{Y_B k_{ion}}$$

where k_{ox} is the oxidation rate constant, k_{ads} is the adsorption rate constant, k_{ther} is the thermal desorption rate constant, Y_{CO}, Y_S and Y_B are the yield of CO, S and B molecules desorped or sputtered per ion incident, and k_{ion} is proportional to the ion bombardment energy.

3.3.5. Diffusivity model

It is assumed that the plasma is generated at a high enough pressure such that the transport of the activated neutrals is governed by diffusion. As explained above, the local diffusivity is enhanced at the etched sites due to the absence of resist polymer at these sites (free space). It is assumed an exponential dependence of the diffusivity on the etched sites concentration.

Equation 3-17.
$$D = D_0 \exp\left(\frac{\omega P}{1 + \upsilon P}\right)$$

D_o is the intrinsic diffusivity of neutrals in the resist polymer and P is the reacted product (free space) concentration.

3.3.6. Differential Equations

It is assumed that all O atoms incident on the surface react immediately to form $C{:}O$. i.e. Adsorption probability $k_{ads}=1$. It is further assumed that the desorption rate is much larger than the adsorption rate so that one needs not keep track of $O{:}C$ concentration.

The following set of coupled nonlinear partial differential equations describe the proposed dry development model:

$$\frac{\partial O}{\partial t} = -k_{ox}OS - k_{th}OC + \nabla(D\nabla O)$$

$$\frac{\partial S}{\partial t} = -k_{ox}OS - Y_S k_{ion}IS$$

$$\frac{\partial B}{\partial t} = k_{ox}OS - Y_B k_{ion}IB$$

$$\frac{\partial C}{\partial t} = -k_{th}OC - Y_C k_{ion}IOC$$

$$\frac{\partial P}{\partial t} = k_{th}OC + Y_C k_{ion}IOC$$

$$D = D_0 \exp\left(\frac{\omega_P}{1 + U_P}\right)$$

Equation 3-18.

3.3.7. Boundary conditions

The gas-polymer interface can be described by assuming that the flux of the oxygen atoms is driven by the gas pressure in the reactor and by the concentration of the oxygen in the polymer near the gas-polymer interface. The adsorption is assumed to be small at the barrier sites. This is modeled as

Equation 3-19. $-D\left(\dfrac{\partial O}{\partial n}\right)_{\text{int air-polymer}} = k_1 \exp(-\alpha B)P_a - k_2 O$

Assuming impermeable boundary conditions at the substrate polymer interface gives

Equation 3-20. $-D\left(\dfrac{\partial O}{\partial n}\right)_{\text{int substrate-polymer}} = 0$

3.3.8. Simulation Examples

Figure 3-8 and Figure 3-9 show the simulation results for positive and negative tone silylation schemes, respectively. The left figure of Figure 3-8 shows the exposure simulation results and is supposed to represent the extent of crosslinking in the film after exposure. The simulation is run for the isolated space, isolated line and dense lines (only one line is shown for dense line) cases. In Figure 3-9, the top figure shows the exposure (left) and post exposure bake (middle) simulation results and is supposed to represent the concentration of functional group capable of reacting with silylating agent to produce the 0.15um silylated profile shown (right).

The dry development model simulation is by far the most challenging model for STORM. The complexity stem primarily from the nondeterministic Monte Carlo process of ion bombardment. The BDF2 algorithm described in Chapter 2 assumes that the PDE simulates a deterministic process and uses an extrapolation scheme based on previous history to predict the initial guess for the Newton iterations. Unfortunately due to the randomness of the ion bombardment, the BDF2 algorithm fails to make accurate predictions and therefore carefully takes very small timestep to reduce numerical errors. Therefore, for the dry development process, the adaptive timestep control feature has to be turned off. Fixed timesteps is used instead to prevent BDF2 from taking very small timesteps and therefore increasing the simulation time. Because of this performance degradation, simulation times for the dry development processes takes about 50 minutes to complete.

Figure 3-10 shows simulation results of the dry etching process for surface imaged resist. Figure 3-10a shows resist remaining after some intermediate time and Figure 3-10b shows the resist line after the dry etching step. Figure 3-10c shows the oxygen atoms con-

63

Isolated space
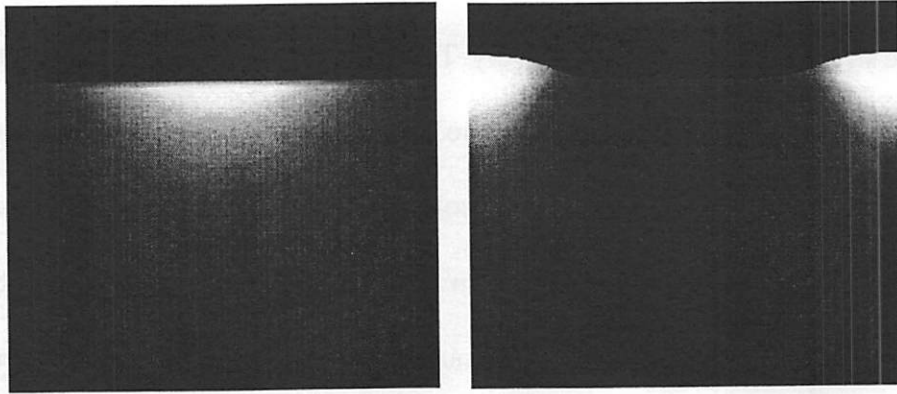
Isolated line
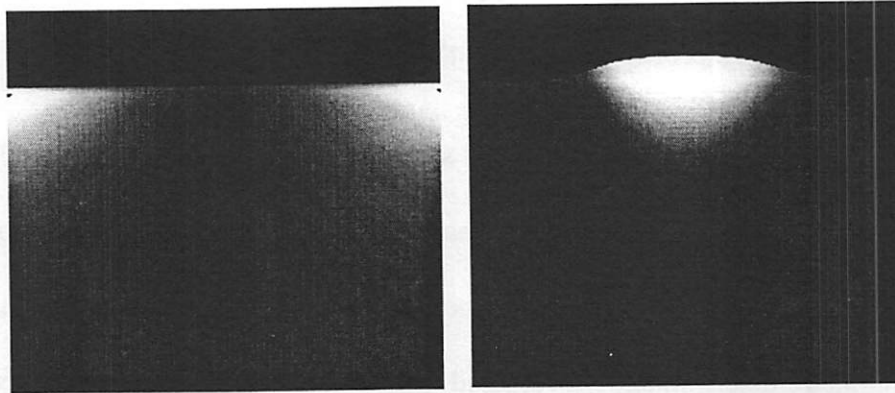
Dense lines
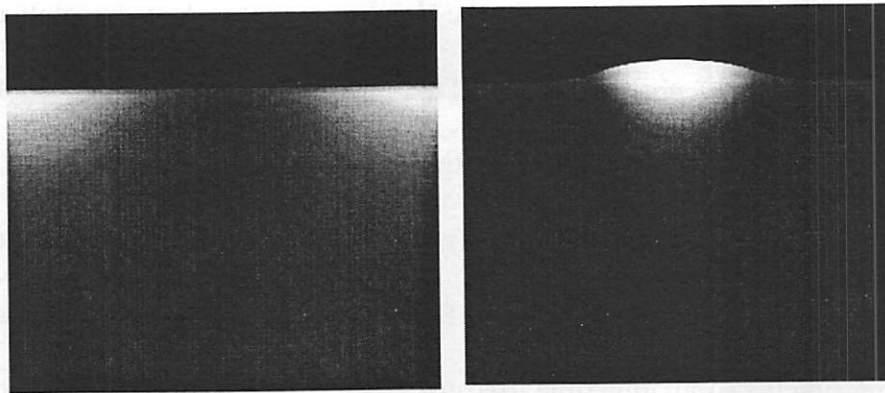
Figure 3-8. Positive tone silylation scheme

Simulation results for positive tone silylation scheme. The left figure shows the exposure
simulation results and is supposed to represent the extent of crosslinking in the film after
exposure. The simulation is run for the isolated space, isolated line and dense lines (only
one line is shown for dense line) cases.
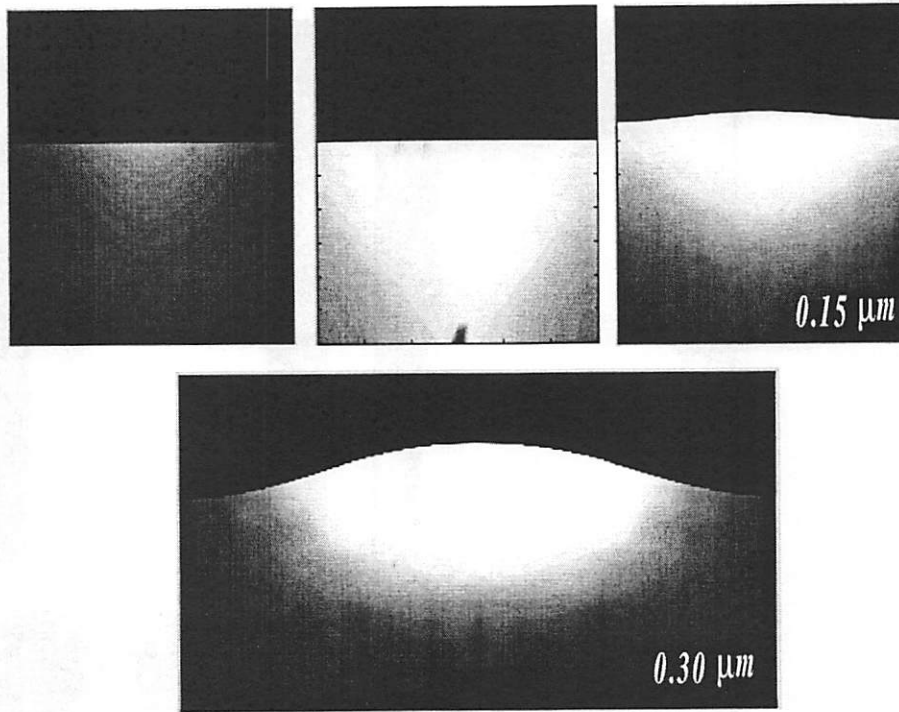
Figure 3-9. Negative tone silylation

Simulation results for negative tone silylation scheme. Top figure shows the exposure and post exposure bake simulation results and is supposed to represent the concentration of functional group capable of reacting with silylating agent.

centration and the resulting SiO_x barrier concentration protecting the unetched resist surface.

Figure 3-11 demonstrates the feasibility of STORM at simulating the 193nm TSI process. The case for the positive tone process is shown. Figure 3-11a shows the extent of crosslinking in the resist after exposure. Figure 3-11b shows the resist after silylation and Figure 3-11c shows the resist line after dry development.

Line edge roughness (LER) is the most important issue hampering the manufacturability of surface imaged resist processes. STORM is the first simulator known to offer

(a)

(b)

(c)

(d)
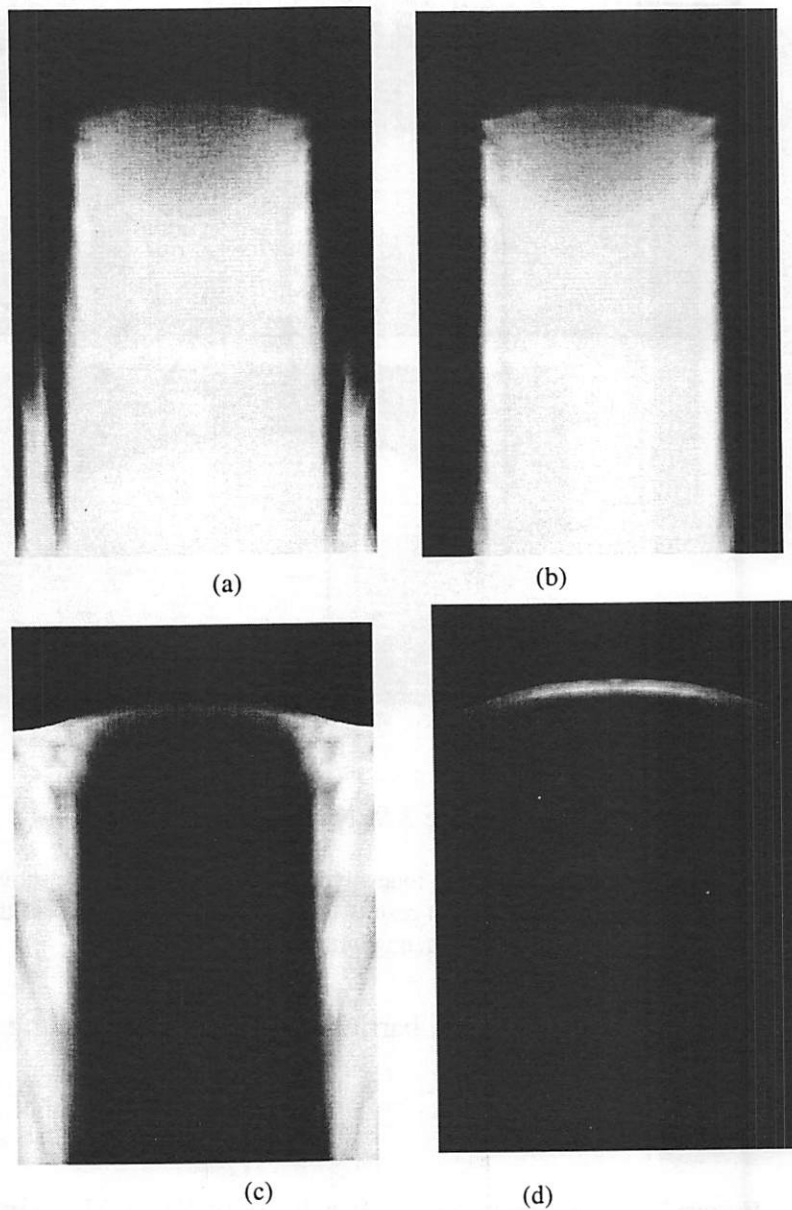
Figure 3-10. O$_2$ RIE dry development simulation

(a) etched profile after some intermediate time (b) final etch profile after dry development.
(c) oxygen atom concentration after dry development. (d) SiOx barrier concentration.

simulation of this important technology issue. Another technology issue of concern is line-end shortening (LES) effects in CAR. The relative impact of LES effect on smaller features
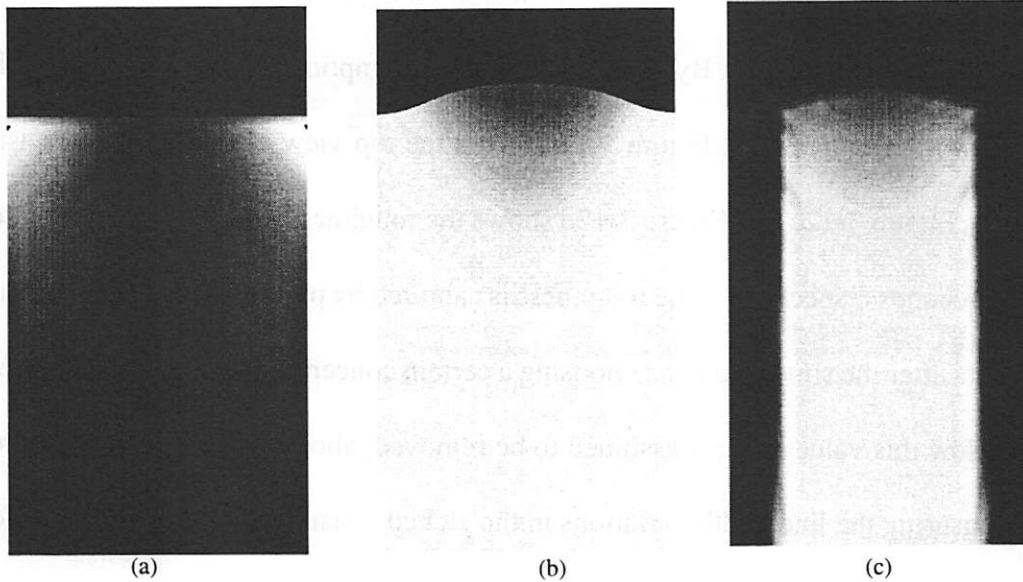
Figure 3-11. Top Surface Imaging Simulations

(a) extent of crosslinking after exposure. (b) silylated profile (red region shows silicon concentration) (c) resist feature after dry development

demands that causes of LES be investigated and controlled to allow extension of CAR for deep submicron resist applications. A cost effective way of investigating LES is through simulation and STORM provides the means of simulating LES. The reader interested in our work on LES should consult reference [82].

The current surface imaged models in STORM assumes that LER is caused by the random nature of the sputtering of the low concentration silicon at the profile edges instead of its conversion into a SiO_x barrier. In other words, when an ion bombards the silicon containing surface in the presence of activated neutrals, the ion bombardment can accelerate the conversion of the silicon to SiO_x or it can sputter the silicon. While silicon areas containing enough silicon content have a high probability of being converted to SiO_x barrier,

67

the silicon concentration at the edges of silylated profile is very sensitive to this randomness of either barrier conversion/silicon sputtering process caused by the random nature of the ion bombardment. By using the above assumptions, simulation results for LER is shown in Figure 3-12 . Figure 3-12a shows the top view of the silylated resist. Figure 3-12b, Figure 3-12c and Figure 3-12d shows the roughness after 10 seconds, 15 seconds and 20 seconds respectfully. The roughness is captured by plotting the resist concentration contours after the simulation and choosing a certain concentration value as the threshold value (below this value resist is assumed to be removed, above this value the resist remain) and measuring the line width variations in the etched resist to obtain roughness information.
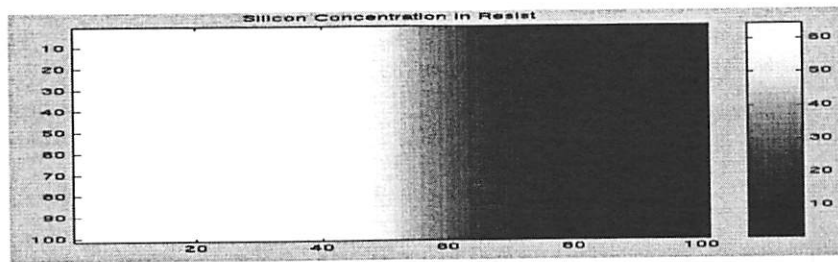
(a)
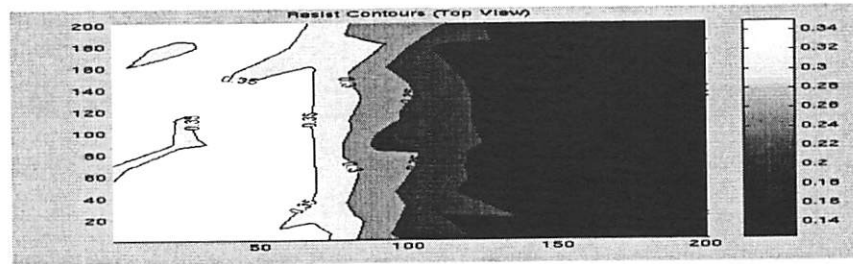
(b)
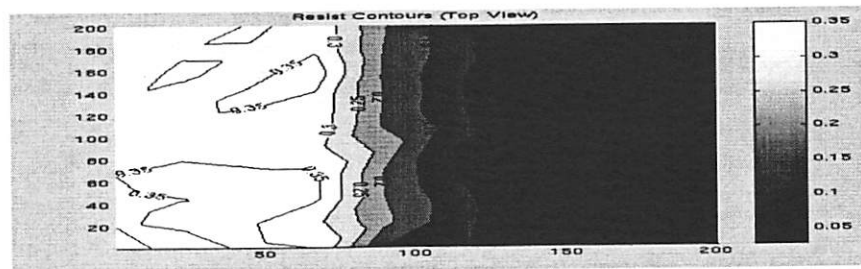
(c)
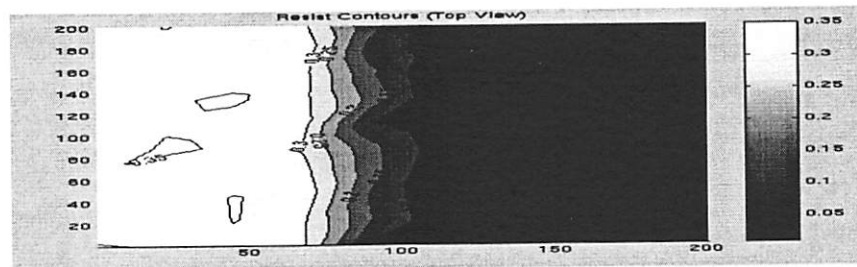
(d)

Figure 3-12. Line edge roughness in TSI process simulations

Top view simulation of etched profiles. (a) initial silicon concentration. (b) roughness simulation after 10 seconds (c) roughness simulation after 15 seconds (c) roughness after 20 seconds.

4 Numerical Algorithms

4.1. Introduction

Traditionally the numerical algorithms of choice for solving the PEB differential equations have been explicit time advancement algorithms such as the finite difference or Runge Kutta methods. In this algorithm, the domain is descretized on a spatial grid that defines the resist. The solution of the equation with time is obtained by discretizing in time. In the case of discretizing the acid, the finite difference algorithm requires that a second-order Taylor series approximation be used to represent the acid diffusion equation. An example of the simple case of Fickean diffusion on a two-dimension grid will be given. In this example the diffusion model becomes

Equation 4-1.
$$\frac{\partial H_i}{\partial t} = D_i \nabla^2 H_i$$

where H_i and D_i represents the local acid concentration and diffusivity at the ith node. The approximation for the second derivative in the x dimension is then given by[43]

Equation 4-2.
$$\frac{d^2 H_i}{dx^2} = \frac{H_i(j+1,k) - 2H_i(j,k) + H_i(j-1,k)}{(\Delta x)^2}$$

The finite difference implementation of this algorithm estimates the current concentrations based on the concentration from the previous time steps. Ferguson used fourth and fifth order Runge-Kutta methods employing variable time step schemes for the PEB simulation[31].

Current applications of STORM focus on a class of nonlinear moving boundary model-equations often encountered in modeling deep submicron resist processes. These model equations take on the form of partial differential equations (PDEs). An approach suitable for solving these model-equations is to develop a *semi-discrete* analogue of the PDEs where the PDEs are discretized in space using the Finite Element Method (FEM) [83]. This consists of a discretization of a domain of interest, into elements with discrete endpoints, or nodes. The space discretization results in a system of stiff ordinary differential equations (ODEs) with the system size proportional to the number of nodes approximating the domain. This system of ODEs can then be discretized in time to obtain a full discrete problem which can be solved numerically. The stiffness of the systems poses extra requirements on the stability of the methods to be used for the time discretization. For the sake of stability, an implicit time advancement scheme must be utilized to discretize the system in time and a resulting system of simultaneous implicit equations are solved at each timestep. This chapter describes the space and time discretization algorithms used to develop the STORM simulation engine.

4.2. Finite Element Space Discretization

The STORM simulator requires the user to provide a *semi-discrete* form of the PDEs using the finite element method. To illustrate the weak formulation procedure used for the discretization process, consider the following linear parabolic problem

Equation 4-3. $\dfrac{\partial}{\partial t}U(x,t) - \nabla\bullet(D\nabla U(x,t)) = f(U(x,t))$ in $\Omega \times I$

Equation 4-4. $U = 0$ on $\Gamma \times I$

Equation 4-5. $U(x,0) = U^0$

The weak formulation of Equation 4-3 reads as follows: Find

Equation 4-6. $U(t) \in H_0^1(\Omega), t \in I$

such that

Equation 4-7. $(\dot{U},V) + a(U,V) = (f(U),V)$ $\forall V \in H_0^1(\Omega), t \in I$

Equation 4-8. $U(0) = U^0$

where

Equation 4-9. $(\alpha, \beta) = \int_\Omega \alpha\beta d\Omega$ and $a(W, V) = \int_\Omega D\nabla W\nabla V d\Omega$

The space $H_0^1(\Omega)$ is a Hilbert space consisting of functions V defined on Ω which together with their first derivatives are square-integrable and are zero on the boundary, $\Gamma = \partial\Omega$. The reader interested in the definitions of Hilbert spaces should consult[83]. For the sake of discretization, let Ψ_h be a finite dimensional subspace of $H_0^1(\Omega)$ with basis

72

$\{\varphi_1, ..., \varphi_m\}$. Thus, one gets the following semi-discrete analogue of Equation 4-7: Find

$U_h(t) \in \Psi_h$, $t \in I$, such that

Equation 4-10. $\quad (\dot{U}_h, V) + a(U_h, V) = (f(U_h), V) \qquad \forall V \in \Psi_h, t \in I$

Equation 4-11. $\qquad (U_h(x, 0), V) = (U^0, V) \qquad \forall V \in \Psi_h$

Let us rewrite Equation 4-10 using the representation

Equation 4-12. $\qquad U_h(x, t) = \sum_{i=1}^{M} U_i(t)\varphi_i(x) \qquad t \in I$

Using Equation 4-12 and taking ,

Equation 4-13. $\qquad V = \sum_{j=1}^{m} v_j \varphi_j(x)$

in Equation 4-10, one gets

Equation 4-14. $\displaystyle\sum_{i=1}^{M} \dot{U}_i(t)(\varphi_i, \varphi_j) + \sum_{i=1}^{M} U_i(t)a(\varphi_i, \varphi_j) = (f, \varphi_j) \quad j = 1, ..., M, \quad t \in I$

Equation 4-15. $\qquad \displaystyle\sum_{i=1}^{M} U_i(0)(\varphi_i, \varphi_j) = \left(U^0, \varphi_j\right) \qquad j = 1, ..., M$

or in a matrix form:

Equation 4-16. $\qquad\qquad\qquad M \cdot \dot{U} + KU = F$

This can be written in the usual ODE system notation as:

Equation 4-17. $\qquad M \cdot \dot{U} = g(U) \qquad \text{where} \qquad g(U) = F - K \cdot U$

73

Equation 4-18. $$m_{ij} = (\varphi_i, \varphi_j) = \int_\Omega \varphi_i \varphi_j dx$$

Equation 4-19. $$k_{ij} = a(\varphi_i, \varphi_j) = \int_\Omega D\nabla\varphi_i \cdot \nabla\varphi_j dx$$

Equation 4-20. $$F_i = (f(t), \varphi_i)$$

K is known as the stiffness matrix, M is the time derivative matrix or the mass matrix and F is the forcing vector or the load vector. K and M are global matrices in the sense that they contain information about the whole domain Ω. In practice, the elements k_{ij} and m_{ij} are computed by summing the contributions from the different elements discretizing the domain. STORM uses triangular elements to discretize the domain.

4.3. The Implicit ODE Integrator

A variable time step second order implicit backward differentiation formula (BDF2) is used to solve the ODE system. The formula is of the following form:

Equation 4-21. $$U_{j+1} = aU_j + bU_{j-1} + ch\dot{U}_{j+1} + dh^3 \ddot{U}(\xi_j)$$

which holds for any smooth function $U(t)$, where ξ_j is some point in the interval (t_{j-1}, t_{j+1}) and where the coefficients a, b, ch and dh^3 are functions of the time steps. $h = h_{j+1} - h_j$ and $h_1 = h_j - h_{j-1}$ are chosen so that Equation 4-21 without the

final error term is exact for all polynomials $u(t)$ of degree two or less. The weight values a, b, and c are given by the following expressions:

$$a(h_1, h) = 1 - b$$

$$b(h_1, h) = -\frac{h^2}{h_1^2 + 2 \cdot h_1 \cdot h}$$

$$c(h_1, h) = h + h_1 \cdot b$$

Equation 4-22.

For example, equal timesteps, $h = h_1$, gives the following

Equation 4-23. $\qquad U_{j+1} = \frac{4}{3}U_j - \frac{1}{3}U_{j-1} + \frac{2}{3}h\dot{U}_{j+1} - \frac{2}{9}h^3\dddot{U}(\xi_j)$

Note that $\tilde{U} = aU_j + bU_{j-1}$ is just a linear extrapolation from the two previous values U_j and U_{j-1}. Thus substituting the BDF2 time advancement equation:

Equation 4-24. $\qquad \dot{U}_{j+1} = \frac{(U_{j+1} - \tilde{U})}{c(h_1, h)}$

into Equation 4-17, one gets the discrete form.

Equation 4-25. $\qquad M \cdot \frac{(U_{j+1} - \tilde{U})}{c} = g(U_{j+1})$

This implicit time advancement requires Newton iterations for its solution. The following is adapted from[84].

4.3.1. The Modified Newton Method for BDF2

Newton's method involves linearizing the residual function about the latest iterate

Equation 4-26. $\qquad R(U) \equiv M \cdot (U - \tilde{U}) - c \cdot g(U) = 0$

75

[85]. Thus, if $\overline{U}$ is the latest iterate, Newton seeks the next iterate $\overline{U} + \delta U$ from the approximation

Equation 4-27. $$R(\overline{U} + \delta U) \approx R(\overline{U}) + R'(\overline{U}) \cdot \delta U$$

where $R' \equiv J$ is the Jacobian matrix. Instead of updating J at each iteration, J is only updated when necessary (i.e. when convergence fails with an old J)[86]. So to get the Newton correction δU one solve the linear systems

Equation 4-28. $$J \cdot \delta U = -R(\overline{U})$$

Note that $J = M - c \cdot g'(\overline{U})$. J is a sparse matrix so an efficient sparse matrix linear solver is required to solve for δU. STORM uses SuperLU direct sparse matrix solver[87].

4.3.2. Predictor for the Initial Newton Guess

The predictor for the initial Newton guess for the Newton solution U_{j+1} is a quadratic extrapolation from the three previous steps U_j, U_{j-1}, U_{j-2}. The divided difference form of the Lagrange extrapolation error (predictor error)

$$PE = U[t_{j+1}, t_j, t_{j-1}, t_{j-2}] \cdot h \cdot (h + h_1) \cdot (h + h_1 + h_2)$$ is used to control the timestep, allowing accurate predictions of the system solution to ensure fast convergence of the Newton method. The predictor error requires knowledge of the converged solution which is not available. Thus, one makes the assumption that the predictor error of the current timestep is the same as the predictor error of the previous timestep. One then checks the validity of this assumption after the converged solution is obtained and accepts or rejects the timestep based on how close the assumed predictor error is to the actual predictor error. The time step control scheme is as follows:

1. Estimate the predictor error (PE_{est}) using the four previous timesteps

$$U_j, U_{j-1}, U_{j-2}, U_{j-3}$$

2. Calculate the timestep h such that PE_{est} is below some predictor error tolerance.

3. Use this h to calculate the initial Newton guess V.

4. Calculate the actual predictor error (PE_{act}) and compare with PE_{est}

5. If PE_{est} and PE_{act} are close enough, accept this timestep h. If not, half h and repeat steps (3), (4) and (5).

4.3.3. The Krylov Subspace Newton Convergence Accelerator

In order to improve the convergence characteristics, Miller's *Krylov subspace-accelerator* for the Newton's Method is employed. The following is a brief description from reference [88]. Consider the nonlinear equations $R(y) = 0$ of Equation 4-26. Multiplying by J^{-1} where $J = R(\hat{y})$ is an "old" Jacobian, we get the following Equation 4-29.

$$f(y) \equiv -J^{-1}R(y) = 0$$

The multiplication by J^{-1} in Equation 4-29 is achieved implicitly by solving directly or iteratively the linearized equations Equation 4-28. The Jacobian f' of f would be approximately equal to $-I$ near the desired root if the Jacobian had been freshly updated.

It is assumed, for the sake of devising an algorithm, that the following two assumptions hold. First because our predictor-error control strategy ensures that the initial guess

for our Newton's method will be very close to the desired root y, it is assumed that our f is exactly linear near y, or

Equation 4-30.
$$f(x + z) = f(x) - A \cdot z$$

for all x near the desired root y and all tiny corrections z. $-A$ is the constant (but unknown) nonsingular matrix $f'(y)$ at the root. Second, because A would be $\approx I$ if the Jacobian had been freshly updated as described in the preceding paragraph, it is assumed that

Equation 4-31.
$$Az \approx z$$

for any small correction vector z for which there is no better information.

Beginning with the initial Newton guess y_0, the accelerator first preconditions the residual equation with the Jacobian to get the initial residual.

Equation 4-32.
$$f(y_0) = -J^{-1} \cdot R(y_0) = r_0$$

Using Equation 4-30, it then solves the linear residual correction equation

Equation 4-33.
$$f(y_0 + v_1) \equiv r_0 - A \cdot v_1 = 0$$

to get the correction vector v_1, the next iterate $y_1 \equiv y_0 + v_1$ and $Av_1 \equiv f(y_0) - f(y_1)$. Thus at the start of the $(k+1)$st step, the set of vectors $\{v_1, v_2, ..., v_k\}$ and $\{Av_1, Av_2, ..., Av_k\}$ are accumulated. The general algorithm approximates the solution of the kth residual correction equation

Equation 4-34.
$$f(y_k + v) \equiv r_k - A \cdot v = 0$$

in two steps. First let w_{k+1} be the element in the subspace $V_k \equiv \text{span}\{v_1, v_2, ..., v_k\}$

such that $\|r_k - Aw_{k+1}\|_2$ is minimized. This involves solving a small $(k \times k)$ system of

normal equations

Equation 4-35.
$$\sum_{j=1}^{k} (Av_i, Av_i)\alpha_j = (r_k, Av_i)$$

for $i = 1, ..., k$. Thus, one solves the resulting linear least squares problem to obtain the

desired correction $w_{k+1} = \sum_{j=1}^{k} \alpha_j v_j$. The residual associated with w_k is

$q_{k+1} = r_k - Aw_{k+1}$. Second, a further correction z such that

Equation 4-36.
$$r_k - A(w_{k+1} + z) \equiv q_{k+1} - Az = 0$$

At this point, assumption in Equation 4-31 is used to obtain the correction $z = q_{k+1}$.

Thus the total correction v_{k+1} is given by

Equation 4-37.
$$v_{k+1} = w_{k+1} + q_{k+1}$$

and the next iterate is $y_{k+1} = y_k + v_{k+1}$.

Under the linearity hypothesis, Equation 4-30 and the additional assumption that A

is positive definite, it is proved in[76] that the $\text{span}\{v_1, ... v_k\}$ coincides with the Krylov

subspace $K_k(A; r_0)$ and that the new correction vector $v_{k+1} = w_{k+1} + q_{k+1}$ cannot

be in the previous span unless the residual q_{k+1} is already zero.

4.3.4. The Starting Procedure

The BDF2 algorithm as described above is a multi-step method requiring four solu-

tion vectors. Thus a starting procedure is needed to generate these solution vectors in order

to proceed with the BDF2 algorithm. The Crank-Nicelson time advancement scheme is

used followed by two steps of BDF2 with a fixed timestep. This gives the four solution vectors (3 + initial vector) needed to start the full BDF2 algorithm.

4.4. Polymer linear viscoelastic model

Resist materials are observed to behave viscoelastically below T_g and rubber-like above T_g[89]. The compaction or swelling of the polymer matrix during the relaxation of the polymer can induce mechanical stress in the resist film. If the polymer mechanical properties depend nonlinearly on the stress, the mechanics of the material is said to be nonlinear. A general linear viscoelastic model is used, assuming that the polymer deviatoric strain rate depends linearly on the deviatoric stress. The mechanical properties of the polymer is related to the stress through the following constitutive equations[49]:

$$\varepsilon = \varepsilon' + \varepsilon''$$

$$\dot{\varepsilon}'' = \frac{1}{3} trace[\dot{\varepsilon}]I$$

$$\frac{\partial}{\partial t}\sigma' + \frac{\sigma'}{\tau} = G\dot{\varepsilon}'$$

$$\sigma = \sigma' + \sigma''$$

$$\sigma'' = \frac{1}{3} trace[\sigma]I$$

$$\tau = \frac{\eta}{G}$$

v : deformation rate
$\dot{\varepsilon}'$: Deviatoric strain rate
$\dot{\varepsilon}''$: Volumetric strain rate
σ' : Deviatoric stress
σ'' : Hydrostatic pressure
η : Viscosity
G : Elastic shear modulus
K : Elastic bulk modulus
τ : relaxation time constant

Equation 4-38.

4.4.1. Discretization of the linear momentum balance equation

To simulate polymer deformation, forces at the boundary are related to the rate of change of the dependent variables that causes volume expansion or shrinkage in the polymer during the resist process. In the case of a fast reaction, it can be assumed that the volume displacement in the system is only a function of the rate of change of the expanding or shrinking species at the reacted/unreacted boundary, allowing us to neglect the bulk forces in the system[90].

This approximation is valid for the model equations under consideration, since these processes exhibit a sharp reacting front which propagates inside the resist material. Under this assumption, the product of the variational of the strain rate and the stress in the system is expressed as follows[49]:

Equation 4-39.
$$\int_{\Omega^e} (\delta\dot{\varepsilon} \cdot \sigma)d\Omega = \int_{\Omega^e} (\delta\dot{\varepsilon}' + \delta\dot{\varepsilon}'') \cdot (\sigma' + \sigma'')d\Omega$$

where the stress and strain rate vectors have been decomposed into orthogonal deviatoric and dialational components such that the product of deviatoric and dialational components is identically zero. The implementation details can be found in a book by Simo and Hughes[105].

4.5. Implementation Example

A numerical implementation of the reaction/diffusion equations in Chapter 2 is given in this section. The FEM discretization employs method of partial variable substitution to reduce the number of system variables. This improvement in the FEM implemen-

tation is proposed by Yuan *et al*[47]. It has the advantage of reducing the size of the global system by eliminating system variables by substitution. This reduces the memory requirements as well as speeds up the algorithm.

Consider the following model-equations which describes the reaction and diffusion mechanisms during post exposure bake.

$$\frac{\partial A}{\partial t} = k_r(1-A)H^m$$

$$\frac{\partial H}{\partial t} = \nabla(D\nabla H) - k_l H$$

$$D = D_0 \exp(\omega A)$$

Equation 4-40.

For the space discretization, it is assumed that

Equation 4-41. $$A = \sum_i A_i(t)\varphi_i \qquad H = \sum_i H_i(t)\varphi_i$$

Substituting Equation 4-41 into Equation 4-40 gives the weak form:

Equation 4-42. $$\int_\Omega \sum \dot{A}_i(t)\varphi_i\varphi_j d\Omega = \int_\Omega -k_r H^m \varphi_i d\Omega + \int_\Omega k_r H^m \sum A_i(t)\varphi_i\varphi_j d\Omega$$

$$\int_\Omega \sum \dot{H}_i(t)\varphi_i\varphi_j d\Omega = \int_\Omega \varphi_j \nabla\left(D\nabla \sum H_i(t)\varphi_i\right)d\Omega$$

$$-\int_\Omega k_l \left) \sum_i H_i(t)\varphi_i\varphi_j d\Omega\right.$$

Equation 4-43.

$$\sum \left(\int_\Omega \varphi_i \varphi_j d\Omega \right) \dot{H}_i(t) - \sum \left(\int_\Omega D\nabla\varphi_i \nabla\varphi_j d\Omega \right) H_i(t)$$

$$+ \sum \left(\int_\Omega k_l \varphi_i \varphi_j d\Omega \right) H_i(t) = \int_{\partial\Omega} \frac{D\varphi_j \partial\left(\sum H_i \varphi_i\right)}{\partial n} dl$$

Equation 4-44.

$$\sum \left(\int_\Omega \varphi_i \varphi_j d\Omega \right) \dot{A}_i(t) - \sum \left(\int_\Omega k_r H^m \varphi_i \varphi_j d\Omega \right) A_i(t) =$$

$$\sum \left(\int_\Omega k_r H^m \varphi_i d\Omega \right)$$

Equation 4-45.

Equation 4-46. $$m_{ij}^{(1)} \cdot \dot{A}_i(t) + k_{ij}^{(1)} A_i(t) = F_i^{(1)}$$

Equation 4-47. $$m_{ij}^{(2)} \cdot \dot{H}_i(t) + k_{ij}^{(2)} H_i(t) = F_i^{(2)}$$

Equation 4-48. $$m_{ij}^{(1)} = m_{ij}^{(2)} = \int_\Omega \varphi_i \varphi_j d\Omega$$

Equation 4-49. $$k_{ij}^{(1)} = \int_\Omega k_r H^m \varphi_i \varphi_j d\Omega$$

Equation 4-50. $$k_{ij}^{(2)} = \int_\Omega D\nabla\varphi_i \cdot \nabla\varphi_j d\Omega + \int_\Omega k_l \varphi_i \varphi_j d\Omega$$

Equation 4-51.
$$F_i^{(1)} = \int_\Omega k_r H^m \varphi_i d\Omega$$

Equation 4-52.
$$F_i^{(2)} = \int_{\partial\Omega} D\varphi_i \frac{\partial H_i}{\partial n} dl$$

Rewriting Equation 4-46 and Equation 4-47 in matrix form, one gets

Equation 4-53.
$$\begin{bmatrix} M & 0 \\ 0 & M \end{bmatrix}\begin{bmatrix} \dot{A} \\ \dot{H} \end{bmatrix} + \begin{bmatrix} K^{(1)} & 0 \\ 0 & K^{(2)} \end{bmatrix}\begin{bmatrix} A \\ H \end{bmatrix} = \begin{bmatrix} F^{(1)} \\ F^{(2)} \end{bmatrix}$$

This completes the space discretization.

For the time discretization, the BDF2 approximation (Equation 4-24)

$$\dot{U}_{j+1} = \frac{(U_{j+1} - \tilde{U})}{c(h_1, h)}$$

is substituted in Equation 4-53 which gives

Equation 4-54.
$$M\frac{A_{j+1} - \tilde{A}}{c} + K^{(1)}A_{j+1} = F^{(1)}$$

Equation 4-55.
$$M\frac{H_{j+1} - \tilde{H}}{c} + K^{(2)}H_{j+1} = F^{(2)}$$

or

Equation 4-56.
$$\frac{M}{c}A_{j+1} + K^{(1)}A_{j+1} = F^{(1)} + \frac{M}{c}\tilde{A}$$

Equation 4-57.
$$\frac{M}{c}H_{j+1} + K^{(2)}H_{j+1} = F^{(2)} + \frac{M}{c}\tilde{H}$$

or in residual form:

Equation 4-58.
$$R = \begin{bmatrix} R^{(1)} \\ R^{(2)} \end{bmatrix} = \begin{bmatrix} \frac{M}{c}A_{j+1} + K^{(1)}A_{j+1} - F^{(1)} - \frac{M}{c}\tilde{A} \\ \frac{M}{c}H_{j+1} + K^{(2)}H_{j+1} - F^{(2)} - \frac{M}{c}\tilde{H} \end{bmatrix}$$

This completes the time discretization. The remaining equations derive the form for the Jacobian needed for Equation 4-27 in order to do the Newton iterations. We seek the first differential of R in Equation 4-58. For $n+1$ iterations, we have:

Equation 4-59.
$$\delta R^{(1)} = \frac{M}{c}\delta A_{j+1} + K^{(1)}\delta A_{j+1} + \delta K^{(1)}A_{j+1} - \delta F^{(1)}$$

where

Equation 4-60.
$$\delta K^{(1)} = \delta\left[k_{ij}^{(1)}\right] = \left[-\int_{\Omega}k_r mH^{m-1}\varphi_i\varphi_j\delta H d\Omega\right] =$$
$$\left[-\int_{\Omega}k_r mH^{m-1}\varphi_i\varphi_j\sum\varphi_k\delta H_k d\Omega\right]$$

Equation 4-61.
$$\delta K^{(1)}A_{j+1} = \left[-\int_{\Omega}k_r mH^{m-1}\varphi_i A_{j+1}^n\varphi_k d\Omega\right]\delta H_{j+1} = \frac{\partial K^{(1)}}{\partial H}A_{j+1}$$

85

Equation 4-62.
$$\delta F^{(1)} = \left[-\int_\Omega k_r m H^{m-1} \varphi_i \delta H d\Omega \right] =$$

$$\left[-\int_\Omega k_r m H^{m-1} \varphi_i \varphi_j d\Omega \right] \delta H_{j+1} = \frac{\partial F^{(1)}}{\partial H}$$

Equation 4-59 becomes

$$\delta R^{(1)} = \frac{M}{c} \delta A_{j+1} + K^{(1)} \delta A_{j+1} + \frac{\partial K^{(1)}}{\partial H} A_{j+1} \delta H_{j+1} -$$

$$\frac{\partial F^{(1)}}{\partial H} \delta H_{j+1}$$

Equation 4-63.

Equation 4-64. $\delta R^{(2)} = \frac{M}{c} \delta H_{j+1} + K^{(2)} \delta H_{j+1} + \delta K^{(2)} H_{j+1} \delta A_{j+1} - \delta F^{(1)}$

Equation 4-65.
$$\delta K^{(2)} = \delta \left[k_{ij}^{(2)} \right] = \left[\int_\Omega D \nabla \varphi_i \cdot \nabla \varphi_j \delta A d\Omega \right]$$

$$\delta K^{(2)} H_{j+1} = \left[\int_\Omega D \nabla \varphi_i \cdot \nabla H_{j+1}^n \varphi_k \delta A \right] \delta A_{j+1} =$$

$$\frac{\partial K^{(2)}}{\partial H} H_{j+1} \delta A_{j+1}$$

Equation 4-66.

$$\delta R^{(2)} = \frac{M}{c}\delta H_{j+1} + K^{(2)}\delta H_{j+1} + \frac{\partial K^{(2)}}{\partial A}H_{j+1}\delta A_{j+1} +$$

Equation 4-67. $\dfrac{\partial F^{(2)}}{\partial H}\delta H$

Equation 4-68. $\qquad \delta F^{(2)} = -\left[\int\limits_{\partial\Omega^e} k_4\varphi_i\varphi_j\delta l\right]\delta H_j$

In summary,

Equation 4-69. $\delta R^{(1)} = \dfrac{M}{c}\delta A_{j+1} + K^{(1)}\delta A_{j+1} + \dfrac{\partial K^{(1)}}{\partial H}A_{j+1}^n\delta H_{j+1} - \dfrac{\partial F^{(1)}}{\partial H}\delta H_{j+1}$

$$\delta R^{(2)} = \frac{M}{c}\delta H_{j+1} + K^{(2)}\delta H_{j+1} + \frac{\partial K^{(2)}}{\partial A}H_{j+1}^n\delta A_{j+1} + \frac{\partial F^{(2)}}{\partial H}\delta H$$

where

$$\frac{\partial K^{(1)}}{\partial H}A_{j+1} = \left[-k_r m H^{m-1}A\int\limits_{\Omega}\varphi_i\varphi_j d\Omega\right]$$

$$\frac{\partial F^{(1)}}{\partial H} = \left[-k_r m H^{m-1}\int\limits_{\Omega}\varphi_i\varphi_j d\Omega\right]$$

$$\frac{\partial K^{(2)}}{\partial A}H_{j+1} = \left[\int\limits_{\Omega}D\nabla\varphi_i\nabla\varphi_j\cdot\sum H_k\varphi_k\delta A\right]$$

Equation 4-70.

A and H refer to A^n_{j+1} and H^n_{j+1} respectively. n is the nth iteration. In the matrix form:

Equation 4-71. $\delta R = \begin{bmatrix} \delta R^{(1)} \\ \delta R^{(2)} \end{bmatrix} = \begin{bmatrix} \dfrac{M}{c} + K^{(1)} & \dfrac{\partial K^{(1)}}{\partial H} A_{j+1} - \dfrac{\partial F^{(1)}}{\partial H} \\ \dfrac{\partial K^{(2)}}{\partial A} H^n_{j+1} & \dfrac{M}{c} + K^{(2)} - \dfrac{\partial F^{(2)}}{\partial H} \end{bmatrix} \begin{bmatrix} \delta H_{j+1} \\ \delta A_{j+1} \end{bmatrix} = R'\delta U$

For the $(n+1)$th iteration:

Equation 4-72. $\begin{bmatrix} R'_{11} & R'_{12} \\ R'_{21} & R'_{22} \end{bmatrix} \begin{bmatrix} \delta A \\ \delta H \end{bmatrix} = \begin{bmatrix} -R_1(A^n_{j+1}) \\ -R_2(H^n_{j+1}) \end{bmatrix}$

$R_2\left(H^n_{j+1}\right)$ is not known within each element, since $F^{(2)}$ relates to adjacent elements. But R_1 is not influenced by other elements.

Equation 4-73. $\qquad R'_{11}\delta A + R'_{12}\delta H = R_1$

where

Equation 4-74. $\qquad \delta A = (R'_{11})^{-1}(R_1 - R'_{12}\delta H)$

Substituting Equation 4-74 into Equation 4-72 gives

Equation 4-75. $\qquad R'_{21}(R'_{11})^{-1}(R_1 - R'_{12}\delta H) + R'_{22}\delta H = R_2$

or

Equation 4-76. $[R'_{22} - R'_{12} - (R'_{11})^{-1}R'_{12}]\delta H = -R_2 - R'_{21}(R'_{11})^{-1}R_1$

The element stiffness and the force needed to be incorporated into the global system is:

Equation 4-77. $\qquad \bar{R}'\delta H = \bar{R}$

88

where

Equation 4-78.
$$\bar{R}' = R'_{22} - R'_{12} - (R'_{11})^{-1} R'_{12}$$

and

Equation 4-79.
$$\bar{R} = -R_2 - R'_{21}(R'_{11})^{-1} R_1$$

After solving this system, δA can be found from Equation 4-74.

4.6. Algorithm Performance

It is observed that the Krylov subspace acceleration (KSA) allows for a greater than
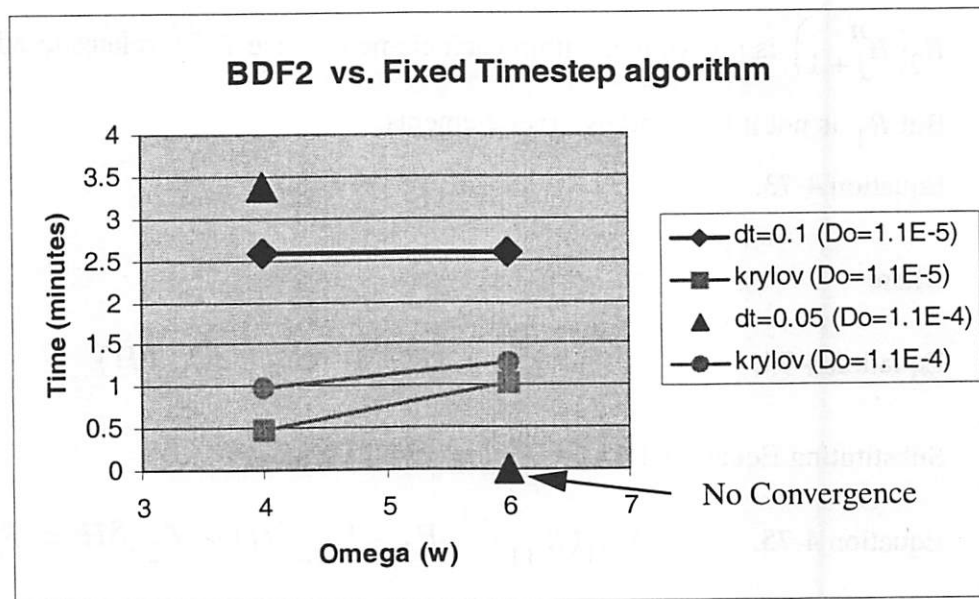
Figure 4-1. Comparing BDF2 with Krylov subspace acceleration to fixed timestep scheme.

PEB time=30s, k_r=5.5cm^3/s, number of nodes=726, Predictor Error Tolerance=1E-3.

order of magnitude decrease in simulation time when compared to variable time advance-

ment schemes without acceleration. Because of the predictor error constraint imposed on

the automatic timestep determination, the BDF2 without KSA takes time steps on the order

of 10^{-4} in order to satisfy the error control. Thus, a typical PEB simulation with 60 seconds bake time takes more than 3 days to simulate! To decrease the simulation time for comparison with the KSA, a fixed timestep scheme is used to allow for large timesteps. Unfortunately, solution using the fixed timesteps algorithm fails to meet the accuracy requirements. The results are presented here for comparison purpose only. Depending on the stiffness of the system, the low accuracy in the fixed timestep calculation results in non convergence of the Newton iterations.

Figure 4-1 compares a fixed timestep algorithm with a Krylov subspace accelerated BDF2 algorithm under the following conditions: PEB time=30s, k_r=5.5cm^3/s, #nodes=726, Error Tolerance=10^{-3}. It is seen that the Krylov/BDF2 algorithm is at least 2X faster than the fixed timestep algorithm, although it is more than order of magnitude more accurate than the fixed timestep algorithm. When the system is made stiffer by setting the pre-exponential diffusion terms as follows, Do=1.1E-4 and ω=6, the fixed timestep algorithm fails to converge even when the timestep is reduced to 0.025.

Figure 4-2 shows the speed-up achieved by the partial variable elimination method derived Section 4.5. This approach achieves up to 4X speedup over the traditional FEM formulation[47]. In general, the speed-up is $O(n^2)$, where n is the number of system variables. In the example shown in Figure 4-2, the system variables were the acid concentration, H, and the deprotected sites concentration A.

Another PEB simulation algorithm proposed by Cheng *et al.* uses high order space approximations where the PDE is solved by iteratively approximating the solution with a
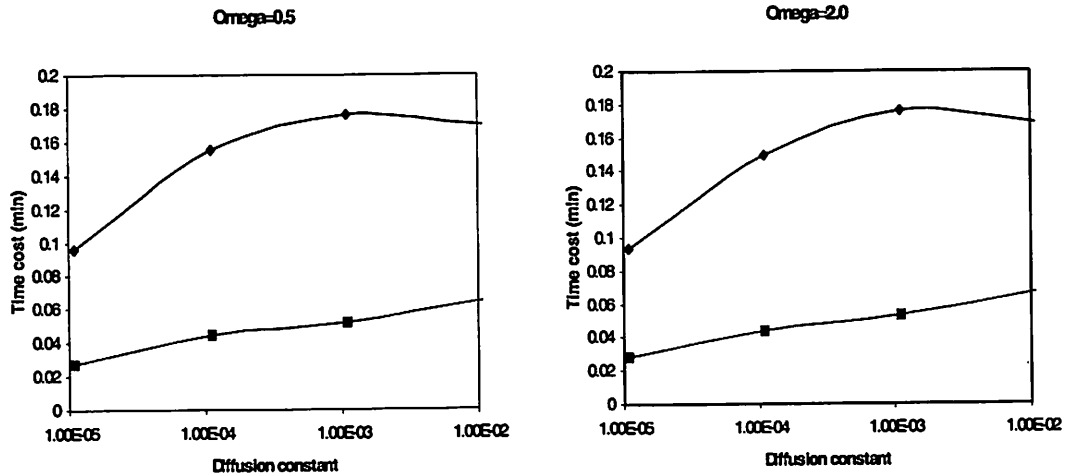
Figure 4-2. Speedup improvements for the variable elimination algorithm.

3-variable polynomial on space[52]. It is a modification of the Finite Difference Method (FDM) and solves high order partial differential expansions so that as large as possible timestep can be used. In general, the timestep of the modified algorithm can be two orders of magnitude more than traditional FDM for a given error tolerance. Thus, the algorithm allows for a gain in computation speed without compromising accuracy.

Figure 4-3 compares the performance of the modified FEM (partial variable elimination) and the modified FDM (higher order space approximations). As shown, the modified FEM runs faster than the modified FDM. However, the modified FDM requires less memory resources. A major advantage of the FEM over the FDM is its capability to simulate volume shrinkage as observed in chemically amplified resist as well as polymer stress effects.
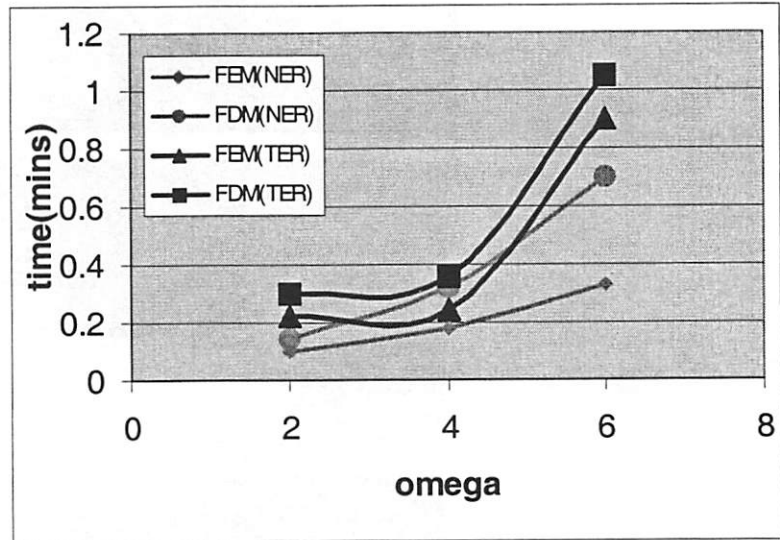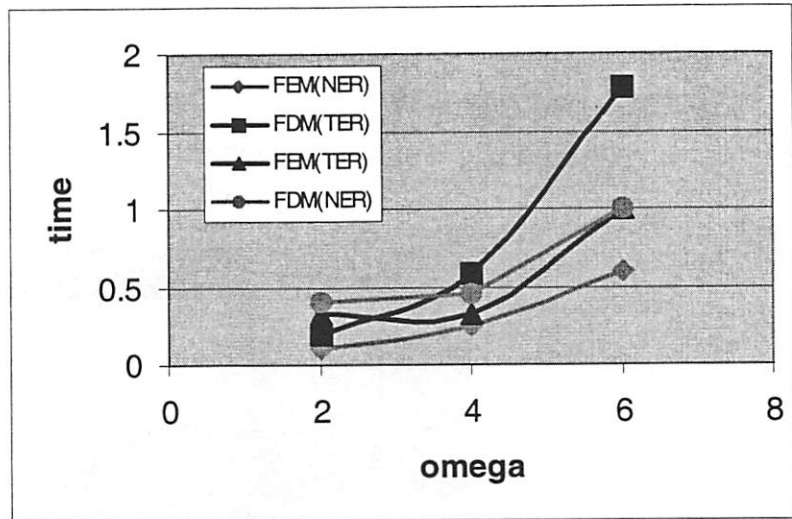
Figure 4-3. Comparing variable elimination FEM and modified FDM algorithms for 2D features at different error controls.

Number of nodes 400. PEB time 60s. TER: Tight Error Control (Predictor Error Tolerance=1E-6); NER: Normal Error Control (Predictor Error Tolerance 1E-6).

4.7. 2D PEB Simulation Results

The models presented in Chapter 2 are used as test vehicles for the numerical algo-

rithms of this chapter to simulate post exposure bake (PEB). SPLAT[73] is used for the

resist exposure simulation. Simulation capability of special technology issues such as line

end shortening (LES) effects in DUV resist are also presented.

Figure 4-4 shows the simulation results of surface imaged resist. The top figure
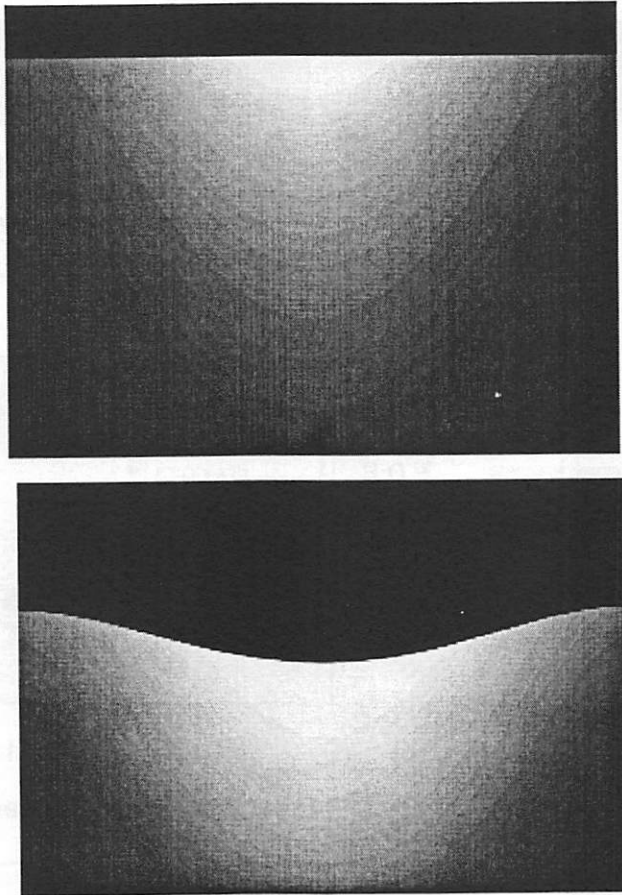
Figure 4-4. Surface Image resist shrinkage after PEB

The top figure shows the acid concentration in resist after SPLAT and BLEACH simulations. The bottom figure shows the deprotected sites concentration and the resist volume shrinkage

shows the acid concentration in resist after SPLAT simulations. The bottom figure shows

the deprotected sites concentration and the resist volume shrinkage. The simulation perfor-

mance is under 3 minutes on DEC Alpha 600MHz machine.

Figure 4-5 shows the PEB simulation for DUV chemically amplified resist for the case of volume shrinkage (right) and no volume shrinkage (left). Figure 4-5a shows the initial acid concentration. Figure 4-5b shows the acid concentration after 60 seconds PEB time and Figure 4-5c shows the deprotected sites concentration after PEB. The following simulation parameters were used to obtain this result: $D_o = 1 \times 10^{-6} \frac{\mu m^2}{s}$, $P_o = 0.5$,

$k_o = 1.0 \frac{\mu m^3}{s}$, $\beta = 0.001$, $t_r = 3.0 s$, $\alpha = 1.0$, $\omega = 100$, and $v = 1.0$. The simulation performance is under 10 minutes. The deprotected sight concentration exhibits a very sharp concentration gradient as predicted by the MBT model.

Finally, 2D simulation and experiment of LES is presented. Figure 4-6 shows both simulated profile and scanning electron micrograph (SEM) of line end shortening feature. By overlapping the SEM and simulation, Figure 4-6c shows that a good matching is obtained between the experiment and the simulation.
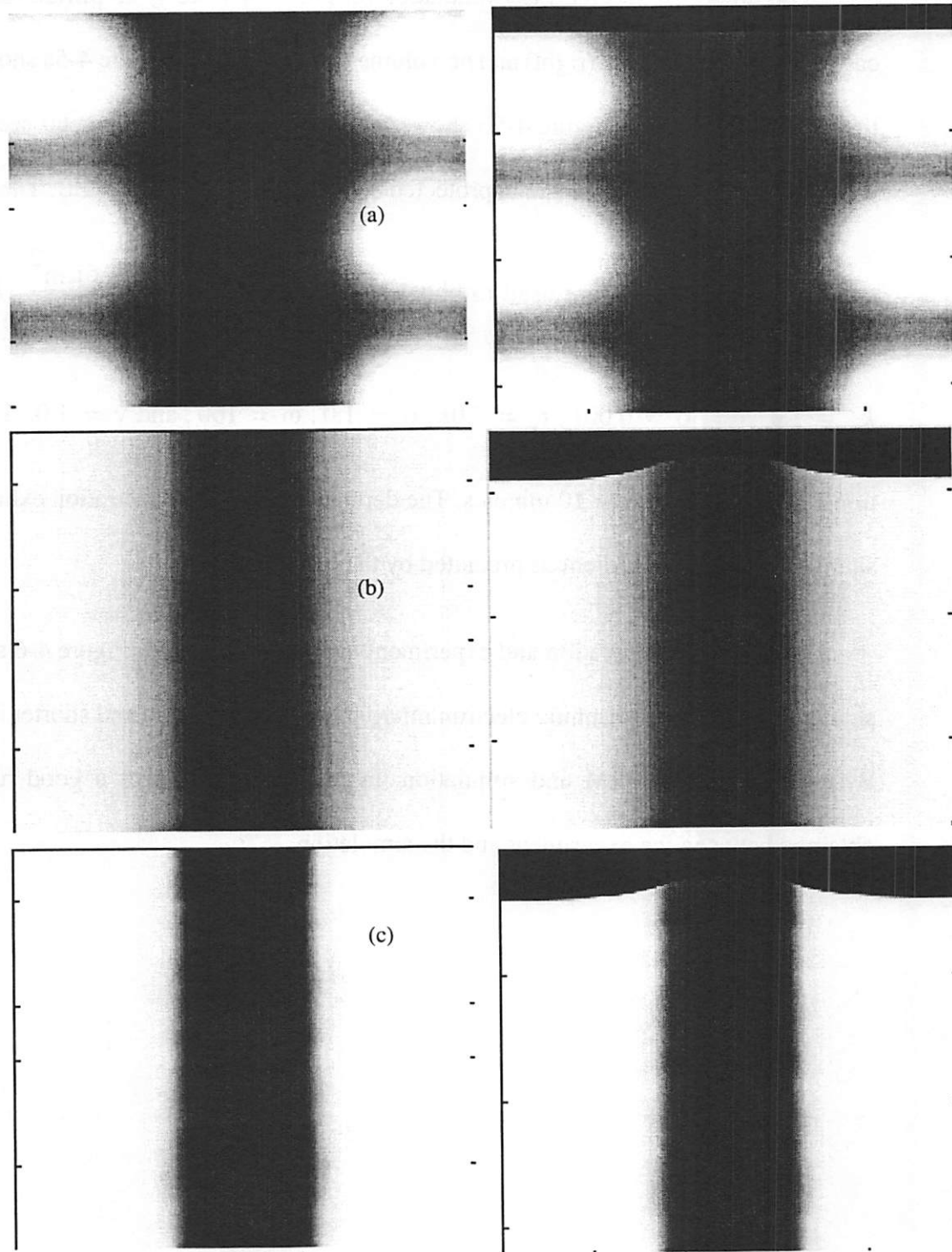
Figure 4-5. DUV chemically amplified resist

(a) initial acid concentration. (b) acid concentration after 60 seconds PEB time (c) deprotected sites concentration. Note the sharp contrast between protected and deprotected regions
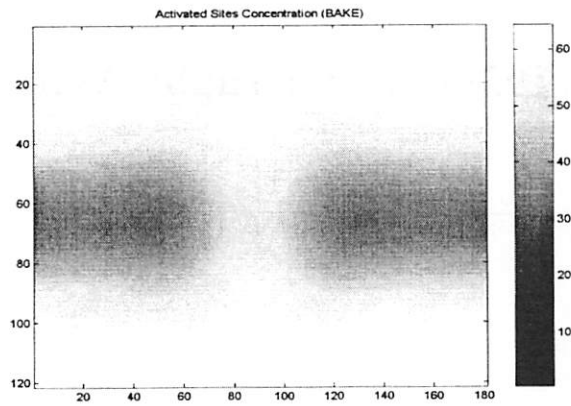
(a)
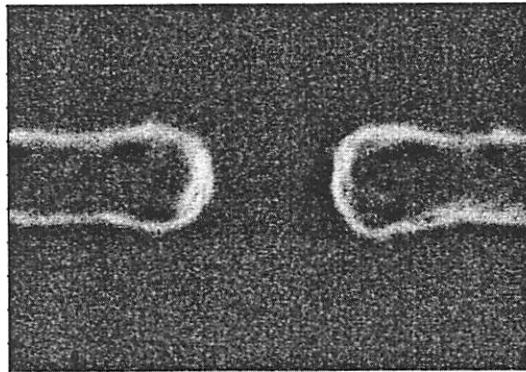
(b)
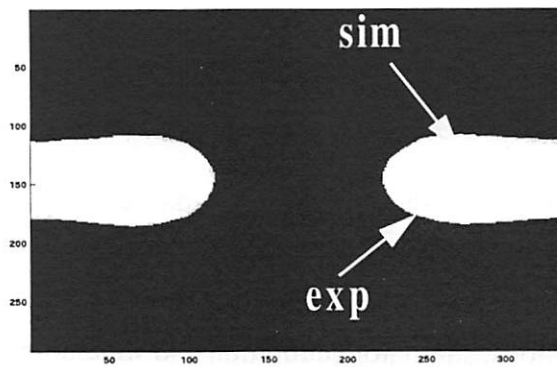
(c)

Figure 4-6. 2D LES Modeling

(a) STORM Simulation. (b) Scanning Electron micrograph (c) simulation/SEM overlap. SEM (b) and overlap of STORM simulation and SEM (c) were provided by Mosong Cheng [52].

5 193nm Lithography Applications

5.1. Introduction

As new optical lithography exposure tools and resist materials for deep submicron applications emerge, accurate models and simulators become indispensable tools for optimizing the processes. Currently, 193nm lithography is a leading candidate for integrated circuits fabrication using design rules below 130nm. In order to provide quantitative support for 193nm resist material development and process optimization, resist models in the STORM program [91] are adapted to 193nm resist formulations. This work was done in collaboration with Frank Houlihan, Om Nalamasu, Pat Watson and Ray Cirelli of Bell Laboratories, and Allen Gabor and Ognian Dimov of Arch Chemicals. All the experiment data were taken by the author under the guidance of the above collaborators, except the data for characterizing photoacid generation, which were taken by Ognian Dimov. All parameter extractions, simulator calibration and simulations results were performed by the author.

Much work has been done on modeling methodology for DUV resists for 248nm lithography[92][93][94]. Similar modeling methodology can be applied to 193nm resists. This work follows the method of "base additions" approach used by Szmanda[95] to

extract the acid generation rate parameter. Ferguson's methodology using FTIR data[92] is applied to extract the reaction rate parameters. The diffusion parameter extractions uses the line end shortening (LES) methodology proposed by Cheng[96]. Simulation results will be compared to experiment for LES features.

5.2. Modeling 193nm Chemically Amplified Resists

5.2.1. Resist Chemistry

The 193nm chemically amplified resists (CAR) used in this example are formulated with cycloolefin-maleic anhydride copolymers, cholate based dissolution inhibitor, non-aflate photoacid generator (PAG) and base[97]. Exposing the resist to 193nm light (ArF excimer laser) generates acid from the PAG. During PEB, the photo-generated acid catalyzes a thermally induced reaction that removes the t-butyl protecting groups, rendering the deprotected region soluble in aqueous developer. Meanwhile, the acid diffuses towards unexposed areas. The presence of base in unexposed areas neutralizes the acid and thus limits the deprotection reaction to the vicinity of the initially exposed region.

5.2.2. Experimental

Bell Laboratories/Arch Chemicals dense resist formulations were studied. All samples were processed under the following conditions unless otherwise stated. Resist samples were spun on HMDS primed 8 inch inorganic ARC coated wafers at 2245 rpm for 30 s. The samples were then soft baked at 140 °C for 90 s. Exposures were carried out on an ISI ArF 0.60 NA, $\sigma = 0.7$, small field catadioptric exposure system. After exposure, PEB

was performed at 155 °C for 90 s. The wafers were puddle developed with OPD-262

developer for 24 s. All resist processes were performed on TEL Superclean Track ACT 8.

Resist thickness was measured using a Nanospec AFT thickness gauge. SEM micrographs

were obtained using KLA Tencor CD SEM.

5.2.3. Model Equations

5.2.3.1. Exposure model

SPLAT[91] is linked to the Dill *ABC* model [98] to simulate the resist exposure.

The *ABC* parameters are extracted by monitoring the resist transmission as a function of

exposure dose and then fitting the parameters to the results. Traditionally, the Dill model

is adapted to the acid generation reaction for chemically amplified resists where *C* is

assumed to be the acid generation rate (photolysis rate) constant. Unfortunately, absor-

bance changes in CAR during exposure have been found to have little correlation to the

amount of photoacid generated[95]. This report differentiates between the resist bleaching

rate constant, C_B, and photolysis rate constant, *C*. The "base additions" method described

by Szmanda[95] is used to extract the photolysis rate constant. This method is based on

casting the Dill model in the form of exposure energy in order to use dose-to-clear (E_0)

changes as a function of base quencher concentration in the resist to monitor the acid con-

centration. For "small" quantities of base, the equation takes the following form:

Equation 5-1. $$H_0 = \frac{H}{P_0} = EC\alpha \quad \text{where } \alpha = \frac{1 - e^{-a}}{a}$$

P_0 is the PAG concentration, α is the attenuation correction and a is attenuation coefficient. From the above equation, by monitoring E_0 as a function of base/PAG ratio, one can extract the actual Dill C parameter. SPLAT is used to simulate the local normalized intensity I_s in resist. The initial local acid concentration is then described by

Equation 5-2. $\qquad H_0 = 1 - \exp(-CE) = 1 - \exp(-CI_s t) \quad \text{where } t = \dfrac{D_e}{I_0}$

Here, t is the exposure time, D_e is the exposure dose and I_o is the normalized intensity at the wafer plane.

5.2.3.2. Post exposure bake model for 193nm resist

The PEB modeling is based on the chemical and physical mechanisms that govern the latent image formation. The model takes the form of Equation 2-22:

Equation 5-3. $\qquad \dfrac{\partial A}{\partial t} = k_r(1-A)H$

Equation 5-4. $\qquad \dfrac{\partial H}{\partial t} = -k_l HB + \nabla(D\nabla H)$

Equation 5-5. $\qquad \dfrac{\partial B}{\partial t} = -k_l HB$

Equation 5-6. $\qquad D = D_0 \exp(\omega(1-A))$

Equation 5-3 describes the deprotection (A) rate during the thermally induced cleavage of the normalized protecting groups (1-A) by the photogenerated acid (H). Equation 5-4 tracks changes in the acid concentration due to protected sites enhanced diffusion (Equation 5-6) and acid loss from base neutralization. Equation 5-5 tracks the base concentration. k_r and k_l are the reaction rate and acid loss rate constants respectively.

Experimental data supports negligible diffusion in deprotected polymers and rapid transport in protected polymer[54]. Thus, the diffusivity parameter, D, is non-Fickean and is assumed to be an exponential function of protected sites concentration.

5.2.4. Parameter Extractions

5.2.4.1. Extraction of exposure parameters

The parameters needed to simulate the resist exposure are the bleachable absorption coefficient, A, the non bleachable absorption coefficient, B, the resist bleaching rate constant, C_B, and the acid generation rate constant C. To extract these parameters, the resist samples were prepared by spin coating the resist on HMDS primed quartz substrate at a speed of 3000 rpm for 30 s. The spin was followed by a pre-exposure bake of 150 °c for 2 min to remove excess solvent. The samples were placed on a black cardboard (to minimize standing wave effects) and exposed to 193nm radiation using Lamda Physik excimer laser model LPX 100.

The resist transmission at 193nm was measured using the HP 845x UV-visible system. To extract the A, B and C_B parameters, STORM simulation of resist transmission using the Dill model was done and fitted to the experimental results. Figure 5-1a shows a good agreement between 193nm transmission data and STORM numerical solution of the Dill ABC model. Values of $A = -1.49$, $B = 2.55$ and $C_B = 1.105 \times 10^{-3}$ best fit the experimental data.

To extract the acid generation rate constant, C, the method of "base additions" [95] was used. Several resist samples were prepared that contained identical components except for different small concentrations of base quencher. E_0 was then measured as a function of

101

193nm Optical Transmission

Photolysis rate constant parameter extraction
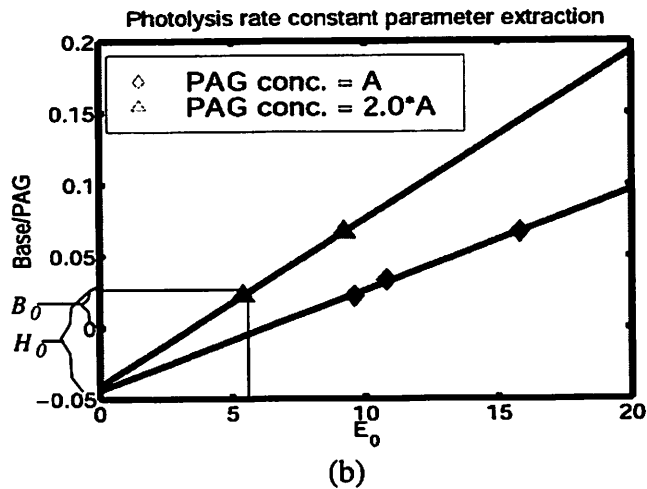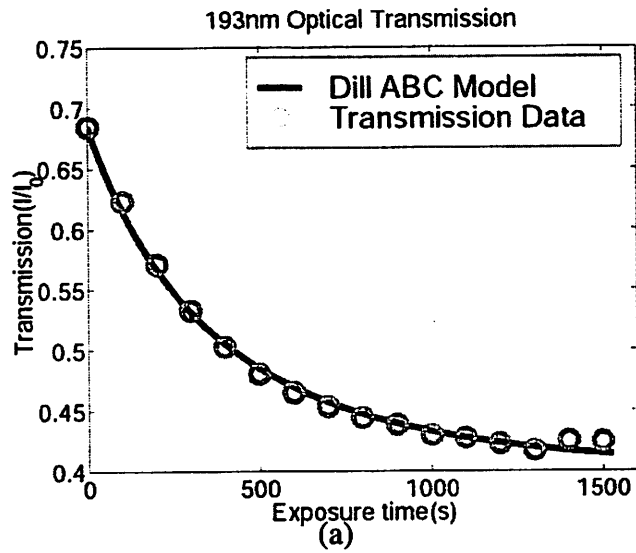
Figure 5-1. Extracting Exposure Parameters

(a) Fitting transmission model to data to extract Dill ABC exposure parameters. (b) Extracting photolysis rate constant parameter using "base additions" method.

base/PAG mole ratio. Figure 5-1b shows that E_0 changes as a function of base/PAG ratio.

The slope gives photolysis rate constant, C, while the magnitude of the intercept gives the

threshold amount of photoacid necessary to clear the resist. The uncorrected values of

C=0.0104 cm^2/mJ and C=0.0118 cm^2/mJ were obtained for PAG concentration A and 2xA

102

respectively. The resist samples used in this study contains PAG concentration 2xA. Thus, all simulation results use C=0.0118 cm^2/mJ.

5.2.4.2. Extraction of reaction rate parameters

To extract the reaction rate parameters, diffusion effects during the PEB has to be minimized so that the effect of acid diffusion on reaction rate parameters are negligible. To minimize diffusion effects, organic ARC DUV 42-11 was spun on 8 inch wafers at 2740 rpm for 30 s. The ARC was baked at 200 °c for 60 s. Resist samples were prepared on the ARC coated wafers using the processing conditions and tools described above. Open frame exposures were carried out with doses ranging from 2 mJ/cm^2 to 50 mJ/cm^2. Because of the small field size of the ISI stepper (1.5mm X 1.5mm), 10 X 10 exposed fields were stitched together to provide a large enough exposed area for FTIR spectroscopy. From these large area open frame exposures, acid diffusion at the edges of exposed region have negligible effects on the reaction. Furthermore, the ARC substrate minimizes standing waves such that acid concentration profile after exposure is close to uniform. From these conditions, it is reasonable to assume that diffusion effects are negligible during PEB. This simplification allows for reaction rate and acid loss parameters to be extracted from open frame exposure experiments to within a few percent, provided that the initial acid (H_0) and base (B_0) concentrations are known.

The Nicolet MAGNA-IR 560 tool was used to monitor the deprotection reaction. The spectra were obtained in transmission mode. Figure 5-2a shows typical results from FTIR spectroscopy. The decrease in absorbance near 1170 cm^{-1} corresponds to the removal of t-butyl protecting groups. To quantify the extent of deprotection, the area under
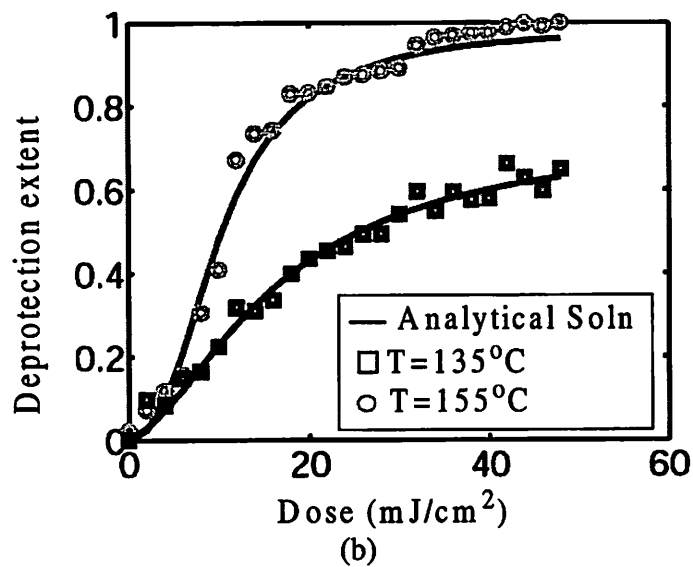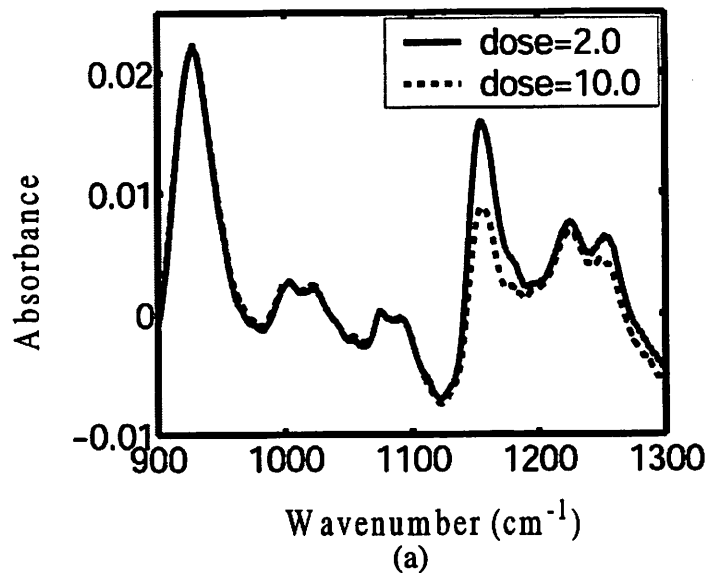
Figure 5-2. Extracting Reaction Parameters

(a) FTIR spectra for doses of 2mJ/cm2 and50mJ/cm2. (b) Fitting analytical solution to FTIR data to extract reaction parameters for bake temperatures 135°C and 155°C.

the peak of deprotected polymer was subtracted from the area under the peak of a fully pro-

tected polymer. This gives a zero extent of deprotection for a fully protected polymer (i.e.

no deprotection). By dividing the results with that of a fully deprotected polymer, the nor-

malized deprotection extent as a function of exposure dose and PEB time were determined. Figure 5-2b shows a good agreement between analytical solution of the model equations, (Section 2.6.3) and FTIR data for the extent of deprotection as a function of exposure dose for bake temperatures 155°C and 135°C. The reaction rate parameters that best fit the data were

$$k_r(155°C) = 0.1974\mu m^3/s \quad k_l(155°C) = 3.022\mu m^3/s$$
$$k_r(135°C) = 0.0427\mu m^3/s \quad k_l(135°C) = 0.150\mu m^3/s$$

5.2.4.3. Extracting diffusion parameter

To characterize diffusion effects on image formation, LES experiments were carried out using the processing conditions described above. Figure 5-3 shows STORM sim-
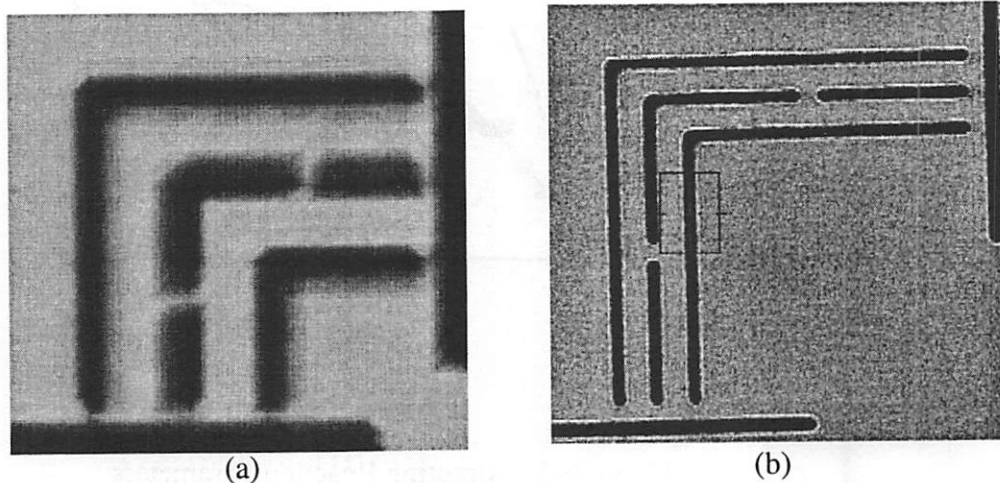
Figure 5-3. Extracting Diffusion Parameters

An example of LES simulation to extract diffusivity parameters. (a) latent image from STORM simulations. (b) SEM micrograph.

ulation and SEM of LES feature. The linewidth measurements for simulated profiles uses

a simple threshold model. This means resist which has deprotection extent higher than a given threshold is considered to develop while resist below this threshold is considered to remain. To obtain the threshold value, a dose response experiment was performed using the above tools and process conditions to determine E_0. E_0 value of $6mJ/cm^2$ was obtained. This gives a normalized threshold deprotection extent value, A_{th}, of 0.3 for PEB temperature of 155 °C and PEB time of 90 s. D_0, ω and A_{th} are tuned to determine the diffusivity parameters that best fit the LES measurements for different bake conditions.

5.2.5. Parameter Optimization

Given the high dimensionality of the parameter space, searching for optimal parameters to fit experimental data is a task best suited for an optimization engine. A large-scale optimization techniques using the Method of Feasible Directions (MFD) algorithm [99] was used for this purpose. The MFD algorithm works as follows. Given some initial parameters, the algorithm changes the parameters in the direction that reduces the error between simulation and experiment. The reaction parameters needed to be optimized are the initial base concentration (B_o), the normalized light intensity at the wafer plane (I_o), the reaction rate constant (k_r) and the acid loss rate constant (k_l).

The initial base concentration, read from the 2xA PAG plot at E_0 (Figure 5-1b) gives B_0=0.025. The initial acid concentration which is B_0 plus magnitude of the intercept gives H_0=0.07. I_s=1.0 for SPLAT open frame exposures. Using H_0 and D_e=$6mJ/cm^2$ (E_0) to solve for I_0 in Equation 2 give I_0=0.976. k_r can be estimated from the high dose region

106

of the FTIR data (See Figure 5-4). Note that for high doses, $H_0 >> B_0$ so acid loss can be assumed negligible. In the case of negligible acid loss and negligible diffusion, Equation 5-3 yields the following solution that can be used to estimate k_r.

Equation 5-7. $$A(t) = 1 - \exp(-k_r H_0 t)$$

From Figure 5-4, using $3E_0$ (18mJ/cm^2) as high dose gives $A=0.9$ and $H_0=0.196$. Using these value in Equation 5-3 gives $k_r=0.131$. There is no straight forward way to approximate k_l from experiment. From experience, a good initial guess for $k_l = 3.0$. Using the initial parameters

$$I_o = 0.976 \quad B_o = 0.025 \quad k_r = 0.131 \frac{\mu m^3}{s} \quad k_l = 3.0 \frac{\mu m^3}{s}$$

the optimization engine gives

$$I_o = 0.95 \quad B_o = 0.065 \quad k_r = 0.194 \frac{\mu m^3}{s} \quad k_l = 3.02 \frac{\mu m^3}{s}$$

The resulting fit is plotted in Figure 5-4. The optimization process takes about 30 seconds.

Beside the deprotection threshold parameter, A_{th}, there are no good experiments that can be used as a guide for the initial guess of the diffusion parameters. $D_0=1 \times 10^{-6}$ and $\omega=1.0$ is chosen as the initial guess. The optimization was performed on the LES feature shown in Figure 5-4b. The gap widths were varied from 120nm to 180nm for the exposure doses, 15.0 mJ/cm^2, 17.4mJ/cm^2 and 19.2mJ/cm^2. The PEB time was 90s. Simulation of each data point takes about 1min on 20X10 grid. Simulating 12 data points were required to complete one round for experimental data comparison. The optimization engine

required 20 rounds to give optimum parameters. Thus the diffusion parameter optimization took about 4 hours. The optimum parameters are

$$D_o = 1 \times 10^{-6} \frac{\mu m^2}{s} \qquad \omega = 4.05 \qquad A_{th} = 0.33$$

The resulting fit to the data is given in Figure 5-4b.
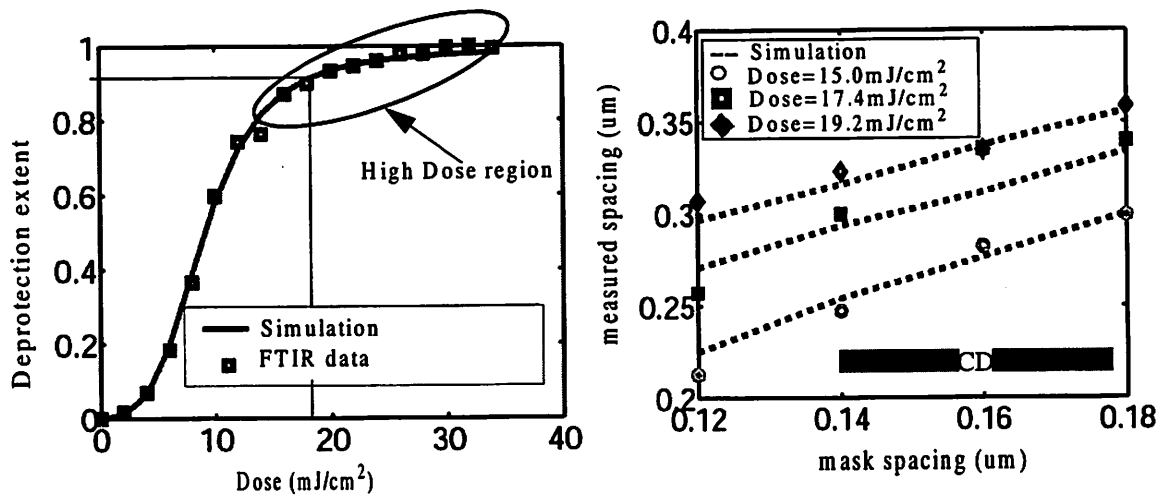
Figure 5-4. Optimizing Model Parameters

(a) Fitting reaction kinetics model to FTIR data to extract reaction parameters. Using high dose values to estimate kr is illustrated. (b) Optimized diffusion parameters' fit to LES data.

5.2.6. Simulation and Experiment Comparison for LES Features

The analytical expression derived in Section 2.6.3 is repeated here for ease of reference.

$$A(t) = 1 - \exp(-k_r H t)$$

$$H(t) = C_1 \tanh(C_1 k_l t - C_2) + C_1$$

$$B(t) = C_1 \tanh(C_1 k_l t - C_2) - C_1$$

$$C_1 = \frac{H_0 - B_0}{2}$$

$$C_2 = \tanh^{-1}\left(\frac{H_0 + B_0}{B_0 - H_0}\right)$$

Equation 5-8.

Equation 5-9. $$\frac{dx}{dt} = \sqrt{k_r Do(1-A)(1-\omega)\exp(\omega(1-A))} \qquad (\omega < 1)$$

A is the extent of deprotection, H is the acid concentration, B is the quencher concentration and dx/dt is the linewidth growth rate. Do and ω are diffusion parameters. Two features are used for LES evaluation with and without OPC. The linewidth is 0.15um. The space widths are varied from 100nm to 360nm. The exposure doses chosen are 13.5 mJ/cm^2, 15mJ/cm^2, 17.4mJ/cm^2 and 19.2mJ/cm^2. The PEB time is 90s. The model parameters used for this simulation were as follows:

TABLE 2. Optimal model parameters

	I_0	B_0	$k_r(\mu m^3/s)$	$k_l(\mu m^3/s)$	$D_0(\mu m^2/s)$	ω	A_{th}
Analytical Solution	1.22	0.036	0.206	3.022	see table1	-0.196	0.30
Full Model	0.95	0.065	0.194	3.022	1.0×10^{-6}	4.05	0.33

Note that the reaction rate and acid loss parameters for the analytical solution and the full model are relatively close as expected.

Figure 5-5 shows comparison between LES measurements from experiment and the analytical solutions. As can be seen, a good fit is obtained for both the OPC feature and

109
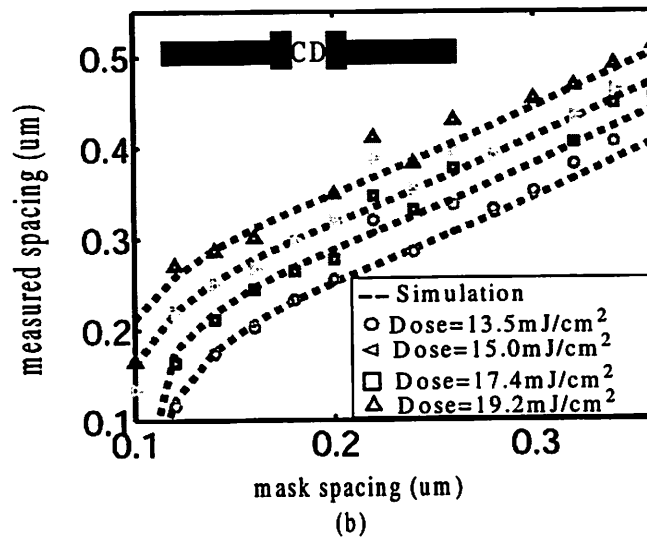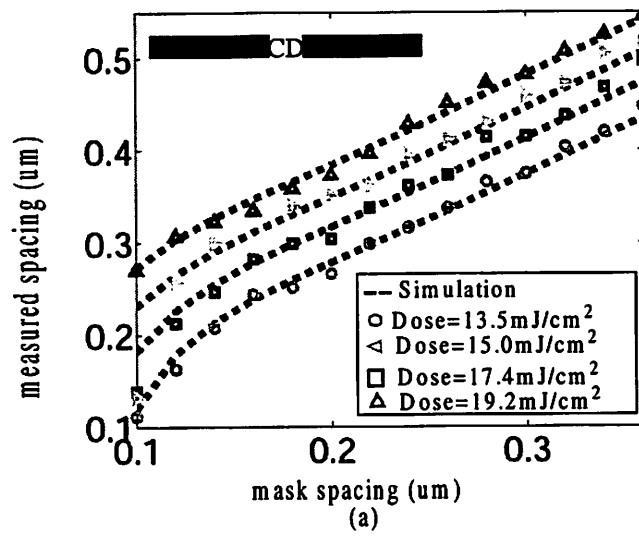
Figure 5-5. LES. Analytical Expression vs. Experiment

Analytical solution prediction of experimental data for different doses for the LES feature with OPC (b) and without OPC (a).

the non-OPC feature. Figure 5-6 shows similar comparison for STORM simulations of the full model. All the results show a good prediction of the experimental data.

No attempt is made to quantify the accuracy since model calibration was done with limited experimental data. For instance LES data was obtained from only one wafer.

110
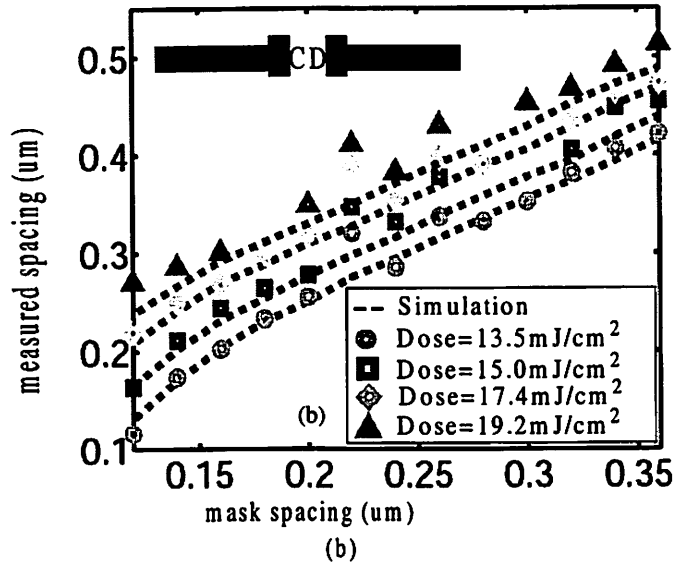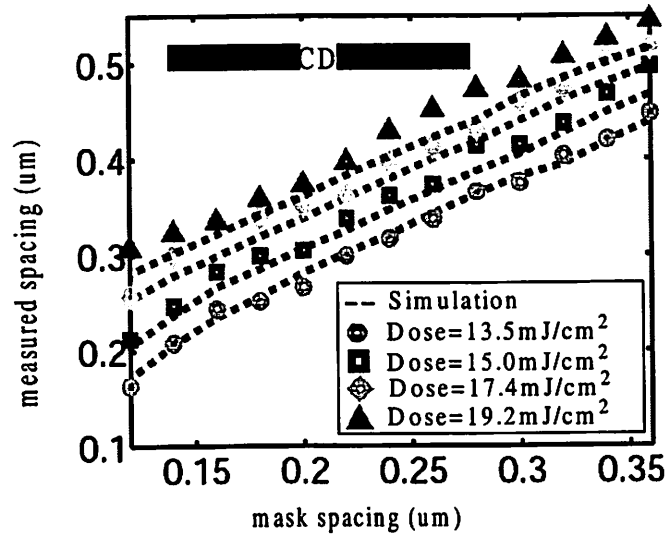
Figure 5-6. 2D Model Simulation vs. Experiment

Analytical solution prediction of experimental data for different doses for the LES feature
with OPC (b) and without OPC (a).

Comprehensive calibration will require obtaining LES data for different bake tempera-

tures and times. LES data for two-dimensional features such as contact holes and isolated

dots are also needed to extract more representative diffusion parameters.
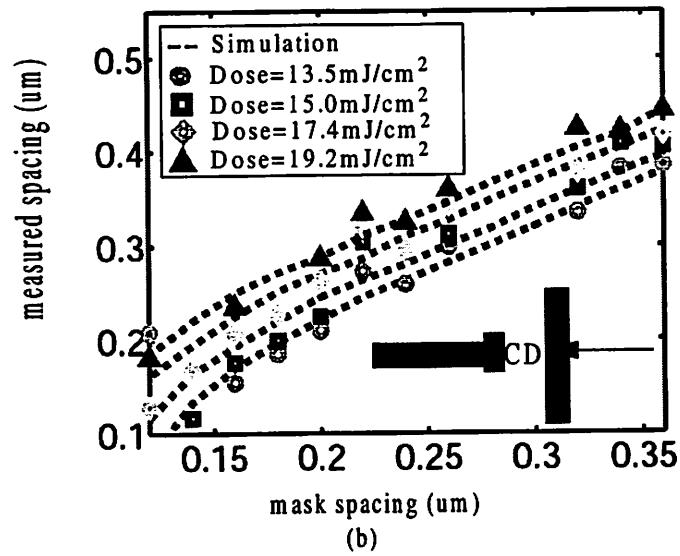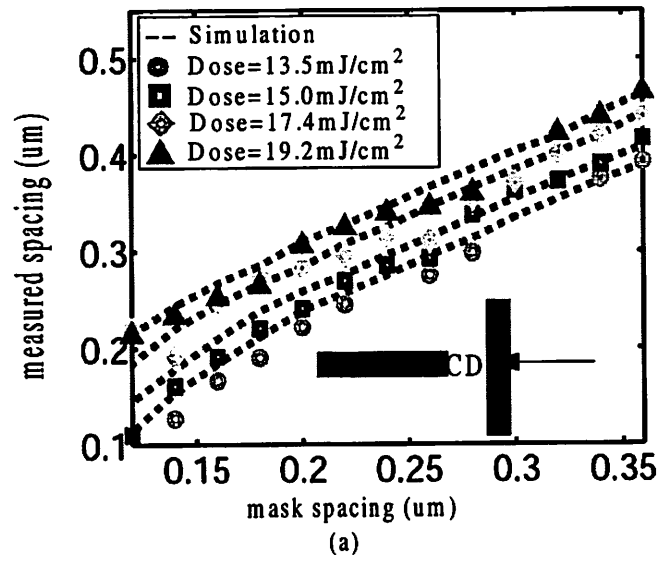
Figure 5-7. 2D Model Simulation vs. Experiment

Simulation vs. experiment for features shown. Good agreement with experimental data is obtained using optimal model parameters.

5.2.7. Summary of 193nm resist modeling

Methodology for extracting the exposure, reaction and diffusion parameters for

248nm resists were used to obtain the modeling parameters for the full model

(Equation 5-3 to Equation 5-6)and analytical expressions (Equation 5-8 and Equation 5-

9). STORM optimization engine was utilized in optimizing the extracted parameters for model calibration. Application results to Bell Labs/Arch Chemical 193nm dense resists show that the resist behavior is well described by both the analytical solution and the full model. While the model calibration presented uses limited data, the STORM simulator and optimization engine makes assessment of process window for large parameter space including resist thickness, exposure dose and focus, bake temperatures and times possible. This provides a cost effective means of optimizing the lithographic process.

5.3. 193nm Photoacid Generator Modeling

5.3.1. Introduction

The relative impact of acid diffusion and line-edge roughness effects on small feature reproduction in 193nm chemically amplified resists (CAR) demands that factors influencing the pattern formation be investigated and controlled to allow extension of CAR for deep submicron resist applications.

Modeling work aimed at understanding the influence of structural changes in photoacid generators (PAGs) on acid generation efficiency, deprotection efficiency and photoacid diffusion in 193nm chemically amplified resists is presented. The analytical expression in Equation 5-8 and Equation 5-9 are used to study the reaction and diffusion properties of the various acids generated by the PAGs. FTIR spectroscopy is used to monitor the generation of photoacid during exposure. Resist thickness loss after PEB as a function of exposure dose is related to the deprotection extent to extract the reaction rate parameters. The effects of the acid size and boiling point on process latitude, line end shortening and line edge roughness are presented. Analytical model predictions of process latititude and line end shortening are also presented and compared to experimental data.

In this study, the photogenerated acid with the smallest molar volume and highest boiling point temperature gave the best overall lithographic performance.

Several studies of the role of PAGs on resist performance are available in the literature. Houlihan et. al. studied the performance of photogenerators of sulfamic acids in chemically amplified single layer resists[100]. Allen *et al.* [101] studied the effects of structural changes in triflic acid generators on the performance of 193nm resists.

The effects of onium salts of perfluorinate sulfonic acids on the lithographic properties of 193nm single layer resists is investigated. A study of the surface composition of a Norbornene/Maleic Anhydride based 193nm photoresist for this class of PAGs suggest that the acid mobility depends on both the boiling point and the molar volume of the acid[102]. The acid size and mobility impact the deprotection efficiency, acid diffusion and line edge profile quality. Of particular interest is the impact associated with mobility and boiling point on the lithographic performance of 193nm resists formulated with these PAGs.

5.3.2. Resist Chemistry

The PAGs used in this study include bis(t-butylphenyl)iodonium perfluorooctanesulfonate (PAG 1), bis(t-butylphenyl)iodonium perfluorobenzenesulfonate (PAG 2), bis(t-butylphenyl)iodonium nonaflate (PAG 3), tris(t-butylphenyl)sulfonium nonaflate (PAG 4) and bis(α-ethoxycarbonyl-2,6-dinitrobenzyl) 1,3-benzenedisulfonate (PAG 5). The PAG structures are shown in Figure 1a. These PAGs were incorporated in 193nm test resists with cycloolefin-maleic anhydride copolymers, cholate based dissolution inhibitor and a base quencher[53]. PAGs 1, 2 and 3 have the same chromophore and are expected to have the same quantum yield.

114
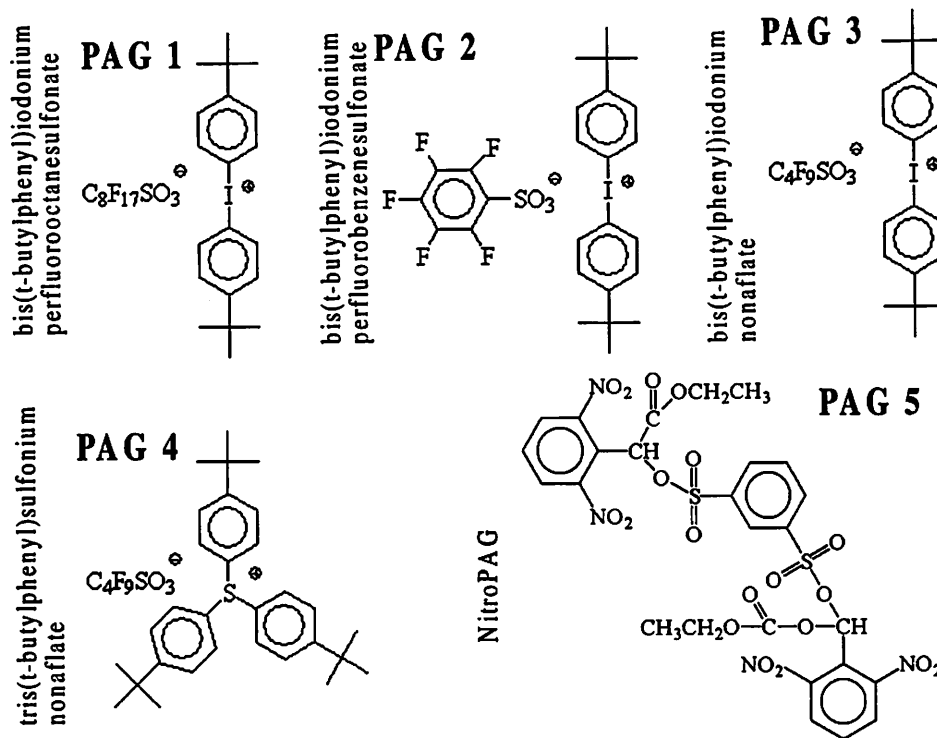
Figure 5-8. Photogenerated Acid Structures

(a) Fitting transmission model to data to extract Dill ABC exposure parameters. (b) Extracting photolysis rate constant parameter using "base additions" method.

PAGs 3 and 4 produce the same acid. The acids that are generated from these PAGs differ in molar volume and boiling point [102] as shown in Figure 5-9b and Figure 5-9b respectively. These different acids allow for the study of influence of the acid size and boiling point on fine feature lithography.

5.3.3. Experimental

All samples were processed under the following conditions unless otherwise stated. Resist samples were spun on HMDS primed 8 inch inorganic ARC coated wafers at 2050
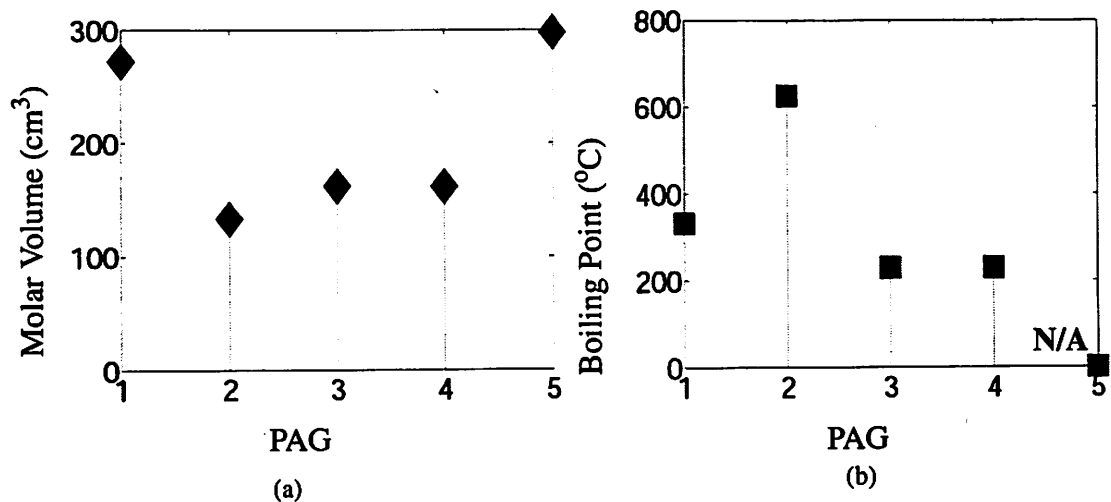
Figure 5-9. PAG Chemical Properties

(a) Fitting transmission model to data to extract Dill ABC exposure parameters. (b) Extracting photolysis rate constant parameter using "base additions" method.

rpm for 30 s. The samples were then soft baked at 145 °C for 90 s. Exposures were carried out on an ISI ArF 0.60 NA, $\sigma = 0.7$, small field catadioptric exposure system. After exposure, PEB was performed at 155 °C for 90 s. The wafers were puddle developed with OPD-262 for 24 s. All resist processes were performed on TEL Superclean Track ACT 8. Resist thickness was measured using a Thermowave Opti-Probe tool. Top-down SEM micrographs and linewidth measurements were obtained using KLA Tencor 8100 CD SEM. All sample cross-section SEM micrographs were obtained using JEOL JSM 6400F scanning microscope except for PAG 2, which was obtained using LEO 1550 scanning microscope.

5.3.3.1. Extraction of exposure parameters

The analytical expression for PEB (Equation 5-8) is used to quantify the lithographic performance of the different PAGs. The initial acid concentration (H_0) is needed to evalu-

ate the above analytical model for PEB. This value is obtained using the Dill exposure

model[50]. To extract the Dill C parameter, a method developed by Byers *et al.* is

employed[103]. The method rewrites Equation 5-7 by substituting the acid generation

equation for H (Equation 5-2), yielding the following expression.

Equation 5-10. $$A(t) = 1 - e^{-k_r(1-e^{-CDose})t}$$

Large dose exposures on anti reflective coated substrates is assumed such that acid

concentration changes with time during PEB is negligible. If low PEB temperature and

time is assumed, Equation 5-10 simplifies to the following.

Equation 5-11. $$A(t) = k_r t(1 - e^{-CDose})$$

Equation 5-10 allows the Dill C parameter to be extracted provided that the above

conditions are met. To meet these conditions, the effect of acid diffusion on deprotection

during PEB has to be minimized. To minimize diffusion effects, organic ARC DUV 42-11

was spun on 8 inch wafers at 2740 rpm for 30 s. The ARC was baked at 200 °c for 60 s.

Resist samples were prepared on the ARC coated wafers using the processing conditions

and tools described above. Open frame exposures were carried out with doses ranging

from 10mJ/cm^2 to 250mJ/cm^2. Because of the small field size of the ISI stepper (1.5mm

X 1.5mm), 10 X 10 exposed fields were stitched together to provide a large enough

exposed area for FTIR spectroscopy. From these large area open frame exposures, acid

diffusion at the edges of exposed region has negligible effects on the deprotection

reaction. Furthermore, the ARC substrate minimizes standing waves such that the acid

concentration vertical profile after exposure is close to uniform. From these conditions, it

is reasonable to assume that diffusion effects are negligible during PEB.

The Nicolet MAGNA-IR 560 tool was used to monitor the deprotection reaction. The spectra were obtained in transmission mode. The decrease in absorbance near 1170 cm^{-1} corresponds to the removal of t-butyl protecting groups.

Figure 5-10 shows the normalized deprotection extent (1138-1170cm^{-1}) vs. dose for
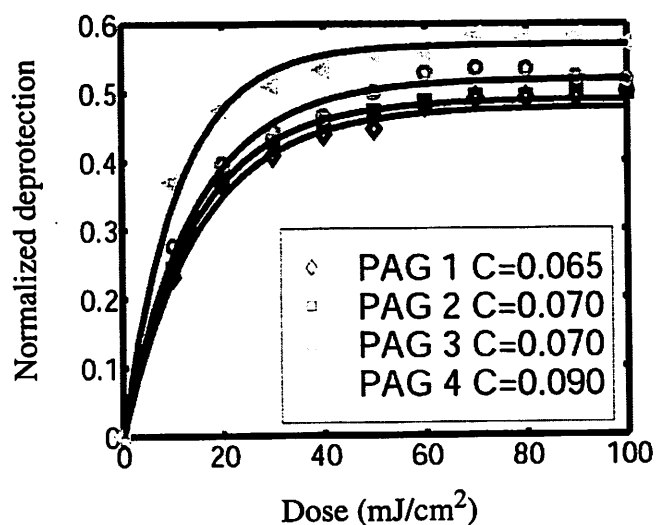
Figure 5-10. Extracting Acid Generation Model Parameters

PAGs 1-4. The samples were baked at 110°c for 45 seconds. The relative C values are obtained by fitting the deprotection vs. dose data. The C values are corrected by a factor such that Equation 5-8 fit deprotection vs. dose data for nominal PEB temperature and time. The correction factor used is (1/6). The corrected C values are plotted in Figure 1c. As expected, PAGs 1,2 and 3 yield similar C values since they have the same chromophore.

5.3.4. Extraction of reaction rate parameters

To extract the reaction rate and acid loss rate constants, resist thickness loss data after PEB is related to the extent of deprotection[104]. The plots of normalized deprotection vs. normalized resist thickness loss give unity slope. This allows us to used thickness loss after PEB data to extract the reaction and acid loss parameters. Figure 5-11 shows the nor-
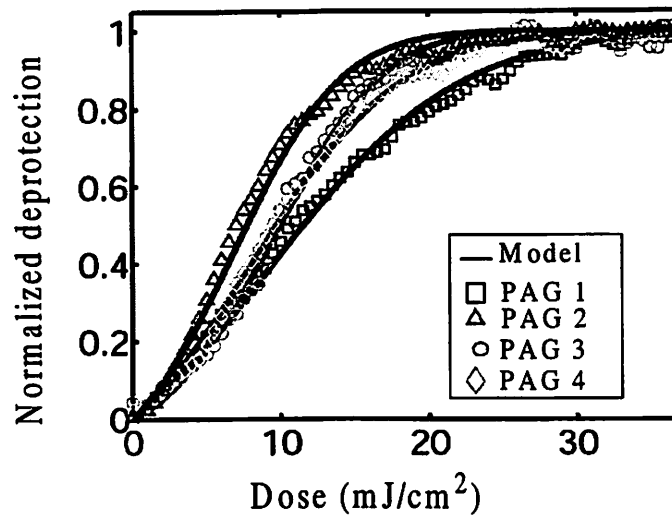
Figure 5-11. Extracting reaction and acid loss rate parameters

malized deprotection extent (from thickness loss data) as a function of exposure dose. The analytical model fit to this data yields the reaction rate constant and the acid loss constant. The reaction rate constant is related to the deprotection efficiency of the acid. Figure 5-12b shows that PAG 2 has the highest deprotection efficiency while PAG 5 has the lowest.
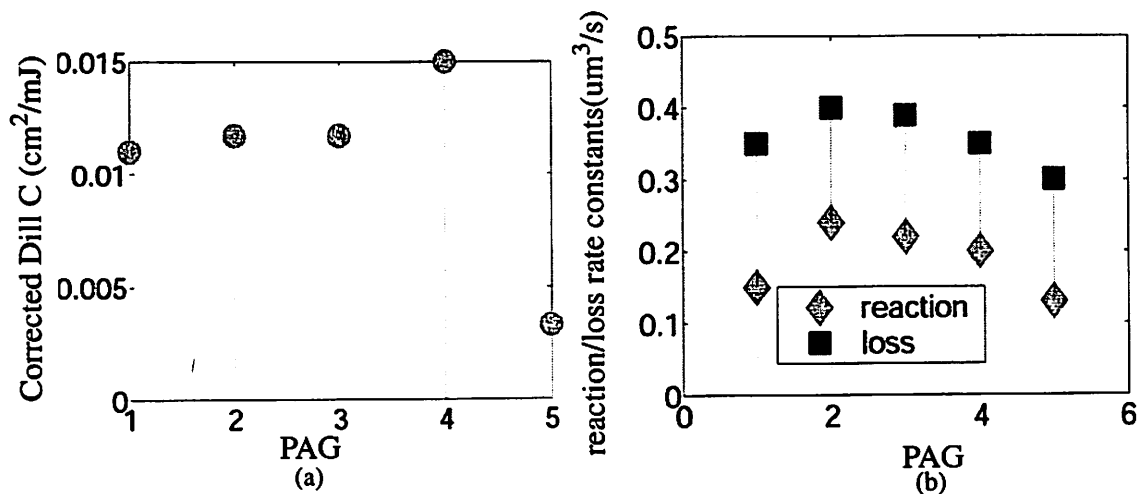
Figure 5-12. Model Parameters for Acid Generation and Reaction

(a) Corrected C values, correction factor (1/6). (b) Reaction and acid loss rate constants.

5.3.4.1. Extracting Diffusion Parameter

To characterize diffusion effects on image formation, line end shortening experiments were carried out using the processing conditions described above. The linewidth measurements for simulated profiles use a simple threshold model. This means resist which has deprotection extent higher than a given threshold, A_{th}, is considered to develop while resist below A_{th} is considered to remain. D_0, ω and A_{th} are tuned to determine the diffusivity parameters that best fit the LES measurements for different doses. Figure 5-17a shows the results of using the analytical model to fit LES data for PAG 1.

The effective diffusion length for the resolution dose of each PAG (Figure 5-13a) as predicted by Equation 5-9 for the above PEB conditions is plotted in Figure 5-13b. The acids generated from PAGs 3 and 4 show high diffusion length due to their small molar
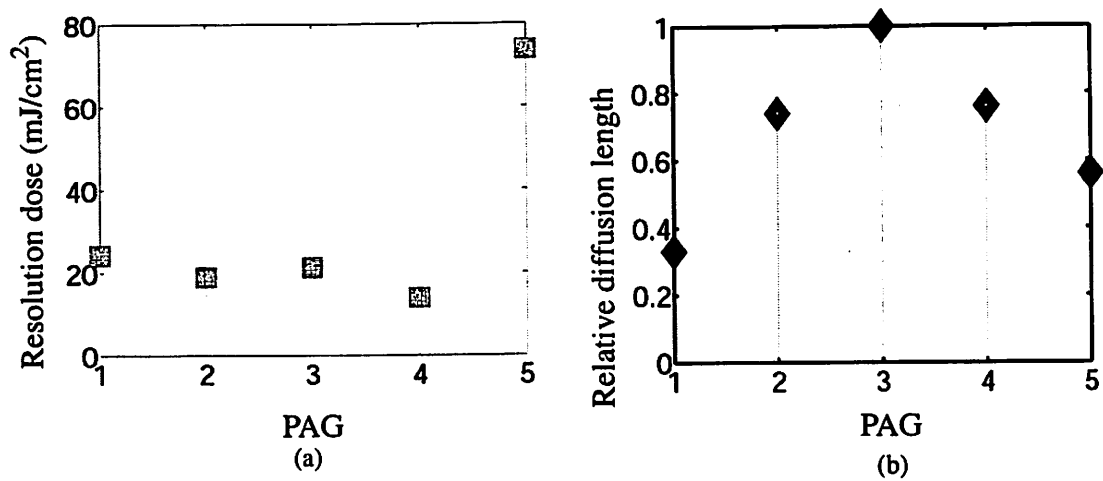
Figure 5-13. Extracting Model Parameters

(a) Resolution dose. (b) Normalized relative diffusion length.

volume and low boiling point. The acid from PAG 1 with relatively larger molar volume

and higher boiling point shows the lowest diffusion length.

5.3.5. Results

5.3.5.1. Resolution

SEM micrographs of 130nm dense features are shown in Figure 5-14. It is seen that

all the PAG samples are able to resolve 130nm dense features except for the PAG 5 sam-

ple which shows more side wall sloping and does not clear the resist to the substrate.

5.3.5.2. Model vs. experiment comparison for process window and LES

The only drawback of the analytical model is that the optimum diffusion parameter

(Do) has to be obtained for different doses, necessitating a lookup table for Do as a func-

tion of dose. Furthermore, the optimum Do values and threshold value (A_{th}) are different

for lines (process window prediction) and spaces (line end shortening prediction). How-
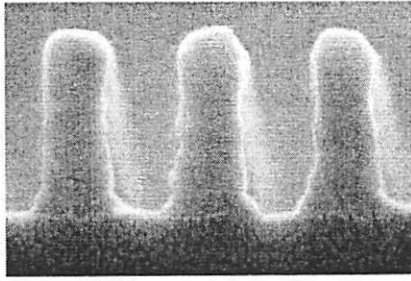
PAG 1
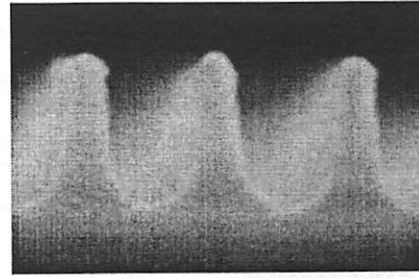
PAG 2
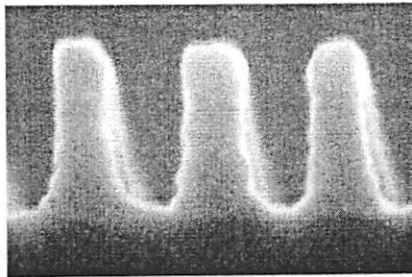
PAG 3
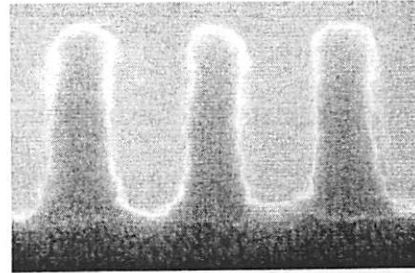
PAG 4
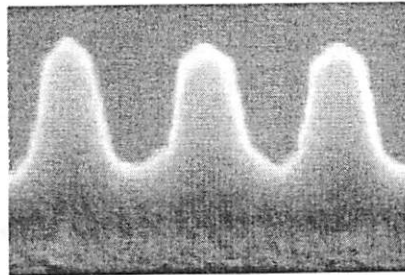
PAG 5

Figure 5-14. 130nm dense lines for PAG samples

ever this custom-tailoring of Do and A_{th} to specific lithographic conditions allow the model to predict experimental data with high accuracy.

The parameters used in the model prediction for process windows and line end short-

ening are summarized in Table 3 The process windows for 130nm lines at +/-10% CD

TABLE 3. Optimal model parameters

	B_0	*Dill C*	k_r($\mu m^3/s$)	k_f($\mu m^3/s$)	ω	A_{th} *(space)*	A_{th} *(line)*
PAG 1	0.065	0.0110	0.15	0.35	0.9	0.30	0.41
PAG 2	0.090	0.0117	0.24	0.40	0.9	0.14	0.37
PAG 3	0.083	0.0117	0.22	0.39	0.9	0.20	0.50
PAG 4	0.079	0.0150	0.20	0.35	0.9	0.15	0.30
PAG 5	0.020	0.0033	0.13	0.30	0.9	0.36	0.60

from experiment and model equations are shown in Figure 5-15.Table 4 compares the

TABLE 4. Comparing model prediction and experiment for process latitude

	PAG 1	*PAG 2*	*PAG 3*	*PAG 4*	*PAG 5*
DOF (um) from Experiment	0.22	0.39	0.15	0.22	0.35
DOF (um) from model	0.25	0.40	0.30	0.21	0.40
EL(%) from experiment	14.2	15.8	7.0	5.4	10.0
EL (%) from model	12.8	16.2	7.4	7.4	11.0

model prediction of the depth of focus (DOF) and exposure latitude (EL) to the experi-

mental data.Though the shape of experimental process window and simulation process

window differ due to imperfections in the exposure tools, it is seen that the model predic-

tion is consistent with experimental data. PAG 2 shows that largest process window

because of its high deprotection efficiency and low diffusion length. PAGs 3 and 4 show

the smallest process windows due to their high diffusion lengths. Figure 5-16a and

Figure 5-15b plots the DOF and EL respectively.

Figure 5-17a shows the line end shortening (LES) data and model fit for PAG 1 for

different doses. Similar fits were done on PAG data for all test resists to obtain the diffu-
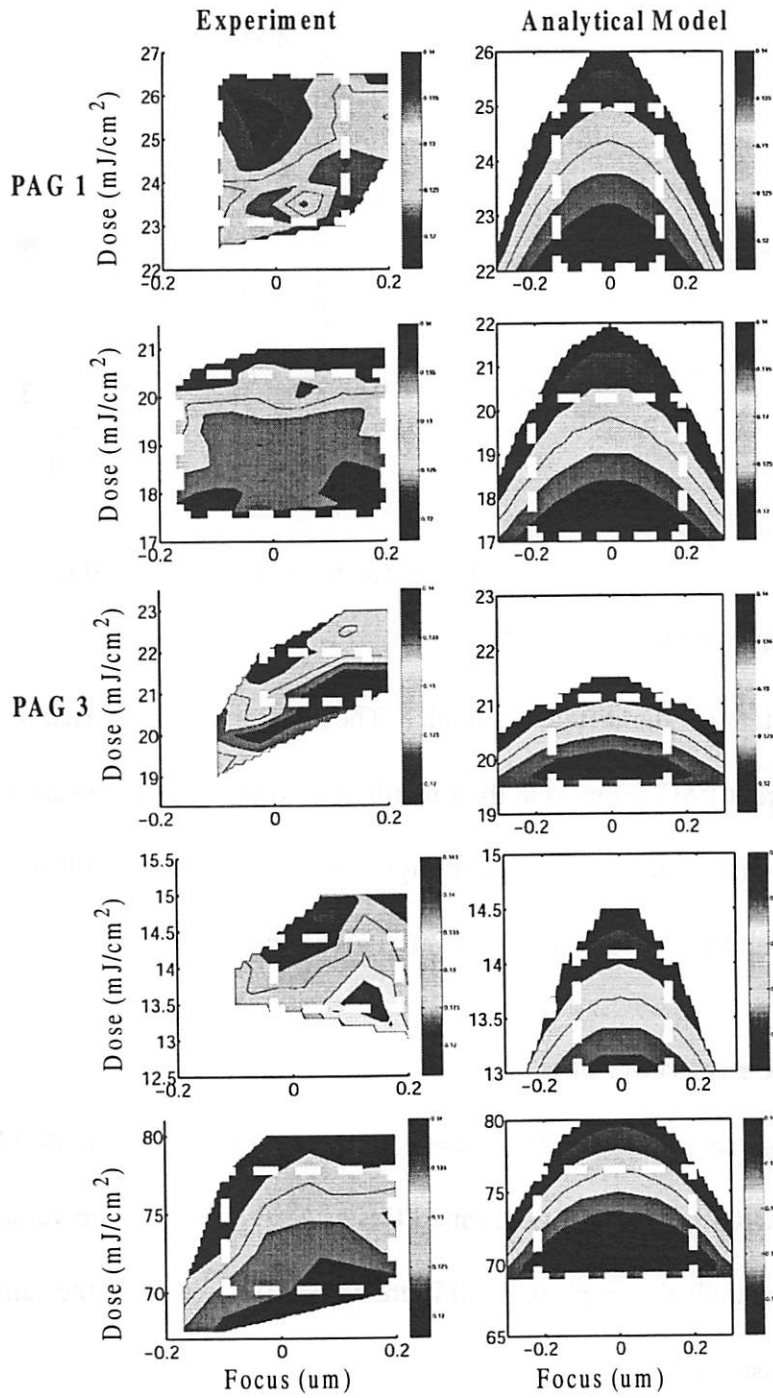
Figure 5-15. Process Windows for 130nm lines at +/- 10%

(a) Experiment. (b) simulation.

124
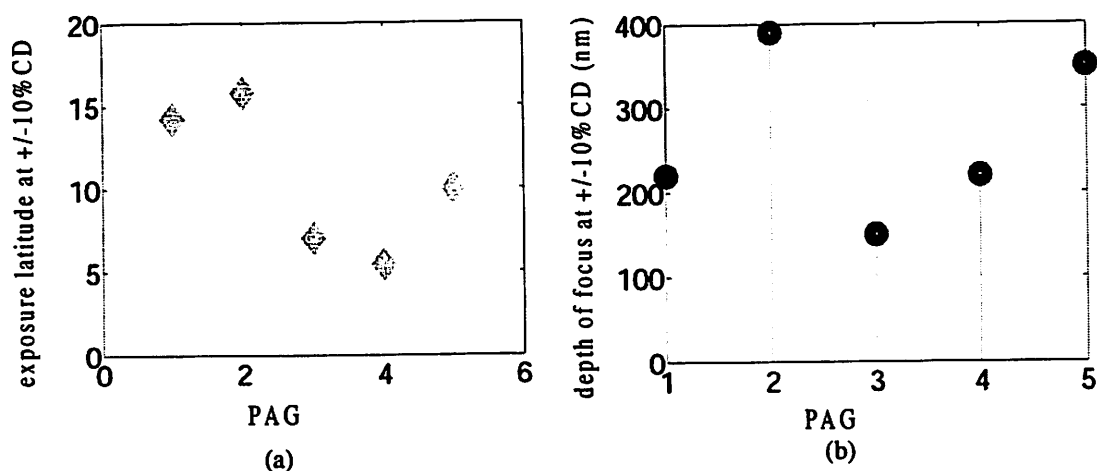
.Figure 5-16. Lithographic Properties of PAGs

(a) Exposure latitude. (b) Depth of Focus.

sion parameters for the different samples. These parameters are used to predict the LES

for the different PAG samples at their resolution doses. The results are plotted in Figure 5-

17b and the LES values are plotted in Figure 5-18c. It is seen that PAG 1 gives the lowest

LES, followed by PAG 2. PAGs 3, 4 and 5 give high LES values.

5.3.5.3. Line edge roughness

Line edge roughness (LER) analysis on the various PAG samples were performed

using the GORA (Graphically-Oriented Resist Analysis) software version 1.65. The

results of the analysis are plotted in Figure 5-18b. It is seen that the sample with PAG 2

gives the least LER.

5.3.6. Summary

In this section, the influence of structural changes in photoacid generators (PAGs) on

acid generation efficiency, deprotection efficiency and photoacid diffusion and their

125
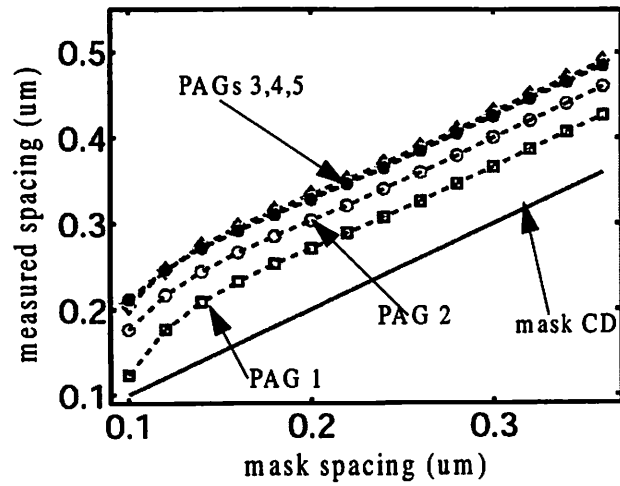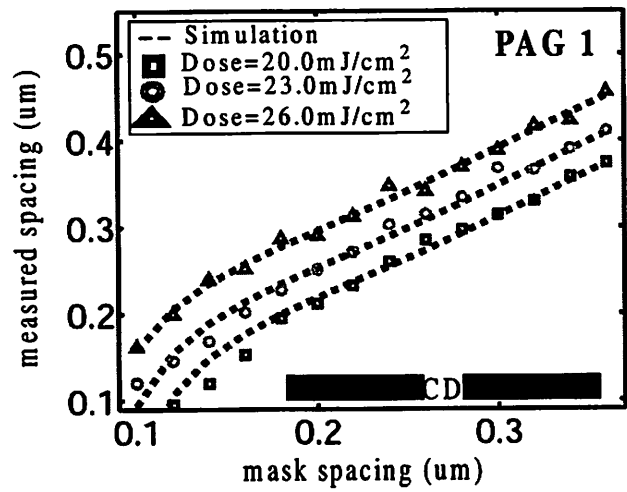
Figure 5-17. LES plots

(a) Extracting diffusion parameters from LES. (b) Comparing LES effects for different PAGs.

effects on line end shorting, process latitude and line edge roughness were documented.

The acid size and boiling point influence the deprotection efficiency and acid diffusion

and consequently the resist performance in fine feature lithography. An analytical model
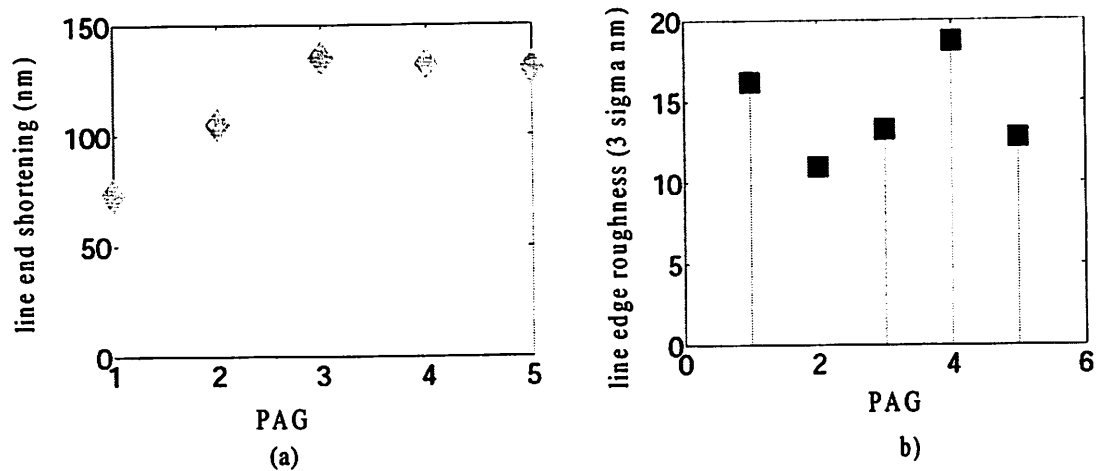
Figure 5-18. Lithographic Properties

(a) Line end shortening. (b) line edge roughness

for the post exposure bake process was used to quantify the deprotection efficiency and

the diffusion length and their effects on line end shortening and process latitude. It was

found that PAG 2 gave the best overall performance in terms of having a low resolution

dose (for throughput considerations), the highest deprotection efficiency, relatively low

diffusion length and line end shortening effect, the largest process window and the lowest

line edge roughness. These good performance of PAG 2 resist sample is attributed to the

small acid size and high boiling point temperature.

127

6 Conclusions

6.1. Summary

Modeling and simulation are useful for understanding factors responsible for various issues associated with the implementation of advanced lithography processes. Given the reduction in cost of computation and increase in cost of experimentation trend, process simulators will continue to provide cost effective means of understanding physical aspects of processing steps to allow for process optimization.

Rigorous numerical tools are described in this thesis to provide a general numerical framework for tackling complex model-equations encountered in advanced optical lithography resist process modeling. The numerical tools are code named STORM for Simulation Tools for Optical Resist Models.

STORM's simulation engine is based on advanced numerical methods such as the second order backward difference formula (BDF2) stiff ordinary differential equations (ODE) numerical integrator and the Krylov subspace Newton convergence accelerator. BDF2 is an implicit time advancement algorithm with variable timestep control. Krylov subspace convergence accelerator adds new capabilities to traditional numerical methods and can increase the speed of the simulator by orders of magnitude.

The finite element method (FEM) is used to discretize the simulation domain in space. The FEM algorithm is improved by employing method of partial variable substitution proposed by Lei Yuan [47]. This method allows reacting species that depend on time alone to be eliminated from nodal update calculations. This elimination reduces the size of the global system, thus increasing the speed of the simulation.

The variable elimination finite element method (FEM) is compared to numerical algorithms based on higher order finite difference methods (FDM) proposed by Mosong Cheng[51]. Although both methods give comparable simulation performance, the FEM method has the capability to simulate volume shrinkage effects as observed in chemically amplified resist. However it required more memory resources than the FDM. It is believed that a hybrid algorithm combining the high order FDM and variable elimination FEM will offer a very efficient simulation engine for optimum memory, speed and accuracy.

The efficiency of STORM at simulating highly nonlinear model-equations allows for mechanistic based moving boundary models to be simulated efficiently. The numerical tools were used to demonstrate a moving boundary silylation simulator which includes polymer relaxation, reaction dependent silylating agent diffusivity, and stress dependent retardation of the reaction rate. Simulation results illustrate the interplay of the various physical parameters in determining final silylation depth and sidewall angle as a function of exposure and silylation conditions and the film's material properties. This simulator is an important new capability which can serve as a guide for future characterization of silylation processes by studying the time evolution of the silylated profile as a function of

both optical and processing conditions, and for developing an intuitive understanding of the fundamental mechanisms which govern silylated resist image formation.

Monte Carlo methods for simulating oxygen reactive ion etching for surface imaging resist processes are also described in this thesis. The performance of STORM is degraded during dry development simulation because of the nondeterministic nature of the Monte Carlo method for ion bombardment. Monte Carlo simulations pose problems for multistep methods since timestep determination depends on deterministic time evolutions of reacting species. The random nature of the ions during the etching process causes the time evolution of the reacting species to be random.

A survey of models and characterization techniques for chemically amplified resist (CAR) processes including contributions to CAR exposure and post exposure bake (PEB) modeling and characterization are documented. A model based on a moving boundary acid transport concept that incorporates transient free volume generation and densification is described. It is able to link the relief image formation to the mechanical and chemical properties of the resist polymer and is capable of simulating the resist shrinkage upon baking. The model reduces to simple Fickean and case II type diffusion models under some simplifying assumptions. The simulations show acid trapping due to densification of the polymer after free volume elimination. This acid trapping process must be considered in addition to losses due to volatility and other loss mechanisms that have yet to be understood.

It is observed that modeling the diffusivity as an exponential function of protected group concentration emulates acid transport retardation due to polymer densification. This allows the model to be simplified by assuming free volume influence on diffusion

130

can be captured by protected group concentration. This reduces the complexity of modeling and characterization by eliminating the free volume variable and associated parameters.

The thesis presents a model for characterizing 193nm chemically amplified resists using the STORM program. Simplifying assumptions are made to derive analytical expressions for the post exposure bake process. Methodology for extracting the exposure, reaction and diffusion parameters for 248nm resists are used to obtain the modeling parameters. STORM optimization engine is utilized in optimizing the extracted parameters for model calibration. Application results to Bell Labs/Arch Chemical 193nm dense resists show that the resist behavior is well described by both the analytical solution and the protected group dependant exponential diffusion model. Line end shortening of different mask features are accurately predicted by the models.

Another application example presented in this thesis is the modeling of the influence of structural changes in photoacid generators (PAGs). The study focuses on acid generation efficiency, deprotection efficiency and photoacid diffusion and their effects on line end shorting, process latitude and line edge roughness. The acid size and boiling point influence the deprotection efficiency and acid diffusion and consequently the resist performance in fine feature lithography. An analytical model for the postexposure bake process was used to quantify the deprotection efficiency and the diffusion length and their effects on line end shortening and process latitude. It was found that PAG with small acid size and high boiling point gave the best overall performance in terms of having a low resolution dose (for throughput considerations), the highest deprotection efficiency,

131

relatively low diffusion length and line end shortening effect, the largest process window and the lowest line edge roughness.

6.2. Improvements and extensions of STORM

Rigorous simulation in lithography requires simulation capabilities of 3-dimensional effects. Optical lithography issues such as reflective notching, line end shortening, resist footing and T-topping require 3-dimensional simulators to capture their effects. Until the recent advances in numerical algorithms documented in this thesis, rigorous 3-dimensional simulation of PEB effects using mechanistic based physical models presented a big challenge as these simulators took days due to the large increase in the number of nodes representing the 3-dimensional domain. With the algorithms presented in this dissertation, 3-dimensional simulations are now practical. The FEM algorithm can be further improved by incorporating the higher order basis functions employed in the modified FDM algorithm. This hybrid algorithm combining the high order FDM and variable elimination FEM will offer a very efficient simulation engine for optimum memory, speed and accuracy.

There is an interest in rigorous 3-dimensional simulators that can be calibrated to the lithography tools. Such a simulator can be used for physical verification of optical proximity corrected (OPC) layouts. The cost of making a reticle and exposing wafers to verify OPC correction is becoming prohibitively expensive. As such, a reliable and efficient 3-dimensional simulator well tuned to the lithography process in the fab will be an invaluable tool to the lithographer.

Bibliography

[1]   J. Lorenz, J. Pelka, H. Ryssel, A. Sachs, A. Seidl, and M. Svoboda, "COMPOSITE, A Complete Modeling Program of Silicon Technology," IEEE Trans. Computer-Aided Design of Integrated Circuits and Systems. vol. CAD-4, no. 4, pp. 421-430, April 1985.

[2]   W. G. Oldham, S. N. Nandgaonkar, A. R. Neureuther, and M. M. O'Toole, "A General Simulator for VLSI Lithography and Etching Process: Part I - Applications to Projection Lithography," IEEE Trans. Electron Devices, vol. ED-26, no. 4, pp. 717-722 (1979).

[3]   Technology Modeling Associates, DEPECT-2, Technology Modeling Associates, 1990.

[4]   C. A. Mack, "PROLITH: A Comprehensive Optical Lithography Model," Proc. of SPIE, vol. 538, pp. 207-220 (1985).

[5]   W. Henke, D. Mewes, M. Weiss, G. Czech, and R. Schiessl-Hoyler, "Simulation of Defects in 3-Dimensional Resist Profiles in Optical Lithography," Microelectronic Engineering, vol. 13, pp. 497-501 (1991).

[6]   M. E. Law and R. W. Dutton, "Verification of Analytic Point Defect Models Using SUPREM-IV," IEEE Trans. CAD, vol. 7, pp. 181-190 (1988).

[7]   S. Pantas, "Finite Element Methods for Process Simulation Application to Silicon Oxidation", Ph.D. Thesis, Memorandum No. UCB/ERL M88/26, University of California, Berkeley, May 1988.

[8]   M. Zuniga, "Fundamental Mechanisms in Advanced Resist System in Optical Lithography", Ph.D. Thesis, University of California, Berkeley, May 1999.

[9]   P.R. Gray, R.G. Meyer, "Analysis and Design of Analog Integrated Circuits". Wiley, New York, 1993.

[10]   R.S. Muller, T.I. Kamins, "Device Electronics for Integrated Circuits". Wiley, New York, 1986.

[11]   M. A. Zuniga, G. Wallraff, E. Tomacruz, A.R. Neureuther, J. Vac Sci. Technol B. 1, 2862 (1993).

[12]   L. Pain, C. Le Cornec, C. Rosilio, P Piniez, Proc. SPIE, Vol. 2724 100-109 (1996).

[13]   F. H. Dill, "Optical Lithography", IEEE Trans. Electron Devices, ED-22, No. 7 (1975) pp.440-444.

[14]   F. H. Dill, W.P. Hornberger, P.S. Hauge, and J.M. Shaw, :Characterization of Positive Photoresist", IEEE Trans. Electron Devices, ED-22, No. 7 (July, 1975) pp.445-452.

[15]   F.H. Dill, A.R.Neureuther, J.A. Tuttle, and E.J. Walker, "Modeling Projection Printing of Positive Photoresists", IEEE Trans. Electron Devices, ED-22, No. 7 (1975) pp.456-464.

[16]   C. R. Szmanda, R. Kavanagh, J. Bohland, J. Cameron, P. Trefonal, R. Blacksmith, Proc. SPIE, Vol 3678, 857-866, (1999).

[17]   J. Thackeray, M. Denison, T. Fedynyshyn, D. Kang, R. Sinta, Proc. Acs Symp. Ser., 614, 110, (1995).

[18]   J. Cameron, D. Kang, M. King, J.M. Mori, S. Virrdee, T. Zydowsky, R. Sinta, Proc. SPE, Photopolymers, Oct. 6-8, (1997), Great Gorge, NJ, p. 20.

[19]   A. R. Eckert, W.M. Moreau, "Fluorescence detection of photoacid in chemically amplified resists", Proc. SPIE-Int. Soc. Opt. Eng., (1997), 3049, 879-887.

[20]   U. Okoroanyanwu, J.D. Byers, T. Cao, S. E. Webber, C.G.Willson, "Monitoring photoacid generation in chemically amplified resist systems,: Proc. SPIE-Int. Soc. Opt. Eng., (1998), 3333, 747-757.

[21]   G. Pohlars, J.C. Scaiano, R. Sinta, "A novel Photometric Method for the Determination of Photoacid Generation Efficiencies Using Benzothiazole and Xanthene Dyes as Acid Sensors", Chem. Mater. (1997) 9(12) 3222-3230,

[22]   J. Byers, J. Petersen, J. Sturtevant, "Calibration fo ChemicallyAmplified Resist Models", Proc. SPIE-Int. Soc. Opt. Eng., (1996), 2724, 156-162.

[23]   C.G. Willson, H. Ito, J. Frechet, T. Tessier, and F. Houlihan, "Approaches to the Design of Radiation-Sensitive Polymeric Imaging Systems with Improves sensitivity and Resolution," J. Electrochem Soc., vol. 133, no. 1, pp181-187, 1986.

[24]   T.H. Fedynyshyn, J.W. Thackeray, J.H. Georger, M.D. Denison, J. Vac. Sci. Tech. B 3888 (1994).

[25]   E. Reichmanis, F.M. Houlihan, O. Nalamasu, T. X. Neenan, Chem. Mater. 3 349 (1991).

[26]   D. Seligson, S. Das, H. Gaw, P. Pianetta, J. Vac. Sci. Technol B 6 2303, 1998.

[27]   H. Fukuda, S. Okazaki, "Kinetic Model and Simulation for Chemical Amplification Resists," J. Electrochem. Soc., vol. 137, no. 2, pp. 675-679, 1990.

[28]   A. Krasnoperova, M. Khan, S. Rhyner, J. Taylor, Y. Zchu, F. Cerrina, J. Vac. Sci. Technol. B 12(6) 3900 (1994)

[29]   T. Watanabe, Y. Yamashita, J. Vac. Sci. Technol. B 12(6) 3879 (1994)

[30]   R. Ferguson, J.M. Hutchinson, C.A. Spence, A.R. Neureuther, J. Vac. Sci. Technol. B 8(6) 1423 (1990).

[31]   R.A. Ferguson, "Modeling and Simulation of Reaction Kinetics in Advanced Resist Processes for Optical Lithography", Ph.D. Thesis, Memorandum No. UCB/ ERL M91/78, University of California, Berkeley, September 1991.

[32]   G.M. Wallraff, J.M. Hutchinson, W. Hinsberg, F. Houle, P. Seidel, R. Johnson, J. Vac. Sci. Technol. B 12(6) 3857 (1994)

[33]   R. R. McKean, U. Schaedeli, S.A. MacDonald, ACS Symp. ser 412, 27 (1989).

[34]   J. Nakamura, B. Hiroshi, A. Tanaka, Jpn. J. Appl. Phys. Vol 33, Pt1. No. 11 1994.

[35]   T. Yoshimura, Y. Nakayama, and S. Okazaki, J. Vac. Sci. Technol. B 10(6), 2615 (1992).

[36]   T.H. Fedynyshyn, C.R. Szmanda, R.F. Blacksmith, W.H. Houck, J.C. Root, J. Vac. Sci. Technol. B. 11(6) 2798 (1993).

[37]   W.D. Hinsberg, S.A. MacDonald, N.J. Cleak, C. Snyder, Proc. SPIE 2194 (1994).

[38]   P. Trefonas, M.T. Allen, Proc. SPIE 1872, 74, 1994.

[39]   J. S. Petersen, C.A. Mack, J.W. Thackeray, R. Sinta, T.H. Fedynyshyn, J.M. Morei, J.D. Byers and D.A. Miller, SPIE, Vol 2438, pp153-166, 1995.

[40]   L. Schlegel, T. Ueno, N. Hayashi, T. Iwayanagi, J. Vac. Sci. Technol. B 9 278 (1991).

[41]   S. Schlegel. T. Ueno, N. Hayashi, T. Iwayanagi, Micor. Eng. 11 (1991).

[42]   T. Yoshimura, H. Shiraishi, J. Yamamoto. S. Ozakaki, Appl. Phys. Lett. 63, 764, (1993).

[43]   J. Crank, "The mathematics of Diffusion", New York, NY: Oxford University Press, 1975.

[44]   S. Postnikov, M. Stewart, H. V. Tran, M. Nierode, D. Mederios, T. Cao, J. Byers, W. Hinsberg, S. Webber, C. G. Willson, to be published in J. Vac. Sci. Technol. Nov/Dec 1999.

[45]   R. W. Korsmeyer, S.R. Lustig, N. A. Peppas, J. Polym. Sci. Phys. Ed. Vol 24, 395-408, Feb. 1986.

[46]   H. Fujita, A. Kishimoto, and K. Matsumoto, Transactions of the Faraday Society, Vol. 56, 424-437 (1960)

[47]   Y. Lei, E. Croffie, M. Cheng, A. Neureuther, Submitted to Proc. SPIE (2001).

[48]   G.M. Schmid, V.K. Singh, L.W. Flanagin, M.D. Stewart, S.D.Burns and C.G. Willson. Proc. SPIE, Vol. 3999 pp.675-685. (2000)

[49]   S. Pantas, "Finite Element Methods for Process Simulation Application to Silicon Oxidation", Ph.D. Thesis, Memorandum No. UCB/ERL M88/26, University of California, Berkeley, May 1988

[50]   F. Dill, A Neureuther, J. Tuttle, E. Walker, IEEE Trans. Electron Devices, ED-22, No 7 pp.456-464, Sept. 1975.

[51]   E. Croffie, M. Cheng, A. Neureuther, F. M. Houlihan, R. A. Cirelli, J. Sweeney, G. Dabbagh, O. Nalamasu, I. Rushkin, O. Dimov, A. H. Gabor. Proc. SPIE, Vol. 3999 (2000)

[52]   M. Cheng, E. Croffie, A. Neureuther, Proc. SPIE, Vol. 3999 (2000).

[53]   F. M. Houlihan, T. Wallow, A. Timko, E. Neria, R. Hutton, R. Cirelli, J.M. Kometani, O. Nalamasu, E. Reichmanis, J. of Photopolymer Sci. & Tech. 10 (3), 1997

[54]   S. V. Postnikov, M. D. Stewart, H. V. Tran, M. A. Nierode, D. R. Medeiros, T. Cao, J. Byers, S. E. Webber, C. G. Willson, J. Vac. Sci. Tech. B 17(6), Nov/Dec 1999

[55]   Ohfuji, T. Ogawa, T. Kuhara, K.; Sasago, M. Journal of Vacuum Science & Technology B, Nov.-Dec. 1996, vol.14, (no.6):4203-6.

[56] Horn, M.W.; Maxwell, B.E.; Goodman, R.B.; Kunz, R.R. Journal of Vacuum Science & Technology B, Nov.-Dec. 1996, vol.14, (no.6):4207-11.

[57] La Tulipe, D.C. Simons, J.P. Seeger, D.E. Proc. of the SPIE vol 2195 (1994) 372-78

[58] Weib, M. Goethals, M. Microelectronic Engineering 30 (1996) 313-16.

[59] Simakov, N.N. Mikroelektronika vol. 26 (30) Jan 1997.

[60] McDonagh, D. Arshak, K. Arshak, A. Optical Engineering, (1996) 277-83.

[61] McDonagh, D. Arshak, K. Arshak, A. Proc. of the SPIE vol.2195 (1994) 497-505.

[62] Jaghold, U. Bauch, L. Proc. of the SPIE vol. 2438 (1995) 884-8.

[63] Pierrat, C. Journal of Vacuum Science & Technology B, 10(6) (1992) 2581-88.

[64] Hartney, M.A. Journal of Vacuum Science & Technology B, 11(3) 681-7 May/Jun 1993.

[65] R. Visser, J. Schellekens, M. Reuhman-Huisken, L Van Ijzendoorn, Proc. SPIE, Vol. 771 111-117 (1987)

[66] Pierrat, C. Journal of Vacuum Science & Technology B, 10(6) (1992) 2581-88

[67] M. Zuniga, E. Croffie, and A. Neureuther, Proc. SPIE, Vol. 3333 611-624. (1998)

[68] Wong, A. PhD thesis, The University of California at Berkeley, 1994.

[69] B. Roland, R. LomBerts, C. Jakus, and F. Coopmans, Proc. SPIE, Vol. 771 69-76 (1987).

[70] Hartney, M.A. Journal of Vacuum Science & Technology B, 11(3) 681-7 May/Jun 1993.

[71] C.A. Spence, S.A. MacDonald, H. Schlosser, Proc. SPIE, Vol. 1262, 344-357 (1990)

[72]   H. Fujita, A. Kishimoto, and K. Matsumoto, Transactions of the Faraday Society, Vol. 56, 424-437 (1960)

[73]   W. G. Oldham, S. N. Nandgaonkar, A. R. Neureuther, and M. O'Toole, *IEEE Trans. Electron Devices*, ED-26, No 4 pp.717-722, April 1979.

[74]   Han-Ming Wu; Graves, D.B.; Kilgore, M., Plasma Sources Sci. Technol. , vol.6, (no.2), May 1997. p.231-9.

[75]   see http://speedie.stanford.edu

[76]   J. Pelka, Microelectronic Engineering, 14, pp.269-281 (1991).

[77]   see http://math.berkeley.edu/~sethian/level_set.htm

[78]   see http://www.sigma-c.de

[79]   Kruger, C.H.; Owano, T.G.; Laux, C.O. IEEE Trans. Plasma Sci. , vol.25, (no.5), IEEE, Oct. 1997. p.1042-51.

[80]   Sethian, J.A., *Numerical Methods for Propagating Fronts*, in Variational Methods for Free Surface Interfaces, edited by P. Concus and R. Finn, Springer-Verlag, New York, 1987

[81]   M. A. Lieberman, A. J. Lichtenberg, Principles of Plasma Discharge and Materials Processing, John Wiley & Sons, Inc, New York, (1994).

[82]   M. Cheng, E. Croffie, and A. Neureuther, Proc. SPIE, Vol. 3678, (1999)

[83]   J. Reddy, An introduction to the finite element method, McGraw Hill, New York, (1993).

[84]   K. Miller, Lecture Notes for Numerical Solutions of Ordinary Differential Equations (Math 228A), University of California, Berkeley, Fall 1997.

[85]   N. Carlson and K. Miller, Design and application of a gradient-weighted Moving Finite Elements, Part 1, Report No. 236, Center Appl Math., Purdue U., May 1994 43-46

[86]   C. W. Gear, Numerical Initial Value Problems in Ordinary Differential Equations.Prentice Hall, Inc, New Jersey pp. 215-220, (1971)

[87]   see http://www.cs.berkeley.edu/~xiaoye/superlu.html

[88]   E.Z. Xaba, "Robust Iterative Solvers for Linear and Nonlinear Finite Element Equations", Ph.D. Thesis, Department of Mathematics, University of California, Berkeley, September 1997.

[89]   R. N. Haward and G. Thackray, Proc. Roy. Soc. A., 302: 453-472, 1968

[90]   M. Zuniga, E. Croffie, and A. Neureuther, Proc. SPIE, Vol. 3333 611-624. (1998)

[91]   E. H. Croffie, *Moving Boundary Models and Methods for Deep Submicron Resist Process Simulations*, Master's Report, University of California Memo No. UCB/ERL M99/26, May 1999.

[92]   R. A. Ferguson, *Modeling and Simulation of Reaction Kinetics in Advanced Resist Processes for Optical Lithography*, Ph.D. thesis, University of California Memo No. UCB/ERL M91/78, May 1991

[93]   Zuniga, A. R. Neureuther, J. Vac. Sci. Tech. B, Nov/Dec 1995.

[94]   C. Mack, *Inside PROLITH: A Comprehensive Guide to Optical Lithography Simulation*, Finle Technologies, Inc. (1997).

[95]   C. R. Szmanda, R. Kavanagh, J. Bohland, J. Cameron, P. Trefonal, R. Blacksmith, Proc. SPIE, Vol 3678, 857-866, (1999)

[96]   M. Cheng, E. Croffie, A. Neureuther, Proc. SPIE, Vol 3678, 1999

[97]   F. M. Houlihan, T. Wallow, A. Timko, E. Neria, R. Hutton, R. Cirelli, J.M. Kometani, O. Nalamasu, E. Reichmanis, J. of Photopolymer Sci. & Tech. 10 (3), 1997.

[98]   F. Dill, A Neureuther, J. Tuttle, E. Walker, IEEE Trans. Electron Devices, ED-22, No 7 pp.456-464, Sept. 1975.

[99]   G. N. Vanderplaats, *Numerical Optimization Techniques for Engineering Design*, McGraw Hill, New York, 1984.

[100] F. M. Houlihan, J. M. Kometani, A. G. Timko, R. S. Hutton, R. A. Cirelli, E. Reichmanis. O. Nalamasu, A. H. Gabor, A. N. Medina, J. J Biafore. S. G. Slater, J. of Photopolymer Sci. & Tech. 11, (1998).

[101] R. D. Allen, J. Opitz, C. E. Larson, R. A. DiPietro, G. Breyta and D. C. Hofer, Proc. SPIE, Vol. 3049 44-54 (1997).

[102] R. D. Allen, J. Opitz, C. E. Larson, R. A. DiPietro, G. Breyta and D. C. Hofer, Proc. SPIE, H. W. Krautter, F. M. Houlihan, R. S. Hutton, I. I. Rushkin, and R. L. Opila, Proc. SPIE, Vol. 3999 (2000).Vol. 3049 44-54 (1997).

[103] J. Byers, Private Communications, Nov. 1999.

[104] A. H. Gabor, L. C. Pruette, C. K. Ober, Chemistry of Materials, Vol. 8, (9) 2282-2290 (1996).

[105] J. C. Simo and T.J.R. Hughes, *Computational Inelasticity*, Springler, New York, 1998.